Modeling coastal circulation in Norway using a high-resolution 4D-Var ocean assimilation system

Ann Kristin Sperrevik

Dissertation for the degree of Philosophiae Doctor (PhD)

Geophysical Institute
University of Bergen

March 2017

Abstract

The circulation along the Norwegian coast is characterized by many transient small-scale features such as eddies and meanders that are challenging to reproduce by means of numerical modeling. In this thesis I investigate the use of advanced data assimilation (DA) techniques in high-resolution coastal models to improve the circulation estimates.

One particularly interesting observational platform for the coastal ocean is high-frequency (HF) radars, which measure surface currents in the coastal zone up to 200 km offshore. The suitability of such observations for use in high-resolution coastal DA systems is assessed by quantifying which components of the near-surface current field are observed by the HF radars. Our results show that there are no contributions from wave drift in the measurements, thus they are suitable for use in coastal DA. Assimilation of HF radar currents in a high-resolution model shows clear improvement in the circulation estimates. Further improvement is obtained when CTD profiles of temperature and salinity are included in the assimilated data set.

A reanalysis of a period, during which in-situ observations were abundant in the study area, is used to assess how an observational network dense enough to constrain the water mass distribution affects the upper ocean circulation estimates. Our investigations of the results show a weakening of the topographically steered currents and, as the stratification increases the effective resolution of the model, more small-scale circulation features are developed. Such changes may have a significant effect on upper ocean transport. Finally, the potential of using high-resolution coastal reanalyses to study specific physical processes is demonstrated for the case of the mechanisms causing variability in the Norwegian Coastal Current.

List of papers

1. Röhrs, J., A. K. Sperrevik, K. H. Christensen, G. Broström, and Ø. Breivik: *Comparison of HF radar measurements with Eulerian and Lagrangian surface currents*, Ocean Dynamics **65**, 679-690, 2015.
2. Sperrevik, A. K., K. H. Christensen, and J. Röhrs: *Constraining energetic slope currents through assimilation of high-frequency radar observations*, Ocean Science **11**, 237-249, 2015.
3. Sperrevik, A. K., J. Röhrs, and K. H. Christensen: *Impact of data assimilation on Eulerian versus Lagrangian estimates of upper ocean circulation*, under revision for Journal of Geophysical Research - Oceans
4. Christensen, K. H. , A. K. Sperrevik, and G. Brostöm: *On the variability in the onset of the Norwegian Coastal Current*, Manuscript

Scientific environment

This PhD study has been carried out at the Norwegian Meteorological Institute, Division of Ocean and Ice, Oslo, Norway. A total of 4 weeks was spent at the University of California, Santa Cruz. The work has largely been funded by MET Norway, with contibutions from the Norwegian Clean Seas Foundation (NOFO) and ENI Norge A/S, and the Norwegian Research Council through grants 244262 (RETROSPECT) and 237906 (CIRFA). Additional travel grants have been provided by ResClim.

UNIVERSITAS BERGENSIS

Norwegian
Meteorological
Institute

Acknowledgements

First and foremost, I would like express my gratitude to my supervisor Kai H. Christensen. Your encouragement and support has been essential for the completion of this thesis, and I have truly learned a lot from you. I would also like to thank my co-supervisors Johnny A. Johannessen and Nils Gustafsson for sharing their insights and asking critical questions. A big thank you goes to Øyvind Breivik for his excellent guidance during the first year of the project, and to Øyvind Sætra who initiated this project.

I feel privileged to have been given the opportunity to conduct the research for my PhD project in the *Ocean and Ice* division at MET Norway and would like to thank all my colleagues for valuable discussions, advises and help. Johannes Röhrs deserves additional attention, as his contributions have lifted the quality of my research. Discussions with Frode Vikebø and Svein Sundby at the IMR have expanded my horizon, thank you! Thanks also to Andy Moore for welcoming me at University of California, Santa Cruz and for taking an interest in my research.

To my family and friends: thanks for your continued support and encouragement. Finally, a huge thank you to my ever-patient husband Tormod, who has provided both technical as well as emotional support.

Contents

Chapter 1

Introduction and Objectives

1.1 Introduction

Human activities at sea such as shipping, oil exploitation, fisheries, and recreation largely occur in the coastal ocean and shelf seas. These regions are also important for marine life as they serve as spawning and feeding grounds for several fish stocks, such as the Northeast Arctic cod, and are hot spots for primary production in the ocean. Circulation estimates from operational forecasts are key components of emergency response services such as search-and-rescue and oil spill mitigation (Breivik and Allen, 2008; Jordi et al., 2006; Röhrs and Christensen, 2015), while data archives of the ocean state during a historic period can be used e.g. for studies of physical processes, connectivity studies (Ådlandsvik and Sundby, 1994; Mitarai et al., 2009), or to assess the mechanisms causing inter-annual variability in recruitment (Svendsen et al., 2007). For many such purposes, the currents in the uppermost part of the ocean are most relevant.

Upper ocean currents are largely wind-driven, but particles drifting in the sea are also affected by transient current features such as tides and eddies as well as large-scale geostrophic currents. Eddies are the oceanic equivalent to high and low pressure systems in the atmosphere, but their horizontal scales are much smaller due to the shorter internal deformation radius in the ocean. In order to provide realistic estimates of ocean currents this scale needs to be resolved by the model. High resolution also allows for a more accurate description of the bathymetry and a more detailed coastline, an important point as many accidents happen close to shore (Broström et al., 2011; Gundlach and Hayes, 1978) and the environmental consequences of a spill often will be more pronounced in the coastal zone (Ihaksi et al., 2011).

A realistic representation of water masses is crucial for the skill of an ocean model, as this affects the baroclinic response to surface forcing, as well as the generation of eddies through baroclinic instabilities occurring at fronts between water masses of different densities. Furthermore, the depth at which a buoyant particle will flow is determined by the density of the surrounding water. As both the strength and direction of wind-driven currents are depth dependent, this will affect the particle's faith (Hannah et al., 1997; Myksvoll et al., 2014; Vikebø et al., 2007).

In addition to the small spatial scales, the ocean has a long memory. This means that features such as eddies will persist over several days to weeks, and water properties, particularly below the mixed layer, for even longer periods of time. Due to these long temporal scales errors in ocean models can largely be viewed as caused by deficiencies in the initial conditions. For small regional applications, however, the boundary values become more important, particularly for the upper ocean where the currents are generally stronger. Similar to the case of limited area models in numerical weather prediction, errors due to unresolved physical processes in the coarser model from which the boundary conditions are provided, propagate into the model domain (Warner et al., 1997). Thus, coastal ocean modeling is both an initial and a boundary value problem, and in order to produce realistic estimates of the coastal circulation, errors in both these sources need to be constrained.

Data assimilation (DA) can improve a model estimate of the ocean state by adjusting the model fields according to observations. DA methods take both uncertainties associated with the model fields as well as uncertainties associated with the observations into account, thus DA combines an inaccurate model with inaccurate observations in order to obtain the best possible description, an analysis, of the true state of the ocean. However, the resolution of the model poses a limit to the precision of the analysis: Even if there are sufficient observations to describe an eddy, the model is incapable of reproducing it if the size of the eddy is too small to be resolved numerically. This is referred to as the error of representativeness, and is usually the largest source of uncertainty associated with an observation.

DA has been a large contributor to the improved quality of weather forecasts over the past few decades, and is commonly used in operational oceanography as well, especially for global and basin-scale applications (Blockley et al., 2014; Oke et al., 2015a; Sakov et al., 2012). In contrast to the observational network for the atmosphere, the oceanic observational network does not resolve the spatial variability, particularly below the surface. This is a major challenge for high-resolution assimilation systems as they require a denser observational network to constrain the circulation (Oke et al., 2015b). One particular challenge is the inherent lack of current observations: with the notable exception of high-frequency (HF) radars which can observe surface currents in the coastal zone, there are hardly any observations of this important variable.

1.2 Objectives

The main objective of this thesis is to study the requirements that must be met by the ocean model and the observing system in order to obtain improvement in the representation of upper ocean circulation in high-resolution coastal ocean models. A second aim is to determine whether assimilation of existing and planned observational networks can improve circulation estimates of the coastal ocean. In a long-term perspective we hope to develop methodology for improving operational ocean forecasts and for giving recommendations on the design of future observational networks supporting this aim. Specifically, the following points are targeted:

- Assessing the potential impact on forecast skill when assimilating HF radar observations of surface currents.
- Understanding how assimilation of hydrography observations impact near-surface circulation estimates.
- Investigate if information from different observation types complement each other or render some observations redundant.

- Use a reanalysis of the ocean state in coastal region to investigate the mechanisms causing variability in the circulation, and to what degree the different observation sources contribute to the improved circulation estimates.

To answer these questions, coastal model applications using four-dimensional variational (4D-Var) assimilation techniques have been applied, assimilating various types of ocean observations. The main focus of the investigations of the results is the impact on the upper ocean circulation, an important component in ocean forecasting.

Chapter 2

Scientific background

2.1 The Norwegian Shelf Seas

The Norwegian coastline is long and complex, scattered with numerous islands and skerries. Fjords add to the complexity: some stretch more than 100 km inland, and many fjords are deeper than the adjacent seas. Norway borders four marginal seas. Starting from the north these are the shallow Barents Sea; the Norwegian Sea, which has a shallow shelf along the Norwegian coast with a steep shelf break into the deep basin; the North Sea, another shallow shelf sea; and Skagerrak in the south. Skagerrak is shallow apart from the Norwegian Trench, an underwater canyon stretching from the shelf break outside western Norway and along the coast into Skagerrak where it reaches its maximum depth of 700 m (Fig. 2.1).

Skagerrak serves as the only natural connection of the Baltic Sea with adjacent seas, and the circulation is heavily influenced by the freshwater outflow from the Baltic. This outflow gives rise to the Norwegian Coastal Current (NCC), which carries fresh coastal water northwards along the coast. Although additional freshwater is supplied from rivers and fjords along the coast, the water of the NCC becomes more saline as it moves northwards due to entrainment of waters of Atlantic origin. Atlantic water, defined as water with salinity above 35, enters the Norwegian Sea through three passages: The Denmark Strait, the opening between Iceland and the Faroe Islands, and through the Faeroe-Shetland channel. The water associated with the latter two inflows forms The Norwegian Atlantic Current (NAC), and flows northward along the eastern rim of the Norwegian Sea. Minor branches of the NAC break off from the main path and flows into the North Sea and along the Norwegian Trench into the Skagerrak. On its way northward, the NAC flows in near-parallel with the NCC before the two currents partly converge outside Vesterålen, where the continental shelf is at its narrowest. This region is highly dynamic with current speeds often exceeding 1 m/s and high eddy kinetic energy levels (Isachsen et al., 2012). As the currents continue northwards, the main branch of the NAC breaks off from the coast and follows the shelf break towards Spitsbergen and into the Arctic Ocean, while the NCC continues along the coast into the Barents Sea.

The NCC is often described as being wedge-shaped, and this shape has a strong seasonal dependence arising from both seasonal varying runoff levels and variations in the solar insolation. Increased freshwater supply and solar warming during the summer months result in a broad and shallow current wedge, while surface cooling and low

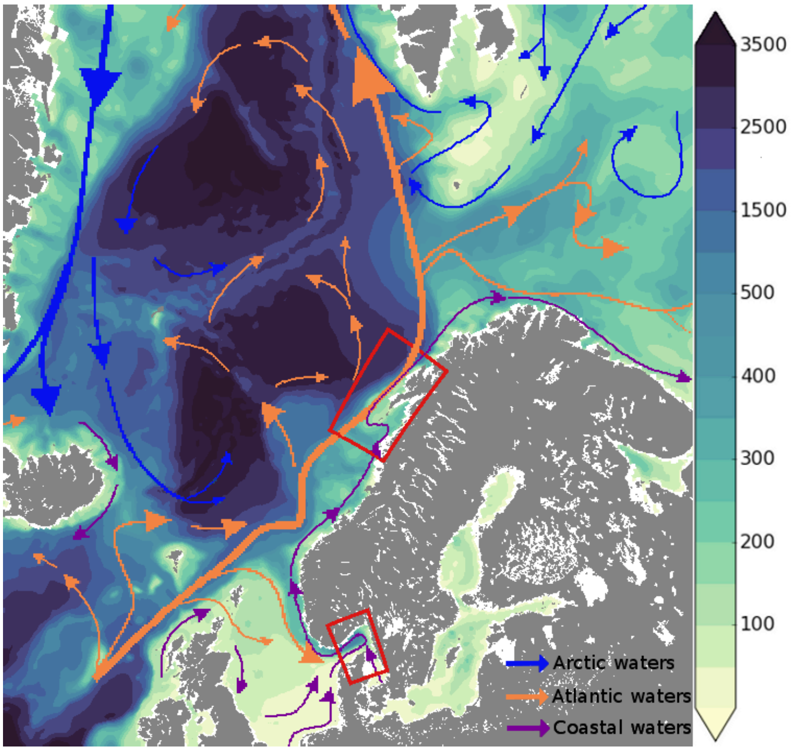

Figure 2.1: Map of Norwegian waters. The bathymetry is indicated in shading, while the arrows display the main currents. The two model domains used in the thesis papers are shown in red. The currents are reproduced from graphic by IMR (`http://www.imr.no/nyhetsarkiv/2006/november/ingen_stopp_i_golfstrommen/nb-no`).

runoff levels during the winter season makes the wedge deep and narrow (Saetre, 2007).

The tidal signal along the Norwegian Coast is dominated by a tidal wave entering the Norwegian waters from the North Atlantic and propagating northwards along the coast as a Kelvin wave (Saetre, 2007). The tidal amplitude varies significantly, with generally small amplitudes found in Skagerrak, amplitudes close to zero outside Egersund in southwestern Norway where an amphidromic point is found, and amplitudes close to 4 m in Northern Norway. The dominating tidal constituents are the diurnal lunar and solar components, M2 and S2.

Providing realistic estimates of the highly dynamic circulation of this coastal region poses a challenge for numerical models. In particular, the pronounced front separating the fresh water of the NCC from Atlantic waters has proven to be difficult to reproduce (e.g. Budgell, 2005; Lien et al., 2013; Røed and Albretsen, 2007; Winther and Evensen, 2006). In this thesis we apply high-resolution models constrained by observations that are assimilated into the model fields to produce circulation estimates.

2.2 Data Assimilation

The use of data assimilation (DA) to prepare high-quality initial conditions for numerical weather prediction (NWP) models is of key importance to ensure reliable weather forecasts. DA is also an essential tool for reconstructing the atmospheric or oceanic state during a past period in a consistent way. When DA is used in this way the resulting data set is called a reanalysis. Such data sets provide long time series of high resolution that cannot be matched by observations alone, and are invaluable for the scientific community.

As DA in ocean models largely builds on development made within the field of NWP, the information presented in this section will be given in this context. This section leans on several texts on data assimilation, such as Blayo et al. (2014); Bouttier and Courtier (1999); Fisher (2010); Kalnay (2003); Talagrand (1997) .

The first approaches to adjust initial conditions for the purpose of weather forecasting include adjusting weather maps by hand according to the available observations, and for the first generation of numerical models, interpolation of the observations to the model grid. Prior to the satellite era, observations tended to be unevenly distributed in space, with many observations over populated areas and hardly any over uninhabited parts of the world. This motivated the development of methods which combined a background state from the numerical model itself with the available observations (Bergthorsson and Döös, 1955).

The development of modern DA techniques was motivated by two important advances in NWP. First, the famous discovery by Lorenz (1963) that even small perturbations (on the order of roundoff errors) in the initial condition of a dynamical system would yield different solutions. Second, the fact that primitive equation models, introduced in the early seventies, are more sensitive to their initial conditions than the first generation of numerical models. In order to obtain initial conditions that would limit the error growth and ensure a stable model run after assimilation, modern DA techniques aims to assimilate observations into the model fields in a way that not only brings the model closer to the true state, but is also consistent with the dynamics represented by the model. The latter point is important, as fast gravity-inertia wave oscillations may quickly deteriorate the model solution if the analysis state is not properly balanced.

All state-of-the-art assimilation methods build on a statistical approach, in which a background state ($\mathbf{x_b}$), observations ($\mathbf{y}$), and description of the error variances of both former terms are combined to provide the best possible description of the true state ($\mathbf{x_t}$), the so-called analysis ($\mathbf{x_a}$). "Best possible" is here defined as the state that minimizes the analysis error variance. The errors are defined as

$$\begin{aligned}
\varepsilon_a &= \mathbf{x}_a - \mathbf{x_t} \\
\varepsilon_b &= \mathbf{x}_b - \mathbf{x_t} \\
\varepsilon_o &= \mathbf{y} - H(\mathbf{x_t}),
\end{aligned}$$

where H is an observation operator that maps between model space and observation space. Assuming that the mean errors of both observations and background state are zero, and that there is no correlation between the errors of the two, the best linear unbiased estimate can be defined as

$$\mathbf{x}_a = \mathbf{x}_b + \mathbf{K}(\mathbf{y} - H(\mathbf{x}_b)), \tag{2.1}$$

where the model state variables, $\mathbf{x}_{a,b}$ consist of all prognostic model variables at every grid point, and $\mathbf{K}$ is the gain matrix that determines the weighting of observations and background state. H may be a simple interpolation operator, or in addition contain a function relating model variables to an observed quantity, e.g. radial current as measured by a HF radar. H is often assumed to be perfect, i.e. no errors are introduced in the mapping from model space to observation space. It is also often assumed that the observation operator (H) can be linearized, so that for a small increment $\delta\mathbf{x}$ to $\mathbf{x}$ we have

$$H(\mathbf{x}+\delta\mathbf{x}) = H(\mathbf{x}) + \mathbf{H}(\delta\mathbf{x}). \tag{2.2}$$

When a solution to Eq. (2.1) is sought by finding the analysis that yields the smallest value for the analysis error variance, $\mathbf{K}$ is the Kalman gain matrix

$$\mathbf{K} = \mathbf{B}\mathbf{H}^T(\mathbf{H}\mathbf{B}\mathbf{H}^T + \mathbf{R})^{-1}, \tag{2.3}$$

where $\mathbf{R}$ and $\mathbf{B}$ are the covariance matrices for the observation errors and the model background errors, respectively. As the full covariance matrix for the model background errors is usually not well known, and is too large to be used in practice, $\mathbf{B}$ can only be approximated. For the case of uncorrelated errors, $\mathbf{R}$ is easier to specify, and is commonly assumed to be known. It consists of two parts: the instrumental error describing the expected accuracy of the measurement, and the error of representativeness which relates to how well the observed quantity can be represented in the model. E.g., the current at a given location in the ocean may be measured with high precision, however, if this observation is to be assimilated into a model of finite resolution, the observed current may be a poor measure of the currents resolved by the model, and thus have a large representation error.

Currently, the methods for solving the DA problem within the context of NWP can be divided in two categories: ensemble methods, in which the ensemble spread is used to specify $\mathbf{B}$, and variational methods. The 4D-Var method applied in this thesis belongs to the latter category. Variational methods can be described by a maximum likelihood approach, as the idea is to find the most probable state given the available information provided by the observations and the background: $\mathbf{x}_a = \max p(\mathbf{x}|\mathbf{y} \wedge \mathbf{x_b})$, where p is a probability density function. According to Bayes theorem, we have

$$p(\mathbf{x}|\mathbf{y} \wedge \mathbf{x}_b) = \frac{p(\mathbf{y} \wedge \mathbf{x}_b|\mathbf{x})p(\mathbf{x})}{p(\mathbf{y} \wedge \mathbf{x}_b)}, \tag{2.4}$$

in which the denominator is independent of $\mathbf{x}$, and since $\mathbf{x}$ is unknown all choices of $\mathbf{x}$ have equal probability, rendering $p(\mathbf{x})$ a constant. Thus, the left hand side of Eq. (2.4) is proportional to the remaining terms on the right. When applying the assumption of uncorrelated observation and background errors, we get the expression

$$p(\mathbf{x}|\mathbf{y} \wedge \mathbf{x}_b) \propto p(\mathbf{y}|\mathbf{x})p(\mathbf{x}_b|\mathbf{x}). \tag{2.5}$$

Eq. (2.5) may be expressed in the form of a cost function, and when simultaneously using the fact that the logarithm is a monotonic function, we get the following expression:

$$J(\mathbf{x}) = -\log(p(\mathbf{y}|\mathbf{x})) - \log(p(\mathbf{x}_b|\mathbf{x})) + const. \tag{2.6}$$

The analysis is now the value of $\mathbf{x}$ that minimizes the cost function. In the context of variational DA, $\mathbf{x}$ is usually referred to as the control vector. As noted by Fisher (2010), the probability density functions of the background and observations can, for the case of Gaussian error distributions, be modeled as:

$$p(\mathbf{x}_b|\mathbf{x}) = b\,\exp\,[\frac{1}{2}(\mathbf{x}-\mathbf{x}_b)^T\mathbf{B}^{-1}(\mathbf{x}-\mathbf{x}_b)],$$
$$p(\mathbf{y}|\mathbf{x}) = o\,\exp\,[\frac{1}{2}(\mathbf{y}-H(\mathbf{x}))^T\mathbf{R}^{-1}(\mathbf{y}-H(\mathbf{x}))],$$

where b and o are normalization factors (Bouttier and Courtier, 1999). Thus, by choosing an appropriate value for the constant in Eq. (2.6), we arrive at the cost function for three dimensional variational DA, 3D-Var:

$$J(\mathbf{x}) = \frac{1}{2}(\mathbf{x}-\mathbf{x}_b)^T\mathbf{B}^{-1}(\mathbf{x}-\mathbf{x}_b) + \frac{1}{2}(\mathbf{y}-H(\mathbf{x})^T\mathbf{R}^{-1}(\mathbf{y}-H(\mathbf{x})). \tag{2.7}$$

The notation 3D is used to emphasize the fact that the observation operator only contains spatial mapping between model and observations. It is common practice to use observations taken during a period of time, referred to as an assimilation window, and evaluate them as if they were valid at the same time. An expansion of H to include temporal mapping essentially yields the cost function of 4D-Var. However, as information is propagated in time according to physical laws, this must be reflected in the observation operator. It is convenient to group observations taken at the same time k and evaluate the cost function in the following form:

$$J(\mathbf{x}) = \frac{1}{2}(\mathbf{x}-\mathbf{x}_b)^T\mathbf{B}^{-1}(\mathbf{x}-\mathbf{x}_b) + \frac{1}{2}\sum_{k=0}^{K}(\mathbf{y}_k-G_k(\mathbf{x}_k))^T\mathbf{R}_k(\mathbf{y}_k-G_k(\mathbf{x}_k)). \tag{2.8}$$

The new observation operator G_k now includes an integration of a the numerical model from $t = 0$ to the time of evaluation, k, and takes the form $G_k = H_k M_{0\rightarrow k}$, where M is the numerical model. This term also appears in its transposed form in Eq. (2.8), implying that the model must be run backwards, i.e. from the end of the assimilation window and back to its beginning. For a full numerical model, with many highly non-linear processes, this is virtually impossible. If we assume that M can be approximated by a linearization around the solution of the full non-linear model state over the course of the assimilation window by providing a tangent linear model (TLM), the problem is possible to solve. The transpose of the TLM, the so-called adjoint model (ADJ) can be derived, making integration backwards in time possible.

As a consequence of the assumption that H does not introduce any errors, the formulation of 4D-Var discussed so far assumes a perfect forecast model: given perfect initial conditions and forcing, the model will produce a perfect forecast. This formulation is called strong constraint 4D-Var. In reality though, errors do arise from imperfect model physics, parametrization of subgrid processes, numerical schemes etc. The assumption of a perfect model may be relaxed to yield weak constraint 4D-Var, with the addition of an extra term in the cost function, containing information on the model error and its covariance matrix. Describing the latter is, however, a non-trivial task.

To sum up the above, the following assumptions are made for strong constraint 4D-Var:

- The mean errors of both observations and the background are zero.
- There is no correlation between the observation errors and the background errors.
- The observation errors are uncorrelated in space and time.
- The errors are normally distributed (Gaussian).
- The forecast model is perfect — no error introduced by the observation operator.
- The evolution of the model over the assimilation window is approximately linear.
- The background is close to the true state.

4D-Var has the distinct advantage of evaluating the observations at their correct time, and through integration of both the TLM and the ADJ, the information is propagated backward and forward in time in accordance with the (linearized) model physics, allowing for an observation to affect the state upstream from its location as well as downstream. The drawback is the fact that it is necessary to maintain three separate model codes; the non-linear (NLM), the TLM and the ADJ. 4D-Var is also computationally demanding, particularly the ADJ. The tangent linear assumption poses a limit on the assimilation window length, as non-linearities will dominate the solution of the ocean model on longer time scales. This issue is particularly important for high-resolution models, as non-linear processes are better resolved. Weak constraint DA has the potential to compensate for the breach of the tangent linear assumption, allowing for longer windows.

Section 3.2 will cover how 4D-Var is implemented in ROMS, and how the cost function is minimized.

2.3 Observations

Observations are an essential component of an ocean assimilation system, but also provide invaluable information for validating non-assimilative models such as hindcasts and for determining the skill of an ocean forecast system. In general, observations are divided into two main categories based on how the measurements are obtained: in-situ or by the means of remote sensing.

For the case of the ocean, observations obtained through remote sensing are limited to the surface. In this thesis we have used two different types of remotely sensed observations: satellite sea surface temperature (SST) and HF radar surface currents. As the latter is the focus of paper I and II, and serves as a part of the observational network in paper IV, a detailed description of HF radars is given later in this section.

A common way to distinguish different SST products is by the level of processing the raw data has undergone to produce the end product. The instruments mounted on the satellites do not directly measure the surface temperature, and some sensors are unable to see through clouds. In order to provide an estimate of the SST with neither temporal nor spatial gaps it is thus necessary to combine observations from different sensors at different times. This can be done by applying optimal interpolation techniques (e.g. Donlon et al., 2012), and SST products derived this way are called level 4 (L4) products. However, this processing method causes some details (e.g. fronts) visible in the raw observations to be lost or smoothed out. In order to provide data everywhere, the resolution in such products must also be coarser than that of lower level products. These constraints should be reflected in the error of representativeness provided to the assimilation system. In paper III two different L4 products of different horizontal resolutions and geographical coverage were used for assimilation, while in paper IV we used a level 2 (L2) product for the same purpose. The L2 product consists of SST observations from individual satellite passes projected onto a grid with 1.5 km resolution. As the observations are derived from infrared sensors, data are only available during cloud free conditions. When using this data set we take advantage of 4D-Var's capability to propagate information in time according to the linearized model physics. This could be beneficial for the multivariate response of the DA system, as the movement of fronts and eddies can be inferred from subsequent satellite passages. On the other hand, SST data are only available during cloud free conditions, which could cause a "fair weather" bias of the modeled temperature.

In addition to HF radar currents and SST, in-situ observations of temperature and salinity have also been used for assimilation. In-situ observations provide the only source of information of the sub-surface ocean, and contrary to observations obtained by remote sensing, the number of such observations are limited. The majority of the in-situ temperature and salinity observations used in this thesis are obtained by profiling CTDs during research cruises, but observations from a wide range of platforms such as Argo profiling floats, moorings, gliders, FerryBoxes, and along-track thermosalinograph measurements from vessels are also included in the data sets used for assimilation.

In paper I and paper II, in-situ measurements of ocean currents obtained by two different means are used for comparison with HF radar currents and as means for validation of the ocean model. A mooring with two acoustic Doppler current profilers (ADCP) provided a time series of the Eulerian vertical current profile for a location within the area covered by the HF radars. Two types of surface drifters, iSphere drifters, which are half-submerged, and self locating datum marker buoys (SLMDB), with a cross-shaped sail with average depth 0.7 m below the surface, were used to provide observations of the Lagrangian surface currents.

HF radars measure ocean currents based on the backscatter from surface waves (Stewart and Joy, 1974). The operating frequencies of HF radars lies within the range of 3-50MHz, which is close to the frequency bands of AM and FM radio (Paduan and Washburn, 2013). Depending on the operating frequency, HF radars can measure currents up to 200 km offshore, and they can operate under all weather conditions. As such, they provide an excellent platform for observing ocean surface currents over extensive areas in coastal regions.

The basic operation principle of a HF radar is to transmit an electromagnetic wave of wavelength λ, and receive the signal that is backscattered from the ocean surface. Backscattering occurs from waves of wavelength $\lambda/2$ that are traveling in a radial direction to or from the antenna. This is known as Bragg scattering, and will result in two distinct peaks in the frequency spectrum of the received signal, one caused by waves moving away from the antenna and one by waves moving towards it. In the absence of an underlying ocean current, and under the assumption of deep water waves, the peaks will be at frequencies corresponding to a Doppler shift due to the phase speed of the surface waves that reflected the signal, more specifically at $f_b = \pm g/\pi\lambda$. However, in the presence of an ocean current there will be an additional shift in frequency, Δf. The

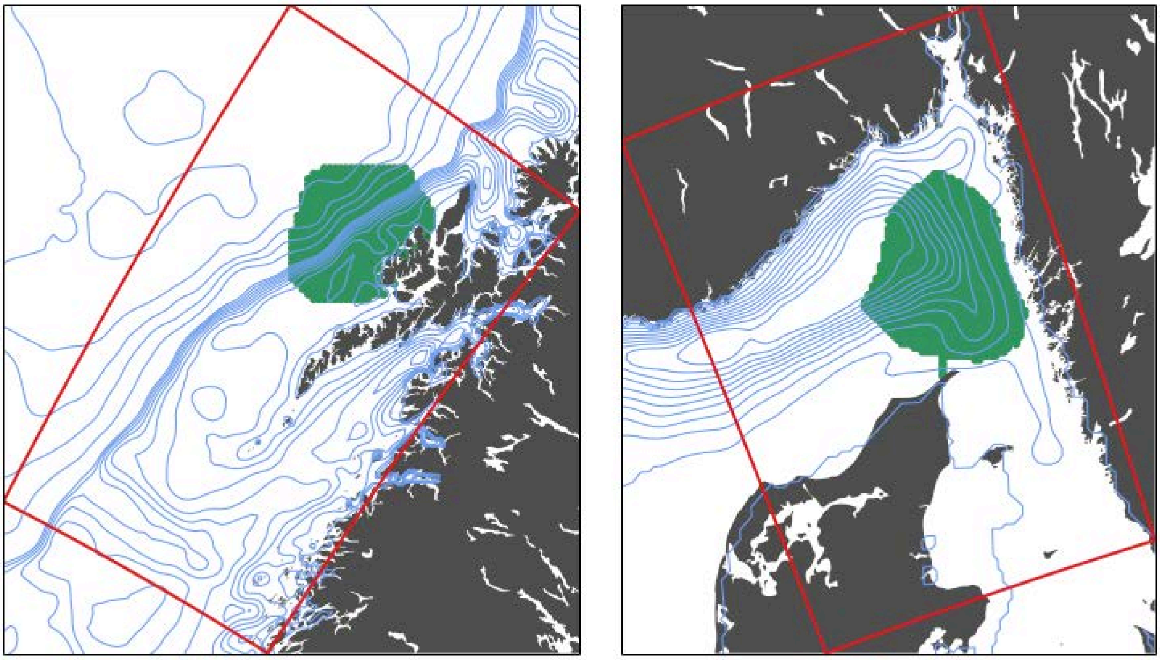

Figure 2.2: The coverage of the HF radar networks used in paper II (left) and paper IV (right). The model domains are shown in red, while the contours indicate the bathymetry.

radial velocity component (v_r) of the ocean current can thus be found by subtracting the theoretical phase speed (c_p) from the phase speed derived from the observed signal (c_p^{obs})

$$v_r = c_p^{obs} - c_p. \tag{2.9}$$

When the same patch of the ocean is simultaneously observed by two or more HF radars, their respective measured radial current components may be combined to form an estimate of the total current, i.e. the components in northerly and easterly directions (Gurgel, 1994). The level of precision of the current estimate will depend on the angle between the respective radials, with higher uncertainties as the angles become more and more parallel through geometric dilution of precision (Chapman et al., 1998).

While radial currents may be used directly for data assimilation through the specification of an observation operator, maps of total currents from a network of HF radars can provide information for monitoring ocean currents in real-time.

In this thesis observations from two HF radar networks, one in Vesterålen and one on the western coast of Sweden, are used. The operating frequencies were 13.525 MHz and 13.5 MHz, respectively. Fig. 2.2 shows the areas covered by the HF radar networks. Paper I uses radial currents from one of the antennas in Vesterålen, while the total currents provided by this network are assimilated in paper II. In paper IV the total currents from the Swedish HF radar network are assimilated.

Chapter 3

Tools and Methods

3.1 ROMS

The model experiments are performed with the Regional Ocean Modeling System (ROMS). The development of ROMS is led by groups at Rutgers University and University of California, Los Angeles (UCLA), with contributions from users around the world. ROMS is a hydrostatic, primitive equation ocean model, which uses split-explicit time stepping to solve the momentum equations (Shchepetkin and McWilliams, 2005, 2009). ROMS applies the Boussinesq approximation, meaning that density differences only affect vertical accelerations through the buoyancy term. It applies terrain-following vertical coordinates, which allows for higher resolution at depths of particular interest, such as the mixed layer. This coordinate system falls within the sigma type vertical coordinate, for which pressure gradient errors may be a problem, particularly in the presence of steep topography. Numerical algorithms to reduce this issue have been implemented in ROMS (Shchepetkin and McWilliams, 2003).

3.2 ROMS-4DVAR

A 4D-Var assimilation system has been developed for ROMS, mainly through efforts by a group at University of California, Santa Cruz. This section aims to give a brief overview of the methods applied in the scientific papers; a more thorough description of the DA system and its performance is given in Moore et al. (2011a,b,c).

The control vector in ROMS-4DVAR consists of the prognostic variables (surface elevation, barotropic and baroclinic velocities, temperature, and salinity) at the start of the assimilation window (t_0), with the possibility of expansion to include the surface forcing and lateral boundary conditions.

ROMS comes with three different implementations of 4D-Var. In this thesis we have used two: the incremental strong constraint 4D-Var (IS4DVAR) and the 4D physical space statistical analysis system (4DPSAS). To keep notation simple and in accordance with that of Sec. 2.2, the expansion of the control vector by surface forcing and boundary conditions will not be considered here.

The algorithms are based on departures from the background state, meaning that the state vector consists of the sum of two terms: the background state $(\mathbf{x}_b(t_0))$ and an increment $(\delta\mathbf{x}(t_0))$ that is assumed to be small compared with the background. This is in accordance with the assumption that the background state is close to the true state. In both IS4DVAR and 4DPSAS, an iterative approach is used to find the solution that minimizes the cost function. During these iterations, the so-called inner-loops (denoted by subscript m in the following), the TLM and ADJ are used to propagate information forward and backward in time. To speed up convergence it is possible to update the non-linear solution according to an intermediate analysis increment and repeat the inner-loops with a linearization around the updated model state. Such re-linearizations are termed outer-loops, and denoted by the superscript k in the following. The use of an outer-loop can to a certain degree compensate for non-linearities within the assimilation window. The number of outer- and inner-loops to be used during the minimizations of the cost function are, in ROMS-4DVAR, most commonly specified by the user a priori.

IS4DVAR

Incremental, strong constraint 4D-Var follows the approach suggested by Courtier et al. (1994). The cost function is minimized using the following approach:

1. An integration of NLM over the assimilation window, using $\mathbf{x_b}(t_0)$ as initial conditions. During this integration the innovations between the observations and the background, $\mathbf{d} = \mathbf{y} - H(\mathbf{x}_b)$, are calculated. The inner-loops iterations are started with $\delta\mathbf{x}_1^k = 0$.

    a) An integration of TLM to compute the cost function $J(\delta\mathbf{x})$ and the increments $\mathbf{H}\delta\mathbf{x}_m^k$.
    b) An integration of ADJ to compute $\nabla J(\delta\mathbf{x})$.
    c) Minimization using a conjugate gradient approach.
    d) Update the analysis increment $\delta\mathbf{x}_m^k$.

2. An integration of NLM with updated initial conditions $\mathbf{x}(t_0) = \mathbf{x_b}(t_0) + \delta\mathbf{x}_m^k(t_0)$

Here, steps a–d are the inner-loops that are repeated several times, ideally until the solution has converged. When all inner-loops have been completed and step 2 has been executed, the inner-loops are repeated if the number of outer-loops is set to be more than one. In contrast to the more common approach of updating both innovations and the linearization model during outer loops, ROMS-4DVAR follows the approach of Bennett (2005), keeping the values obtained for the innovations ($\mathbf{d}$) during the first outer-loop for all later outer-loops (Moore et al., 2011c). The last iteration of step 2 yields the final analysis $\mathbf{x}_b + \delta\mathbf{x}_M^K$.

In IS4DVAR the value of the cost function decreases monotonically with the number of inner-loops. Solutions that minimize the cost function are sought after in the space spanned by the control vector, and thus always correspond to a physical solution. This means that even if the number of iterations is insufficient to ensure convergence of the solution, the result will be meaningful and closer to the true state than the first guess.

4DPSAS

The increments to the analysis, for simplicity named $\delta\mathbf{x}_a$, can according to Eqs. /2.1)-(2.3) be expressed as

$$\delta\mathbf{x}_a = \mathbf{x}_a - \mathbf{x}_b = \mathbf{B}\mathbf{H}^T(\mathbf{H}\mathbf{B}\mathbf{H}^T + \mathbf{R})^{-1}\mathbf{d}. \tag{3.1}$$

It can be further simplified by defining $\mathbf{w}_a = (\mathbf{H}\mathbf{B}\mathbf{H}^T + \mathbf{R})^{-1}\mathbf{d}$, whose dimension is the number of observations, and Eq. (3.1) is referred to as the dual formulation for 4D-Var, while 4D-Var in the form of the previously discussed IS4DVAR is called the primal formulation. For the case of an ocean DA system, the number of observations is typically much smaller than the number of entries in the state vector, thus searching for a solution in observation space rather than in model space may be advantageous. A new cost function can be defined as:

$$I(\mathbf{w}) = \frac{1}{2}\mathbf{w}^T(\mathbf{H}\mathbf{B}\mathbf{H}^T + \mathbf{R})\mathbf{w} - \mathbf{w}^T\mathbf{d}. \tag{3.2}$$

This is the cost function of 4DPSAS. Contrary to the primal formulation of 4D-Var, the dimension of the control vector in 4DPSAS remains the same when weak constraint is applied as the number of observations does not change. This formulation is thus much better suited when model errors are taken into account. The solution in 4DPSAS is found using the following iterative process:

1. An integration of NLM with initial conditions $\mathbf{x}(t_0) = \mathbf{x}_b(t_0)$, during which $\mathbf{d}$ is calculated. Set $\mathbf{w}_1^k = \mathbf{d}$.
    a) Integrate ADJ to compute $\mathbf{H}^T\mathbf{w}_m^k$.
    b) Multiply by the covariance matrix to get $\mathbf{B}\mathbf{H}^T\mathbf{w}_m^k$.
    c) Integrate TLM to compute $\mathbf{H}\mathbf{B}\mathbf{H}^T\mathbf{w}_m^k$.
    d) Apply a conjugate gradient algorithm to get the cost function $I(\mathbf{w})$, which gives an estimate of $\mathbf{w}_{m+1}^k$.
2. Integrate ADJ to compute $\mathbf{H}^T\mathbf{w}_{m+1}^k$.
3. Multiply by the background covariance matrix to get $\mathbf{B}\mathbf{H}^T\mathbf{w}_{m+1}^k$.
4. An integration of NLM with updated initial conditions $\mathbf{x}(t_0) = \mathbf{x_b}(t_0) + \delta\mathbf{x}_k(t_0)$.

Similar to IS4DVAR, steps a–d are the steps performed in the inner-loops, while steps 1–4 are performed in the outer-loops. The final analysis is given by the last iteration of step 4.

Chapter 4

Summary and future perspective

In this PhD thesis we have investigated how the use of a 4D-Var ocean assimilation system impacts the circulation in high-resolution coastal models.

- **Paper I**: Investigates whether HF radar observations of currents include Stokes drift and what depth they represent. This is important to determine the suitability of this observing system for use in DA.
- **Paper II**: Evaluates the ability of the 4D-Var ocean assimilation system to realistically reproduce energetic slope currents by assimilating HF radar currents and CTD hydrography.
- **Paper III**: Examines how assimilation of hydrography affect the upper ocean circulation estimates, and the potential consequences for particle transport.
- **Paper IV**: Combining the experience from paper I-III, a reanalysis of the Kattegat-Skagerrak is produced and used to investigate the mechanisms causing variability in the onset of the Norwegian Coastal Current.

4.1 Summary of papers

Paper I: Comparison of HF radar measurements with Eulerian and Lagrangian surface currents

Röhrs, J., A. K. Sperrevik, K. H. Christensen, G. Broström, and Ø. Breivik

The aim of this study was to determine whether HF radar observations of currents include the Stokes drift, which is a mean drift velocity in the waves, and to identify which depth the observed currents correspond to. In order to use HF radar currents for data assimilation it is essential to know what the observations actually represent. To achieve this goal an observational campaign measuring surface currents by three different means was conducted: a HF radar antenna, an ADCP sampling vertical profiles of the Eulerian current, and two types of surface drifters sampling the Lagrangian current field. In addition, wave data were provided by a pressure sensor on the ADCP rig. According to the results of Röhrs et al. (2012) this observational system allows us to distinguish between Eulerian and Lagrangian currents. Our results showed good agreement between HF radar and Eulerian ADCP currents, and the best agreement with currents from surface drifters was obtained when the Stokes drift, derived from wave data, were subtracted from the drifter velocities. Furthermore, our results showed that the HF radar currents represent a vertical average of currents, weighted by an exponential function with an e-folding scale in the range between 0.8 and 1.4 m, meaning that 80% of the signal comes from the upper meter. This is in accordance with the theoretical calculations by Stewart and Joy (1974).

Paper II: Constraining energetic slope currents through assimilation of high-frequency radar observations

Sperrevik, A. K., K. H. Christensen, and J. Röhrs

In this paper the impact of assimilation of HF radar total currents in a high-resolution model is investigated in order to determine the potential effect of such observations on the subsequent circulation estimates. The ability of the assimilation system to reproduce an energetic, non-linear slope current is first investigated by assimilating synthetic current observations in an idealistic model configuration mimicking the complex topography of the Lofoten/Vesterålen shelf, using different configurations of the assimilation system. Secondly, a series of assimilation experiments using a realistic model setup were performed:

- Assimilating only HF radar currents.
- Assimilating only CTD hydrography.
- Assimilating both HF radar currents and CTD hydrography.

For comparison, a model simulation without assimilation was also produced. Based on each updated initial state, forecast simulations of 5 days were conducted, and the results of these were compared with complementary observations from the SLMDB surface drifters and the ADCP mooring. The results showed positive impact of assimilation of HF radars on the forecast skill of upper ocean transport, with further improvement obtained when CTD hydrography was included. The CTD observations alone did, however, not provide sufficient information to constrain the circulation. This underlines the value of assimilating complementary observation sources.

Paper III: Impact of data assimilation on Eulerian versus Lagrangian estimates of upper ocean transport

Sperrevik, A. K., J. Röhrs, and K. H. Christensen

A common application of regional hindcasts is transport studies of biological quantities such as fish eggs and larvae. The coastal dynamics are, however, often not properly resolved in such hindcasts. This may result in erroneous description of the transport. As demonstrated by Myksvoll et al. (2014), vertical stratification impacts transport of cod eggs of different densities, highlighting the importance of realistic stratification in the model archives used for these purposes.

In this study a reanalysis for the first six months of 1984 was produced by assimilating SST and in-situ hydrography observations using the same model application as in paper II. This period was chosen as the Institute of Marine Research (IMR) conducted extensive field campaigns during the spring of 1984 to assess the stock of Northeast

Arctic cod, which have their main spawning grounds inside Vestfjorden, providing a unique data set of in-situ profiles. The changes in upper ocean circulation caused by improved representation of the water mass distribution, both in the vertical and the horizontal, are investigated by evaluating the impact on the Eulerian and Lagrangian surface currents. The results show similar distribution of the Eulerian current speeds compared with a traditional hindcast generated with the same model configuration, while the Lagrangian current speeds have overall higher kinetic energy in the reanalysis. One possible explanation for these differences is that the increased effective model resolution caused by stronger stratification allows for more small-scale circulation features to be generated.

Paper IV: On the variability in the onset of the Norwegian Coastal Current

Christensen, K. H., A. K. Sperrevik, and G. Broström

The most prominent feature of the coastal circulation along the coast of Norway is the Norwegian Coastal Current (NCC). It originates in the Skagerrak as a continuation of the outflow from the Baltic Sea, and flows northwards along the coast. Thus, it has profound impact on the environmental conditions all along the Norwegian coast, and a good description of this current is therefore of uttermost importance for coastal models in Norway.

In this study we generate a reanalysis of the circulation in Kattegat-Skagerrak with a horizontal resolution of 1 km, covering the period October 2014 - November 2015. The observational data set used consist of in-situ observations from multiple sources, high-resolution SST, and surface currents provided by two HF radar antennas on the Swedish coast. The reanalysis is used to investigate the variations in the onset of the NCC with emphasis on the response to large-scale wind forcing, and to evaluate how well the circulation correspond with conceptual models described in the literature. Our results reveal that the local wind forcing explains 75% of the variability of the transport in NCC.

The impact of different observation types on the transport in the NCC is evaluated using adjoint techniques as described in Moore et al. (2011b); Neveu et al. (2016). The results show similar impact of SST and HF radar currents observations, even though the HF observations are too far away from the section to directly observe the transport. Normalizing the impacts by the number of observations in each category reveals, however, that in-situ data by far have the largest impact per individual observation.

4.2 Perspectives

Adjusting the model state by the means of data assimilation can significantly improve model skill, both directly as well as implicitly. The result of paper III is an example of the latter: the first baroclinic Rossby radius is increased as a consequence of improved stratification achieved through assimilating in-situ profiles of temperature and salinity. As this scale is linked to the scale of boundary currents, fronts and eddies, an increase of the first baroclinic Rossby radius implies an increase in the scale of such circulation features as well. Thus, the model's ability to generate such features is affected.

The oceanic observational network is insufficient to properly constrain the circulation, especially for the case of high-resolution coastal models. This advocates for the use of advanced DA techniques such as the 4D-Var methods applied in the papers in this thesis (Talagrand, 1997), as the integrations of the linearized models backward and forward in time allows an observation to influence the ocean state both upstream and downstream of its actual location, and the (linearized) model physics ensure a multivariate response to each available observation.

The positive effect of complementing observations of the near-surface flow field with CTD profiles, as discussed in paper II, and the observation impact calculations performed in paper IV, which show contributions from all assimilated observation types on increments to the transport of the NCC, are in agreement with Oke et al. (2015a), who conclude that there are currently no redundant observation sources in ocean DA. These results provide motivation for a continued effort to include data from both existing and emerging observational platforms in future studies and operational forecast models. An important information source we have not taken advantage of in this thesis is sea surface height from satellite altimeters, which could provide valuable information on the large scale circulation patterns and complement HF radar currents. However, satellite altimetry products suffer from high uncertainties in the near-coastal zone (Cipollini et al., 2010), and particular care is required when including such data in high-resolution coastal models. One promising prospect in this regard is the planned SWOT mission (see https://swot.jpl.nasa.gov/mission/), which aims to provide high-resolution measurements of the sea surface height. Furthermore, the transition from assimilating HF radar total currents to direct assimilation of the radial current velocities is compelling for several reasons. Firstly, processing of the radials to total vectors introduce additional uncertainties to the observations. Secondly, the use of radials will expand the area where current observations are available. Direct assimilation of radials is also less vulnerable to failures in the infrastructure, as one antenna alone provide information that can be used by the assimilation system.

The encouraging results of the studies included in this thesis aside, there are still many aspects of the ocean DA system that can be improved and several challenges to be overcome, some general and some specific to the case of an operational DA forecast application. The performance of the DA system is sensitive to the specification of observational errors and the background error covariance matrix, both which are assumed to be known a priori. In our studies we have used an estimate of $\mathbf{B}$ based on climatology calculated from multi-year simulations of the nonlinear model, a common approach in variational DA. This approach does not take the so-called errors of the day into account, and several studies have shown improvement of the analysis when static background errors covariances are combined with flow-dependent error covariances obtained from ensemble simulations to form $\mathbf{B}$ (e.g. Bannister, 2017; Buehner, 2005; Gustafsson and Bojarova, 2014). The observational errors are also assumed known and explicitly specified to the system, and improvements to this component can certaintly be made. Desroziers et al. (2005); Neveu et al. (2016) provide a method that can be used to improve the specification of $\mathbf{R}$.

The 4D-Var DA scheme used in this thesis are computationally costly, it is approximately 20-30 times as expensive to run as a stand-alone forecast model. This poses a challenge, especially for operational DA, and compromises to the design of the system in terms of assimilation window length and the number of iterations used to obtain the minimum value of the cost function might be necessary. A common approach in many NWP centers is to perform the inner-loops at lower resolution than the non-linear model. The implementation of this approach in ROMS-4DVAR, holds the potential to reduce the computational cost significantly. Another challenge to operational DA is the delay with which many in-situ observations are made available. Considering the sparse number of such observations available for coastal circulation models, one might consider taking advantage of the long memory of the ocean and use seasonal reanalyses to re-initialize the operational DA system. Such seasonal reanalyses can also provide useful data sets for e.g. biological applications, which are often focused on evaluating a season in retrospect to investigate the conditions for e.g. recruitments to fish stocks and primary production.

References

Ådlandsvik, B. and S. Sundby, 1994: Modelling the transport of cod larvae from the Lofoten area. *ICES Marine Science Symposia*, Vol. 198, 379–392. 1.1

Bannister, R. N., 2017: A review of operational methods of variational and ensemble-variational data assimilation. *Q. J. R. Meteorol. Soc.*, **143 (703)**, 607–633, doi:10.1002/qj.2982. 4.2

Bennett, A. F., 2005: *Inverse Modeling of the Ocean and Atmosphere*. Cambridge University Press. 3.2

Bergthorsson, P. and B. R. Döös, 1955: Numerical Weather Map Analysis. *Tellus*, **7 (3)**, 329–340, doi:10.3402/tellusa.v7i3.8902. 2.2

Blayo, E., M. Bocquet, E. Cosme, and L. F. Cugliandolo, 2014: *Advanced Data Assimilation for Geosciences*. 2.2

Blockley, E. W., M. J. Martin, A. J. McLaren, A. G. Ryan, J. Waters, D. J. Lea, I. Mirouze, K. A. Peterson, A. Sellar, and D. Storkey, 2014: Recent development of the Met Office operational ocean forecasting system: an overview and assessment of the new Global FOAM forecasts. *Geosci. Model Dev.*, **7 (6)**, 2613–2638, doi:10.5194/gmd-7-2613-2014. 1.1

Bouttier, F. and P. Courtier, 1999: Data assimilation concepts and methods. ECMWF, Lecture Notes NWP Course. 2.2, 2.2

Breivik, Ø. and A. A. Allen, 2008: An operational search and rescue model for the Norwegian Sea and the North Sea. *J. Mar. Syst.*, **69 (1–2)**, 99–113, doi:10.1016/j.jmarsys.2007.02.010. 1.1

Broström, G., A. Carrasco, L. R. Hole, S. Dick, F. Janssen, J. Mattsson, and S. Berger, 2011: Usefulness of high resolution coastal models for operational oil spill forecast: the "Full City" accident. *Ocean Sci.*, **7 (6)**, 805–820, doi:10.5194/os-7-805-2011. 1.1

Budgell, W. P., 2005: Numerical simulation of ice-ocean variability in the Barents Sea region. *Ocean Dyn.*, **55 (3-4)**, 370–387, doi:10.1007/s10236-005-0008-3. 2.1

Buehner, M., 2005: Ensemble-derived stationary and flow-dependent background-error covariances: Evaluation in a quasi-operational NWP setting. *Q.J.R. Meteorol. Soc.*, **131 (607)**, 1013–1043, doi:10.1256/qj.04.15. 4.2

Chapman, R. D., L. K. Shay, and H. C. Graber, 1998: On the accuracy of HF radar surface current measurements: intercomparisons with ship-based sensors. *Oceanographic Lit. Rev.*, **3 (45)**, 578. 2.3

Cipollini, P., J. Benveniste, J. Bouffard, W. Emery, C. Gommenginger, D. Griffin, J. Høyer, K. Madsen, F. Mercier, L. Miller, et al., 2010: The Role of Altimetry in Coastal Observing Systems. European Space Agency, 166–176, doi:10.5270/OceanObs09.cwp.16. 4.2

Courtier, P., J.-N. Thépaut, and A. Hollingsworth, 1994: A strategy for operational implementation of 4d-Var, using an incremental approach. *Q. J. R. Meteorolog. Soc.*, **120 (519)**, 1367–1387, doi:10.1002/qj.49712051912. 3.2

Desroziers, G., L. Berre, B. Chapnik, and P. Poli, 2005: Diagnosis of observation, background and analysis-error statistics in observation space. *Q. J. R. Meteorol. Soc.*, **131 (613)**, 3385–3396, doi:10.1256/qj.05.108. 4.2

Donlon, C. J., M. Martin, J. Stark, J. Roberts-Jones, E. Fiedler, and W. Wimmer, 2012: The Operational Sea Surface Temperature and Sea Ice Analysis (OSTIA) system. *Remote Sens. Environ.*, **116**, 140–158, doi:10.1016/j.rse.2010.10.017. 2.3

Fisher, M., 2010: Data assimilation lecture notes. ECMWF, Lecture Notes NWP Course. 2.2, 2.2

Gundlach, E. R. and M. O. Hayes, 1978: Vulnerability of coastal environments to oil spill impacts. *Mar. Technol. Soc. Rev.*, **12 (4)**. 1.1

Gurgel, K. W., 1994: Shipborne measurement of surface current fields by HF radar. *OCEANS '94. 'Oceans Engineering for Today's Technology and Tomorrow's Preservation.' Proceedings*, Vol. 3, III/23–III/27 vol.3, doi:10.1109/OCEANS.1994.364167. 2.3

Gustafsson, N. and J. Bojarova, 2014: Four-dimensional ensemble variational (4d-En-Var) data assimilation for the HIgh Resolution Limited Area Model (HIRLAM). *Nonlin. Processes Geophys.*, **21 (4)**, 745–762, doi:10.5194/npg-21-745-2014. 4.2

Hannah, C. G., C. E. Naimie, J. W. Loder, and F. E. Werner, 1997: Upper-ocean transport mechanisms from the Gulf of Maine to Georges Bank, with implications for Calanus supply. *Cont. Shelf Res.*, **17 (15)**, 1887–1911, doi:10.1016/S0278-4343(97)00048-4. 1.1

Ihaksi, T., T. Kokkonen, I. Helle, A. Jolma, T. Lecklin, and S. Kuikka, 2011: Combining Conservation Value, Vulnerability, and Effectiveness of Mitigation Actions in Spatial Conservation Decisions: An Application to Coastal Oil Spill Combating. *J. Environ. Manage.*, **47 (5)**, 802–813, doi:10.1007/s00267-011-9639-y. 1.1

Isachsen, P. E., I. Koszalka, and J. H. LaCasce, 2012: Observed and modeled surface eddy heat fluxes in the eastern Nordic Seas. *J. Geophys. Res.: Oceans*, **117 (C8)**, C08 020, doi:10.1029/2012JC007935. 2.1

Jordi, A., M. I. Ferrer, G. Vizoso, A. Orfila, G. Basterretxea, B. Casas, A. Álvarez, D. Roig, B. Garau, M. Martínez, V. Fernández, A. Fornés, M. Ruiz, J. J. Fornós, P. Balaguer, C. M. Duarte, I. Rodríguez, E. Alvarez, R. Onken, P. Orfila, and J. Tintoré, 2006: Scientific management of Mediterranean coastal zone: A hybrid ocean forecasting system for oil spill and search and rescue operations. *Mar. Pollut. Bull.*, **53 (5–7)**, 361–368, doi:10.1016/j.marpolbul.2005.10.008. 1.1

Kalnay, E., 2003: *Atmospheric Modeling, Data Assimilation and Predictability*. Cambridge University Press. 2.2

Lien, V. S., Y. Gusdal, J. Albretsen, A. Melsom, and F. B. Vikebø, 2013: Evaluation of a Nordic Seas 4 km numerical ocean model hindcast archive (SVIM), 1960-2011. *Fisken og Havet*, 7–79. 2.1

Lorenz, E. N., 1963: Deterministic Nonperiodic Flow. *J. Atmos. Sci.*, **20 (2)**, 130–141, doi:10.1175/1520-0469(1963)020<0130:DNF>2.0.CO;2. 2.2

Mitarai, S., D. A. Siegel, J. R. Watson, C. Dong, and J. C. McWilliams, 2009: Quantifying connectivity in the coastal ocean with application to the Southern California Bight. *J. Geophys. Res.: Oceans*, **114 (C10)**, C10 026, doi:10.1029/2008JC005166. 1.1

Moore, A. M., H. G. Arango, G. Broquet, C. Edwards, M. Veneziani, B. Powell, D. Foley, J. D. Doyle, D. Costa, and P. Robinson, 2011a: The Regional Ocean Modeling System (ROMS) 4-dimensional variational data assimilation systems: Part II – Performance and application to the California Current System. *Prog. Oceanogr.*, **91 (1)**, 50–73, doi:10.1016/j.pocean.2011.05.003. 3.2

———, 2011b: The Regional Ocean Modeling System (ROMS) 4-dimensional variational data assimilation systems: Part III – Observation impact and observation sensitivity in the California Current System. *Prog. Oceanogr.*, **91 (1)**, 74–94, doi:10.1016/j.pocean.2011.05.005. 3.2, 4.1

Moore, A. M., H. G. Arango, G. Broquet, B. S. Powell, A. T. Weaver, and J. Zavala-Garay, 2011c: The Regional Ocean Modeling System (ROMS) 4-dimensional variational data assimilation systems: Part I – System overview and formulation. *Prog. Oceanogr.*, **91 (1)**, 34–49, doi:10.1016/j.pocean.2011.05.004. 3.2, 3.2

Myksvoll, M. S., K.-M. Jung, J. Albretsen, and S. Sundby, 2014: Modelling dispersal of eggs and quantifying connectivity among Norwegian coastal cod subpopulations. *ICES J. Mar. Sci.*, **71 (4)**, 957–969, doi:10.1093/icesjms/fst022. 1.1, 4.1

Neveu, E., A. M. Moore, C. A. Edwards, J. Fiechter, P. Drake, W. J. Crawford, M. G. Jacox, and E. Nuss, 2016: An historical analysis of the California Current circulation using ROMS 4d-Var: System configuration and diagnostics. *Ocean Modell.*, **99**, 133–151, doi:10.1016/j.ocemod.2015.11.012. 4.1, 4.2

Oke, P. R., G. Larnicol, Y. Fujii, G. C. Smith, D. J. Lea, S. Guinehut, E. Remy, M. A. Balmaseda, T. Rykova, D. Surcel-Colan, M. J. Martin, A. A. Sellar, S. Mulet, and V. Turpin, 2015a: Assessing the impact of observations on ocean forecasts and reanalyses: Part 1, Global studies. *J. Oper. Oceanogr.*, **8**, s49–s62, doi:10.1080/1755876X.2015.1022067. 1.1, 4.2

Oke, P. R., G. Larnicol, E. M. Jones, V. Kourafalou, A. K. Sperrevik, F. Carse, C. A. S. Tanajura, B. Mourre, M. Tonani, G. B. Brassington, M. L. Henaff, G. R. H. Jr, R. Atlas, A. M. Moore, C. A. Edwards, M. J. Martin, A. A. Sellar, A. Alvarez, P. D. Mey, and M. Iskandarani, 2015b: Assessing the impact of observations on ocean forecasts and reanalyses: Part 2, Regional applications. *J. Oper. Oceanogr.*, **8**, s63–s79, doi:10.1080/1755876X.2015.1022080. 1.1

Paduan, J. D. and L. Washburn, 2013: High-frequency radar observations of ocean surface currents. *Annu. Rev. Mar. Sci.*, **5**, 115–136, doi:10.1146/annurev-marine-121211-172315. 2.3

Röhrs, J. and K. H. Christensen, 2015: Drift in the uppermost part of the ocean. *Geophys. Res. Lett.*, **42 (23)**, 2015GL066 733, doi:10.1002/2015GL066733. 1.1

Röhrs, J., K. H. Christensen, L. R. Hole, G. Broström, M. Drivdal, and S. Sundby, 2012: Observation-based evaluation of surface wave effects on currents and trajectory forecasts. *Ocean Dyn.*, **62 (10-12)**, 1519–1533, doi:10.1007/s10236-012-0576-y. 4.1

Røed, L. P. and J. Albretsen, 2007: The impact of freshwater discharges on the ocean circulation in the Skagerrak/northern North Sea area Part I: model validation. *Ocean Dyn.*, **57 (4-5)**, 269–285, doi:10.1007/s10236-007-0122-5. 2.1

Saetre, R., (Ed.) , 2007: *The Norwegian Coastal Current: Oceanography and Climate*. Fagbokforlaget, Trondheim. 2.1

Sakov, P., F. Counillon, L. Bertino, K. A. Lisæter, P. R. Oke, and A. Korablev, 2012: TOPAZ4: an ocean-sea ice data assimilation system for the North Atlantic and Arctic. *Ocean Sci.*, **8 (4)**, 633–656, doi:10.5194/os-8-633-2012. 1.1

Shchepetkin, A. F. and J. C. McWilliams, 2003: A method for computing horizontal pressure-gradient force in an oceanic model with a nonaligned vertical coordinate. *J. Geophys. Res.: Oceans*, **108 (C3)**, 3090, doi:10.1029/2001JC001047. 3.1

———, 2005: The regional oceanic modeling system (ROMS): a split-explicit, free-surface, topography-following-coordinate oceanic model. *Ocean Modell.*, **9 (4)**, 347–404, doi:10.1016/j.ocemod.2004.08.002. 3.1

———, 2009: Computational Kernel Algorithms for Fine-Scale, Multiprocess, Long-time Oceanic Simulations. *Handbook of Numerical Analysis*, Tribbia, R. M. T. a. J. J., Ed., Elsevier, Special Volume: Computational Methods for the Atmosphere and the Oceans, Vol. 14, 121–183, dOI: 10.1016/S1570-8659(08)01202-0. 3.1

Stewart, R. H. and J. W. Joy, 1974: HF radio measurements of surface currents. *Deep Sea Res.*, **21 (12)**, 1039–1049, doi:10.1016/0011-7471(74)90066-7. 2.3, 4.1

Svendsen, E., M. Skogen, P. Budgell, G. Huse, J. Erik Stiansen, B. Ådlandsvik, F. Vikebø, L. Asplin, and S. Sundby, 2007: An ecosystem modeling approach to predicting cod recruitment. *Deep Sea Res. Part II*, **54 (23–26)**, 2810–2821, doi:10.1016/j.dsr2.2007.07.033. 1.1

Talagrand, O., 1997: Assimilation of Observations, an Introduction. *J. Meteorolog. Soc. Jpn.*, **75 (1B)**, 191–209. 2.2, 4.2

Vikebø, F., C. Jørgensen, T. Kristiansen, and Ø. Fiksen, 2007: Drift, growth, and survival of larval Northeast Arctic cod with simple rules of behaviour. *Mar. Ecol. Prog. Ser.*, **347**, 207–219, doi:10.3354/meps06979. 1.1

Warner, T. T., R. A. Peterson, and R. E. Treadon, 1997: A Tutorial on Lateral Boundary Conditions as a Basic and Potentially Serious Limitation to Regional Numerical Weather Prediction. *Bull. Am. Meteorol. Soc.*, **78**, 2599–2617, doi:10.1175/1520-0477(1997)078<2599:ATOLBC>2.0.CO;2. 1.1

Winther, N. G. and G. Evensen, 2006: A hybrid coordinate ocean model for shelf sea simulation. *Ocean Modell.*, **13 (3–4)**, 221–237, doi:10.1016/j.ocemod.2006.01.004. 2.1

Chapter 5

Scientific papers

Paper I

5.1 Comparison of HF radar measurements with Eulerian and Lagrangian surface currents

Johannes Röhrs, Ann Kristin Sperrevik, Kai Håkon Christensen, Göran Broström, and Øyvind Breivik

Ocean Dynamics **65**, 679-690 (2015)

Ocean Dynamics (2015) 65:679–690
DOI 10.1007/s10236-015-0828-8

Comparison of HF radar measurements with Eulerian and Lagrangian surface currents

**Johannes Röhrs · Ann Kristin Sperrevik ·
Kai Håkon Christensen · Göran Broström ·
Øyvind Breivik**

Received: 20 November 2014 / Accepted: 3 March 2015 / Published online: 31 March 2015

Abstract High-frequency (HF) radar-derived ocean currents are compared with in situ measurements to conclude if the radar observations include effects of surface waves that are of second order in the wave amplitude. Eulerian current measurements from a high-resolution acoustic Doppler current profiler and Lagrangian measurements from surface drifters are used as references. Directional wave spectra are obtained from a combination of pressure sensor data and a wave model. Our analysis shows that the wave-induced Stokes drift is not included in the HF radar-derived currents, that is, HF radars measure the Eulerian current. A disputed nonlinear correction to the phase velocity of surface gravity waves, which may affect HF radar signals, has a magnitude of about half the Stokes drift at the surface. In our case, this contribution by nonlinear dispersion would be smaller than the accuracy of the HF radar currents, hence no conclusion can be made. Finally, the analysis confirms that the HF radar data represent an exponentially weighted vertical average where the decay scale is proportional to the wavelength of the transmitted signal.

Keywords HF radar · Stokes drift · Surface current · Surface drifter

Responsible Editor: Matthew Robert Palmer

J. Röhrs (✉) · A. K. Sperrevik · K. H. Christensen · Ø. Breivik
Norwegian Meteorological Institute, Allegaten 70,
5007 Bergen, Norway
e-mail: johannes.rohrs@met.no

G. Broström
Department of Earth Science, University of Gothenburg,
Gothenburg, Sweden

1 Introduction

High-frequency (HF) radars can measure ocean currents by using the radio wave backscatter signal from surface gravity waves (Stewart and Joy 1974). The obtained area-wide current fields have proven useful for assimilation into ocean circulation models (e.g., Zhang et al. 2010, Sperrevik et al. 2015) and as nowcasts in time critical applications like search-and-rescue operations and for oil spill mitigation (Paduan and Washburn 2013; Breivik et al. 2013).

Radio waves emitted by the HF radar are reflected through Bragg backscattering from waves at the ocean surface. The return signal experience a Doppler shift by the apparent phase velocity v_p^{obs} of the scattering waves (Bragg waves), which differs from the intrinsic phase velocity c_p in the presence of an underlying ocean current **v**. The radial component of **v** observed by the radar is

$$v^{(HF)} = c_p^{obs} - c_p. \tag{1}$$

The intrinsic phase velocity c_p is known from the dispersion relation of surface gravity waves and the frequency of the transmitted signal (Stewart and Joy 1974). Applications of HF radars typically employ the dispersion relation for linear waves, but some studies suggest that nonlinear contributions are relevant for HF radar currents (Barrick and Weber 1977; Ardhuin et al. 2009).

Due to their complex and remote measurement principle, HF radar-derived currents require a more elaborate interpretation than traditional in situ observations (Chapman and Graber 1997). Firstly, the radar receives its information from a horizontal footprint area and a vertical integration rather than measuring at a distinct location. Secondly, the estimated current has been suggested to include the entire, or parts of, the wave-induced Stokes drift (Stokes 1847), but the literature is inconsistent and sometimes unspecific on what part of the Stokes drift is included. While HF radar currents are usually interpreted as Eulerian currents (i.e., not including the Stokes drift), some studies (e.g., Graber et al. 1997; Law 2001) assume that they include the full Stokes drift. Ardhuin et al. (2009) argue that HF radar currents include only parts of the Stokes drift and compare their measurements with a "filtered Stokes drift" derived by Broche et al. (1983). Ohlmann et al. (2007) compared HF radar currents with drifter observations and underline this problem by remarking that the role of the Stokes drift "may not be reconciled consistently among platforms."

The view that HF radar currents should be Eulerian is motivated by the fact that the radar retrieves its signal from fixed regions in space, hence not following particle motions. The opposing view, that HF radar currents include the Stokes drift, implies that the waves are advected by their own mean drift velocity, which is incompatible with linear theory. Stokes drift contributions to HF radar currents are in fact motivated by a nonlinear correction to the phase velocity (Barrick and Weber 1977) with numeric values similar to the Stokes drift (Broche et al. 1983). Here, we address this problem by comparing HF radar currents to Lagrangian drifter velocities, Eulerian currents from an acoustic Doppler current profiler (ADCP), and wave data that supply the Stokes drift. Since we have ADCP current profiles with high vertical resolution near the surface, our data also allow us to assess what part of the ocean column is observed by the radar.

The main question addressed here is if HF radar measurements represent Eulerian or Lagrangian ocean currents. In the latter case, whether or not the HF radar currents contain a signal from surface waves proportional to the Stokes drift. The theoretical background with regard to the second order wave quantities is briefly presented in Section 2. Our methods and the field data are documented in Section 3. A synthesis between the ADCP, surface drifter, and wave data is presented in Section 4. Section 5 contains a discussion and interpretation of HF radar currents in terms of vertical origin and an assessment of Stokes drift contributions. Our conclusions are summarized in Section 6.

2 Theoretical background

The difference between the Eulerian velocity at fixed position and the Lagrangian (particle following) velocity is, per definition, the Stokes drift. In the presence of surface gravity waves, the Stokes drift arises because particles are for longer time exposed to the forward wave motion while its phase propagates forward (Stokes 1847). The resulting surface net drift in wave propagation direction is at the order of 10 cm s^{-1} for a wind sea with significant wave heights of 2 m (Röhrs et al. 2012). In deep water, the Stokes drift of surface gravity waves decays exponentially with depth; the decay scale depends on the wave number and is typically of the order 1 m.

2.1 Nonlinear wave effects

Barrick and Weber (1977) derived a second-order correction to the dispersion relation of surface waves using a perturbation technique. This correction is described as resulting from two separate mechanisms: (i) the "self effect," which yields a slightly higher phase velocity of monochromatic waves, and (ii) a "mutual effect" resulting from nonlinear wave-wave interactions. In the latter case, their theory predicts how one wave component influences the phase speed of other components, even in the case when the propagation directions are orthogonal to each other. These second-order effects have later been interpreted in terms of the surface Stokes drift. More specifically, a "filtered Stokes drift" can be obtained by integrating the wave spectrum multiplied by a weighting function that depends on the Bragg wavelength and the direction between the observation point and the HF radar (e.g., Ardhuin et al. 2009).

Creamer et al. (1989) revisited the problem of higher order corrections, and, using Hamiltonian theory, arrived at a result that differs from that of Barrick and Weber. They argue that products of linear and higher order terms largely cancel the second-order corrections obtained by Barrick and Weber. Janssen (2009) later confirmed this result in a more general treatment of the nonlinear problem. Janssen also points out a fundamental problem with the second-order correction terms of Barrick and Weber, namely that important integrated wave parameters such as mean square slope do not converge for high wave numbers.

2.2 Effective depth of HF radar measurements

Stewart and Joy (1974) argue that the vertical origin of the ocean current $\mathbf{v}$ causing the phase shift in Eq. 1 is related to the wavelength of the scattering Bragg waves. According to their analysis, HF radars observe a vertical average of the ocean current with exponentially decaying weight in radial radar direction as

$$v^{(HF)} = 2k_b \mathbf{e}_\theta \cdot \int_{-\infty}^{0} \mathbf{v}(z) e^{2k_b z} dz, \tag{2}$$

where z is the depth below surface, k_b is the wave number of the Bragg waves, and $\mathbf{e}_\theta$ the unit vector from the radar towards the observation, with θ being the observation direction of the radar throughout this paper. For typical HF radar transmitter frequencies, the integral in Eq. 2 gives most weight to ocean currents in the upper meter of the ocean.

3 Methods and data

To interpret HF radar currents, we use Lagrangian surface drifters, a Eulerian current meter, and surface wave data. The data was collected during a field experiment in the spring of 2013 on the shelf sea off Vesterålen, Norway (Fig. 1). The main motivation for the HF radar deployment was the assimilation of HF radar currents and hydrography profiles into an ocean model. The research vessel "Johan Hjort," at sea on the annual cod stock assessment cruise of the Institute of Marine Research, was used for deploying surface drifters. Moored current meters were deployed 3 weeks in advance before the vessel arrived in the area.

3.1 Surface drifting buoys

Two types of surface drifters were released from R/V Johan Hjort in the period 16–17 March 2013. Seven iSphere drifters and seven self-locating datum marker buoys (SLDMBs), both manufactured by MetOcean, Canada, were deployed pairwise at the locations shown in Fig. 1. By March 25, all drifters had left the area covered by the radars.

The iSpheres are half-submerged spheres with a diameter of 35 cm without a drogue. A previous experiment (Röhrs et al. 2012) showed that they are driven by the sum of the Eulerian current and the Stokes drift at the surface, with only little wind drag. The effect of the wind drag on this drifter type is up to 50 % of the Stokes drift in magnitude, depending on the local wind and wave conditions. The SLDMBs drifters have a drogue extending from 30 to 120 cm depth (also referred to as CODE-type drifters). They follow the ocean current at approximately 1-m depth with negligible wind drag (Davis 1985).

Drifter positions were reported every 30 min by the Iridium satellite system. The drifter velocity $\mathbf{v}^{(d)}$ between two positions $\mathbf{x}_i$ and $\mathbf{x}_{i+1}$ is calculated as

$$\mathbf{v}^{(d)} = \frac{1}{2}(\mathbf{x}_{i+2} + \mathbf{x}_{i+1} - \mathbf{x}_i - \mathbf{x}_{i-1}), \tag{3}$$

which is a weighted average of 30 min average velocity and 90 min average velocity with double weight to the center 30-min period, therefore approximating a noise reduced 1 h average velocity.

3.2 ADCP data

A Nortek Aquadopp ADCP was deployed at the location shown in Fig. 1 (green diamond), collecting data from March 15 to March 31, 2013. The depth of the ADCP below sea level was 8-10 m depending on the tide. The total water depth at this site is 86 m. The relatively high signal frequency of 1 MHz allowed sampling the current in vertical bins of 25 cm.

The instrument was configured in the same way as in a previous experiment (Röhrs et al. 2012), with data being sampled as 2.5 min averages. A Godin-type filter over 60 min in time was applied to achieve similar time filtering as performed by the HF radar. All bins were depth-referenced to the sea surface using the maximum backscatter signal from the surface.

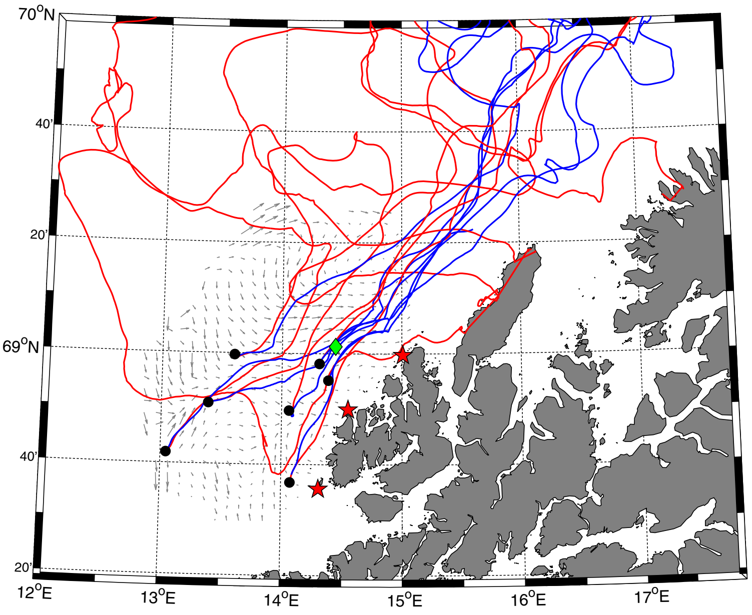

Fig. 1 The experiment site in Vesterålen, Norway. The positions of the three HF radars at Nyksund, Hovden, and Litløy (from north to south) are marked with *red stars*. The location of the ADCP and pressure sensor mooring is marked with a *green diamond*. Trajectories of pairwise deployed iSphere (in *red*) and SLDMB drifters (in *blue*) are drawn as *solid lines*. Typical HF radar coverage (total vectors) is indicated by the *gray arrows*

Previous comparisons with surface drifters (Röhrs et al. 2012), as well as comparisons with the surface drifters in this study show that the Aquadopp ADCP, in the configuration used here, provides reliable surface currents at 0.5-m depth: The ADCP current was verified against instantaneous velocities from surface drifters that passed the ADCP mooring within 8 km distance. ADCP currents between 1 and 7-m depth were also verified against a a 600 kHz Aandera ADCP located at 48-m-depth sampling in 1-m bins, which was deployed on the same mooring line. From 0.5 m up to the surface, we assume that the Eulerian (ADCP) currents are constant.

3.3 HF radar currents

Three SeaSonde HF radars manufactured by Codar Ocean Sensors, USA were deployed during March–May 2013 at the locations shown in Fig. 1. The radars used in this experiment are autonomous, rapidly deployable units that were deployed by helicopter. These allow operation in remote areas with no infrastructure (i.e., roads) and mountainous terrain, and are supposed to be deployable in time-critical situations.

The sensors transmitted radio waves of frequency 13.52 MHz and hence measured the Bragg backscatter from surface waves with 11.1 m wavelength and a wave number of $k_b = 0.566\ \mathrm{m}^{-1}$ to retrieve radial current estimates (hereafter called radials). Linear surface waves at this wavelength travel at a phase speed of 4.16 ms^{-1}. Radials were computed using the "MUSIC" algorithm (Schmidt 1986), which provides current estimates in 5° directional bins and 2 km range bins from 3 km to approximately 90 km distance as hourly averages.

As for this experiment, a rapidly deployable HF radar system was used; the radar direction finding algorithm was not calibrated as is common for permanent installations. The origin of each HF radar measurement may therefore exhibit a bearing offset, which was estimated by finding the HF radar directional bin with maximum correlation to radial ADCP currents, as also done by Emery et al. (2004) and Liu et al. (2014). The analysis revealed that the radar at Nyksund has a bearing offset of 5° at the direction towards the ADCP location, while the radar at Hovden has a 30° bearing offset. For the Litløy radar, the ADCP was too far away to assess the bearing direction offset. For this reason, the analysis in this paper focuses on the radials from the Nyksund radar station (northernmost) and disregards the other two radars.

3.4 Wave data

A pressure sensor was used to obtain one-dimensional wave spectra at the experiment site. To obtain the Stokes drift, two-dimensional spectra are needed, and we use a combination of pressure sensor data with results from a numerical model. To evaluate the performance of the model to predict Stokes drift, we use a waverider buoy that is located near the experiment site.

3.4.1 Waves from pressure sensor

Surface wave data at the experiment site were obtained using a TWR-2050 pressure sensor manufactured by RBR, Canada. The instrument was attached to the ADCP mooring. One-dimensional surface wave variance spectra $E(f)$, where f is frequency, are computed from the pressure time series using the standard transfer function. Hourly significant wave heights H_s from the wave spectra are computed according to

$$H_s^{(obs)} = 4\sqrt{\int_0^\infty E(f)df}. \tag{4}$$

3.4.2 Waves from waverider buoy

A Datawell DWR-MkIII directional waverider buoy moored at 67.56° N, 14.17° E about 160 km south of the experiment site where the total water depth is 220 m. The waverider provided half hourly directional wave spectra $E(f, \theta_w)$, where θ_w is wave direction, in the frequency range of 0.025–0.58 Hz. The Stokes drift at the surface is then computed according to

$$\mathbf{v}_S = 2\int_0^{2\pi}\int_0^\infty E(f,\theta_w)\omega\mathbf{k}df d\theta_w. \tag{5}$$

Here, $\omega = 2\pi f$ is the wave frequency and $\mathbf{k}$ is the wave number vector.

3.4.3 Waves from numerical weather prediction model

Two-dimensional wave spectra at the experiment site were obtained from the limited area wave model of the European Centre for Medium Range Weather Forecasts (hereafter called LAWAM). This model has about 10 km horizontal resolution and provides hourly directional variance spectra $E(f, \theta_w)$. This wave model has recently been proven useful for predicting Stokes drift profiles (Breivik Ø et al. 2014), which is its main purpose in this study. We compute significant wave height H_s from LAWAM as

$$H_s^{(mod)} = 4\sqrt{\int_0^\infty\int_0^{2\pi} E(f,\theta_w)df d\theta_w}. \tag{6}$$

The difference between the observed and modeled wave height are used to calculate a correction factor for the model wave energy spectra. A corrected spectra

$$E'(f,\theta_w) = \left(\frac{H_s^{(obs)}}{H_s^{(mod)}}\right)^2 E(f,\theta_w) \tag{7}$$

is used in the analysis, which essentially means that observed wave heights, but modeled propagation directions, are used. The radial component of the Stokes drift in radar observation direction θ is calculated as

$$v_S(z) = \mathbf{e}_\theta \cdot 2\int_0^{2\pi}\int_0^{\infty} E'\omega\mathbf{k}e^{2|\mathbf{k}|z} df\, d\theta_w, \tag{8}$$

To account for unresolved high-frequency contributions, all spectra (including observed spectra) are appended with a f^{-5} spectral tail (Komen et al. 1994).

We also compute an approximation to the nonlinear correction in the phase velocity of Bragg waves, as seen from a HF radar measuring at 0.38 Hz in direction θ_b (Ardhuin et al. 2009):

$$\begin{aligned}\Delta c_p &= \mathbf{e}_\theta \cdot 2\int_0^{2\pi}\int_0^{0.38Hz} E'\omega\mathbf{k} df\, d\theta_w \\ &+2k_b\int_0^{2\pi}\int_{0.38Hz}^{\infty} E'\omega\cos(\theta_w-\theta) df\, d\theta_w.\end{aligned} \tag{9}$$

3.5 Data synthesis

Radials from the HF radar at Nyksund are linearly interpolated to the ADCP position and to the positions of the surface drifters. For comparison with the ADCP, we corrected the bearing direction of the HF radar by 5°, which was found to be the offset of HF radar directions at the ADCP location. The drifter data are averaged over 1 h. A threshold of 2 km separation and a maximum distance of 40 km to the radar station is chosen to find pairs of drifter speed and HF radar currents. In the analysis, we only consider the radial current speed v, that is, the component of the ADCP and drifter velocities along a line from the HF radar towards the observation point. To indicate the contribution of the radial speed to total speed $\mathbf{v}$, we calculate the ratio

$$r_{rad} = \frac{v}{|\mathbf{v}|} \tag{10}$$

for both ADCP currents and drifter velocities, and the ratio

$$r_{S,rad} = \frac{v_S}{|\mathbf{v}_S|} \tag{11}$$

for the Stokes drift radial component compared to total Stokes drift speed $|\mathbf{v}_s|$ given by LAWAM.

The depth-dependent ADCP current $v'^{(A)}(z)$ was vertically integrated from 0 to 7 m depth with an exponentially decaying weight described by a wavenumber k_a:

$$v^{(A)}(k_a) = 2k_a\int_{-z}^{0} v'^{(A)}(z)e^{2k_a z}dz. \tag{12}$$

This vertical filter imitates the current measured by the HF radar for $k_b = k_a$, i.e., Eq. 2. To test the hypothesis that HF radar currents include the Stokes drift, we compute the Lagrangian current from the ADCP as

$$v_L^{(A)} = v^{(A)} + v_S. \tag{13}$$

To test the hypothesis that the HF radar currents include a contribution from a nonlinear correction to the phase velocity of Bragg waves Eq. 9, we also compute an Eulerian current with nonlinear correction from ADCP currents:

$$v_{nl}^{(A)} = v^{(A)} + \Delta c_p. \tag{14}$$

Radial components of drifter velocities are denoted as $v^{(d)}$. To obtain Eulerian current estimates from the drifters, we subtract the Stokes drift at the surface for the iSphere drifters and the Stokes drift at 1-m depth for the SLDMB drifters:

$$v_E^{(d)} = v^{(d)} - v_S. \tag{15}$$

Finally, for the drifter data, we compute an Eulerian current with the nonlinear correction term estimated from drifter speeds:

$$v_{E,nl}^{(d)} = v^{(d)} - v_S(z) + \Delta c_p. \tag{16}$$

When comparing HF radar radials with ADCP and drifter speeds, we calculate correlation coefficients r, the slope of linear regression lines S, and the root-mean-square differences (RMS) from the bias-reduced HF radar radials. We also give an estimate on the variation for these three statistics within the presented data: each respective dataset has been re-sampled into 1000 new bootstrapped datasets of the same number of samples (Emery and Thomson 1997, ch. 3.19). Standard deviations were then obtained from the statistics (r, S, and RMS) of the re-sampled data.

4 Results

4.1 Wave data

Significant wave heights from the pressure sensor and from the wave model LAWAM at the ADCP station are shown in Fig. 2a. Observed and modeled wave heights agree well in general, but some discrepancies exist during March 11 to 13 and March 16. To account for these discrepancies, wave spectra used in the analysis are corrected according to Eq. 7 using the observed wave heights from the pressure sensor.

Stokes drift speed and direction from the LAWAM model are shown in Fig. 2b, c along with Stokes drift from the

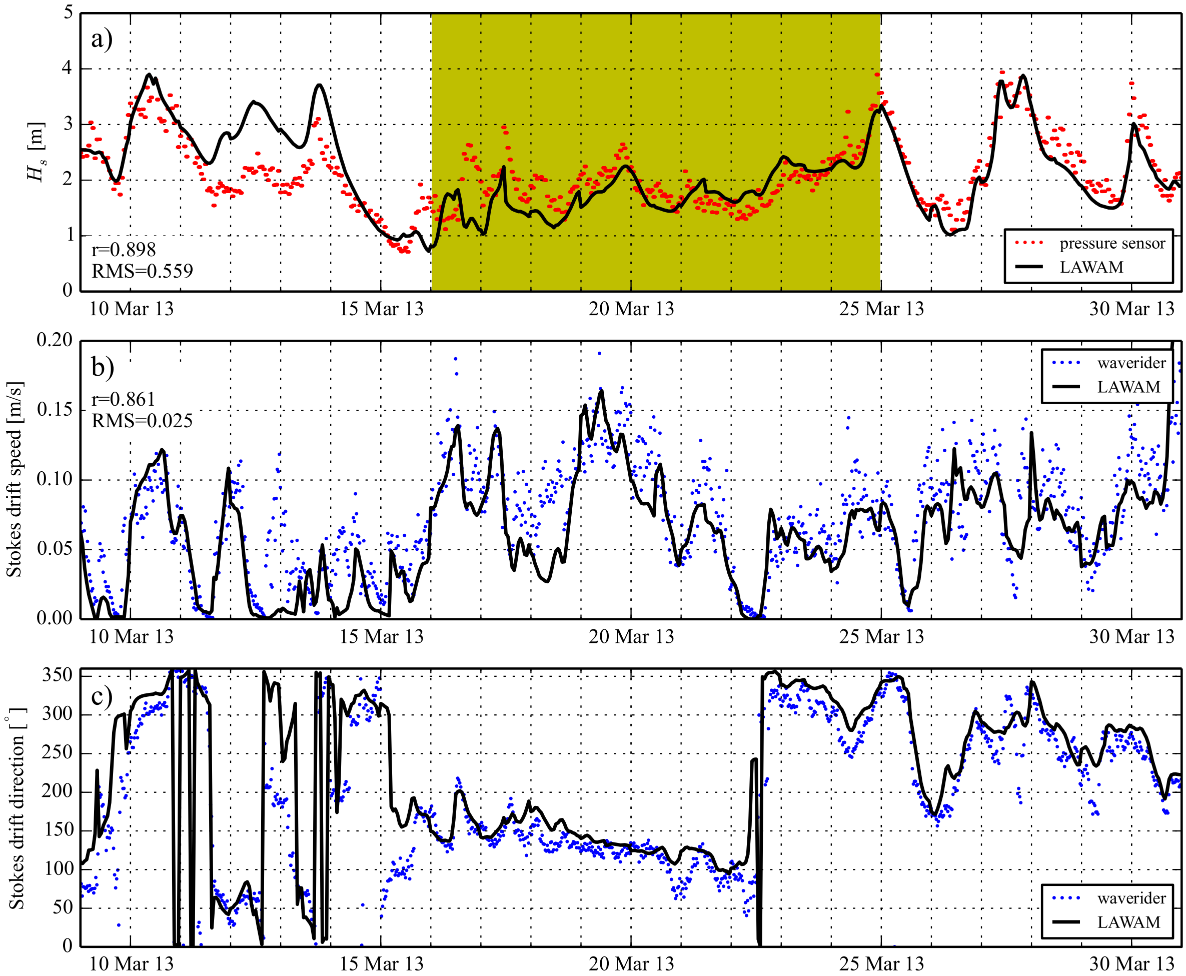

Fig. 2 Comparison of wave model results with observations. **a** Significant wave height from the pressure sensor and from the LAWAM model at the position of the ADCP/pressure sensor rig for the period when ADCP measurements were available. The *yellow shaded area* indicates the period when the drifters are in the range of the HF radar. **b** Stokes drift speed at the surface from the waverider and the LAWAM model at 67.56° N, 14.17° E, which is about 160 km south of the ADCP/pressure sensor rig. **c** Stokes drift direction from the waverider and the LAWAM model for the same position as in panel **b**

waverider. Note that these are not at the same position as the the wave heights in Fig. 2a, but in the same region. To asses the quality of the LAWAM model in our region and time period of interest, correlation coefficients and RMS errors are given for significant wave height and Stokes drift speed in Fig. 2a, b. A vector correlation of Stokes drift components between LAWAM and the waverider is

$$r_v = 1 - \frac{< (v_i - v_j)^2 >}{< v_i^2 > + < v_j^2 >} = 0.903 \qquad (17)$$

where $\mathbf{v}_i$, $\mathbf{v}_j$ are vectors of LAWAM and waverider Stokes drift at the surface, respectively.

Figure 3a shows the Stokes drift at the surface and at one meter depth based on wave spectra from LAWAM, corrected using Eq. 7, at the position of the ADCP/pressure sensor rig. The Stokes drift at 1 m depth is less than half that of the surface Stokes drift. The figure also shows the nonlinear correction to the phase velocity Δc_p and the Stokes drift at the surface in the waves with frequencies below 0.38 Hz. These are comparable in magnitude to the Stokes drift at 1 m depth. Figure 3c displays the ratio (11) of radial to the total Stokes drift magnitude. Only this fraction can have a possible contribution to the HF radar measurements.

4.2 HF radar compared to ADCP

Comparisons of HF radar radials $v^{(HF)}$ with raw and vertically integrated ADCP speeds are shown in Fig. 4, as function of depth for the raw ADCP current $v'^{A}(z)$ and as function of exponential decay scale $z = \frac{1}{2k_a}$ for the integrated $v^{(A)}(k_a)$. For the raw ADCP currents, HF radar currents correlate highest at $z = 1.0$ m depth while the lowest RMS error is at $z = 1.3$ m.

The vertically integrated ADCP current from Eq. 12 agrees best with HF radar currents for decay scales in the range of $0.63\ \mathrm{m}^{-1} > k_a > 0.36\ \mathrm{m}^{-1}$. This mean that the HF radar signal represents a vertical average of currents weighted by an exponential function with an e-folding scale in the range between 0.8 and 1.4 m. Hence, about 80 % of the HF radar signal comes from the upper meter.

Figure 5 shows scatter plots of HF radar currents versus vertically integrated ADCP currents using $k_a = k_b$ in Eq. 12. The pure Eulerian ADCP current $v^{(A)}$ is shown in panel a, while panel b shows a Lagrangian estimate from ADCP currents $v_L^{(A)}$ that include the Stokes drift calculated by Eq. 8. Panel c shows the comparison for a Eulerian ADCP current $v_{nl}^{(A)}$ that includes the nonlinear correction to the phase velocity of Bragg waves. The Eulerian currents (panels a and c) provide a better fit than the Lagrangian current (panel b). In terms of linear regression slope S and spread (RMS), the pure Eulerian current $v^{(A)}$ shows clearly the best agreement with the HF radar. $v^{(A)}$ also yields the highest correlation coefficient with the HF radar, but this difference does not exceed the uncertainty margins. The scatter plots indicate the fraction of the radial ADCP current relative to the absolute ADCP current in color shading, and it appears that outliers are not related to this ratio, implying that the quality of the radial HF radar current does not depend on the orientation of the total current vector.

4.3 HF radar compared to drifters

A comparison between HF radar radials and drifter speeds is given in Fig. 6. Panel a shows a scatter plot for the Lagrangian current $v^{(d)}$, panel b the Eulerian current estimate $v_E^{(d)}$, and panel c shows an Eulerian estimate with nonlinear correction term $v_{E,nl}^{(d)}$. In contrast to the comparison with the ADCP, the in situ measurements now provides Lagrangian velocities and the subtraction of the Stokes drift gives an Eulerian estimate. The Eulerian current $v_E^{(d)}$ compares better with the HF radar than the Lagrangian current $v^{(d)}$, judging from the difference in linear regression slope S and spread (RMS) relative to their uncertainty margins.

The Eulerian current estimate with nonlinear correction $v_{E,nl}^{(d)}$ performs better than $v_E^{(d)}$ in terms of correlation coefficient r and worse in terms of linear regression slope S and spread (RMS). These differences between the Eulerian current with and without nonlinear correction, however, lie within the uncertainty margins for the drifter vs. HF radar comparison.

The outliers in Fig. 6, noticeable by drifter velocities above 0.7 ms^{-1}, are associated with large distances of 30–40 km between the respective drifter and the HF radar. These outliers cause large RMS values, but are not removed from the analysis because not all samples within this distance range are outliers, indicating that the HF radar was often capable of accurately measuring currents up to 40 km away from the radar.

5 Discussion

5.1 Discrepancies between HF radar currents and in situ observations

While the in situ measurements provide currents at certain points or along trajectories, the HF radar provides spatial and temporal averages. Because the instruments measure different currents, we might expect discrepancies that exceed the error margins and noise of the respective instruments. Expected differences between ADCP and HF radar measurements on the West Florida shelf were recently estimated by Liu et al. (2014), finding that 80–100 % of the observed differences could be explained by the horizontal and vertical separation between the measurements.

While it is possible to eliminate the sampling difference due to temporal averaging (it is straightforward to perform time filtering of ADCP or drifter data), the spatial averaging cannot be synchronized. The HF radar processing algorithm estimates the source of each retrieved backscatter signal and averages all data originating from cells of the same radial range and sector bins. Furthermore, the radar provides the standard deviation for the averaged velocity estimate of each cell. For the radar station at Nyksund, the mean of the spatial standard deviations of all cells is $\sigma_s = 0.095\ \mathrm{ms}^{-1}$. This is the spatial variability that is typically lost by averaging over the data in each cell. For each cell, a resulting spatial standard error can be estimated (Everitt B 2003) as

$$e_s = \frac{\sigma_s}{\sqrt{N}}, \tag{18}$$

where N is the number of samples for each respective cell. On average, the HF radar at Nyksund provided $\overline{N} = 3.2$ spatially varying samples, ranging from 1 to 26. A temporal standard error e_t can be estimated in a similar way. Values of spatial and temporal standard errors, averaged over all cells, are given in Table 1.

In addition to the differences in averaging, HF radar and in situ currents differ by the extent to which the Stokes drift may be included, and by the depth that is

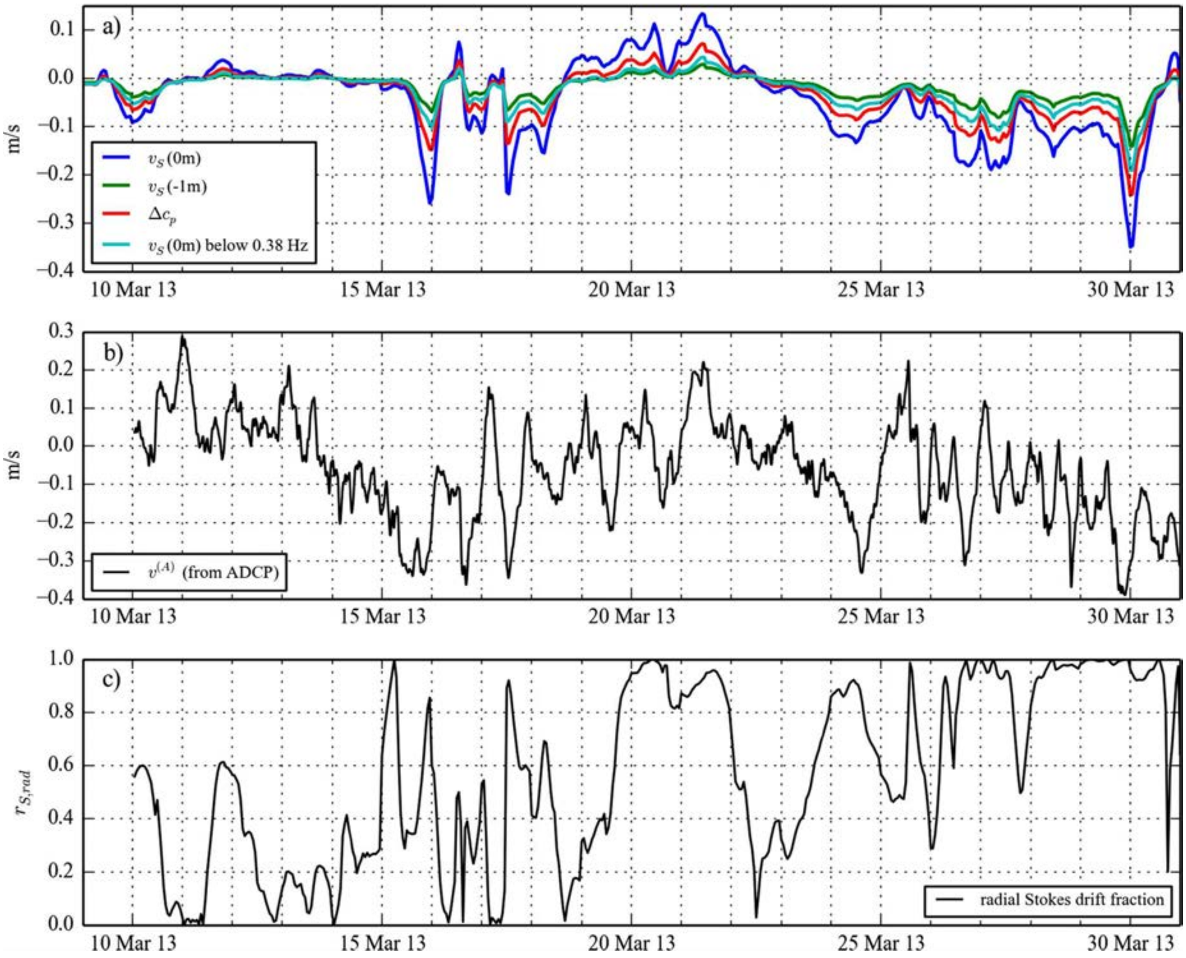

Fig. 3 **a** Stokes drift at the surface (*blue*) and at one meter depth (*green*) calculated from LAWAM wave spectra at the position of the ADCP station. Also shown is the Stokes drift at the surface for wave frequencies below 0.38Hz (*cyan*) and the nonlinear correction to the phase velocity of Bragg waves Δc_p (*red*). **b** The Eulerian current measured by the ADCP. All quantities are radial components, pointing from the Nyksund HF radar station towards the ADCP station. **c** Fraction of the Stokes drift component in radial HF radar direction compared to total Stokes drift speed at the surface

sampled by the different instruments. Despite the differences in spatial averaging and instrument noise, we expect that comparisons between the HF radar and the ADCP or drifters yield a higher degree of agreement if the differences in sampling depth and Stokes drift contribution are correctly accounted for, which is the main question in this analysis.

5.2 Vertical origin of HF radar currents

The ADCP data (Fig. 4) with 25 cm vertical resolution and coverage up to 0.5 m below the surface shows that more than 80 % of the HF radar signal originates from the upper meter. The wave number of the Bragg waves ($k_b = 0.566$ m^{-1}) is within the range of the decay scale estimated from comparison between ADCP and HF radar. Best agreement between HF radar and ADCP was obtained when the ADCP current was vertically integrated according to Eq. 12 with $k_a = k_b$. The theoretical arguments of Stewart and Joy (1974) are thereby confirmed, that is, the radar backscatter signal is exposed to a Doppler shift by the Eulerian current with the same vertical origin as the Stokes drift profile of the Bragg wave.

Teague et al. (2001) compared HF radar currents with ADCP data that was resolved up to 2 m below the surface, employing radars signals with different frequencies. They suggested that the HF radar samples the current at the depth $z = (2k_b)^{-1}$, but did not compare the HF radar currents with vertically integrated ADCP currents. Their ADCP data resolved a depth with minimal RMS error at

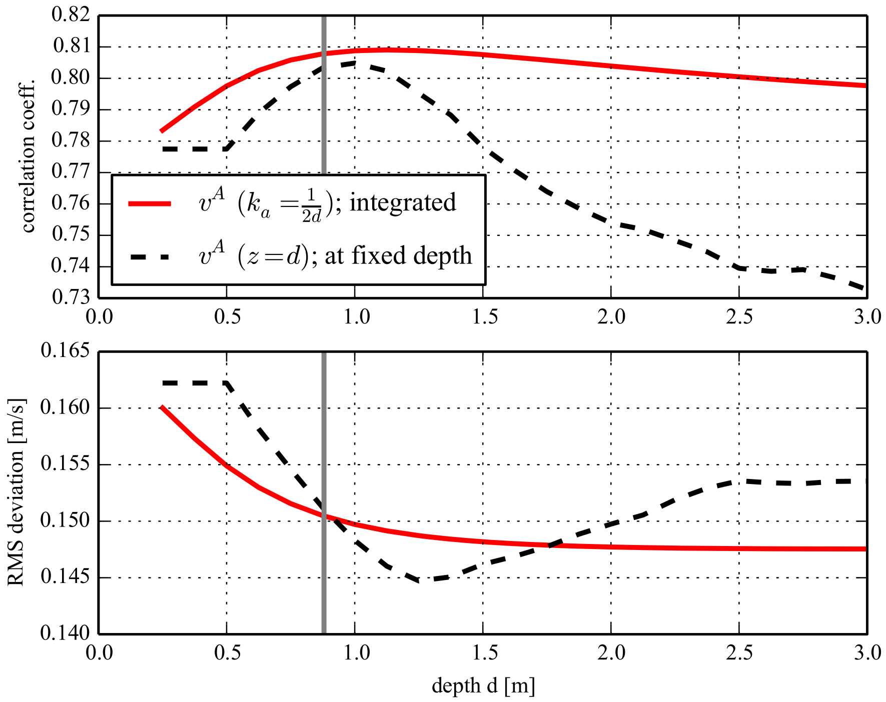

Fig. 4 Correlation and RMS deviation between HF radar and ADCP current as function of depth of ADCP current. The *dashed line* shows statistics for ADCP currents at fixed depth. The *solid line* shows statistics for vertically integrated ADCP current, with integration according to Eq. 2 with $k_a = (2d)^{-1}$. The *gray solid line* indicates the depth $(2k_b)^{-1}$ = 0.88 m according to the wave number of the used Bragg waves

4 m depth for a low frequency radar operating at 4.8 MHz. For a radar frequency of 13.52 MHz, we observe a minimal RMS error at 1.25 m when using ADCP data at fixed depth.

More precisely, the HF radar does not measure the current at $z = (2k_b)^{-1}$ but observes vertically integrated currents, which also gives best agreement between ADCP and the HF radar data presented here. For practical use, however, the vertical origin of HF radar currents is often referred to as an effective depth. Our data supports the practice to use a depth of z = 0.8–1.4 m for radars transmitting at 13.52 MHz.

5.3 Contribution of Stokes drift to HF radar currents

By comparing HF radar currents with in situ measurements of Eulerian and Lagrangian currents, we find that (i) the speeds observed by the ADCP agree better with the HF radar if the Stokes drift is not added to the Eulerian ADCP current, and (ii) the current speeds inferred from drifter trajectories agree better with the HF radar currents if the Stokes drift is subtracted from the (Lagrangian) drifter velocity.

Both comparisons lead to the same conclusion that the HF radar measures the Eulerian and not the Lagrangian current. We know from previous experiments that the iSphere

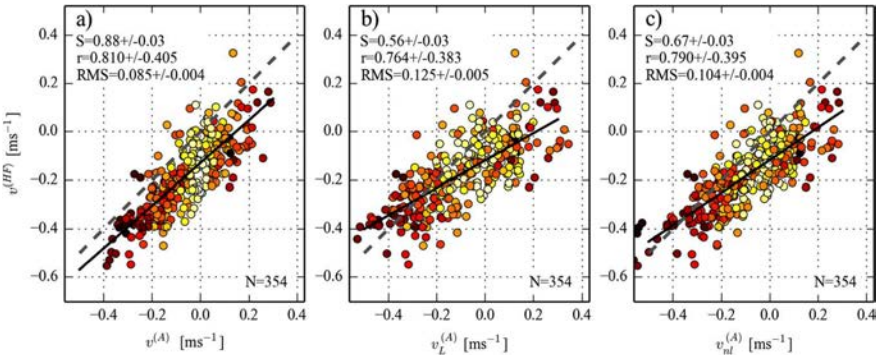

Fig. 5 Scatter plot comparing HF radar currents with ADCP currents. **a** shows the Eulerian ADCP current $v^{(A)}$, **b** shows the Lagrangian current estimate $v_L^{(A)}$ obtained from ADCP and the Stokes drift, and **c** shows the Eulerian current $v_{nl}^{(A)}$ with the nonlinear correction term. The colors of each dot indicate the fraction r_{rad} of radial speed to ADCP total speed (10), with *dark red* for $r_{rad} = 1$ and *bright yellow* for $r_{rad} = 0$

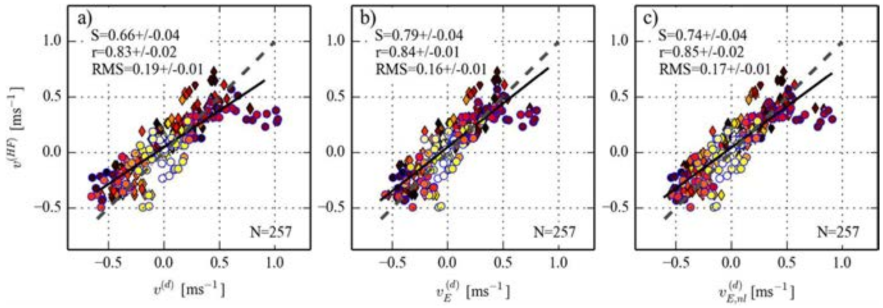

Fig. 6 Scatter plot comparing HF radar currents with drifter speed. *Circles with black edge color* represent iSphere drifters and *diamonds with blue edge color* represent SLDMB speed. **a** Shows the Lagrangian drifter speed v^d, **b** shows the Eulerian current $v_E^{(d)}$ obtained by subtracting the Stokes drift at the respective drifter depth from the drifter speed, and **c** shows the Eulerian current with nonlinear correction term $v_{E,nl}^{(d)}$. The colors of each dot indicate the fraction r_{rad} of radial speed to total drifter speed (10), with *dark red* for $r_{rad} = 1$ and *bright yellow* for $r_{rad} = 0$

Table 1 Magnitudes of the components that form the signal observed by a HF radar transmitting at 13.52 MHz

Phase velocity c_p of linear surface waves	4.16 ms^{-1}
Radial HF radar current $v^{(HF)}$	0.16 ± 1.5 ms^{-1}
Onlinear correction Δc_p	0.03 ± 0.06 ms^{-1}
Spatial error e_s	0.052 ms^{-1}
Temporal error e_t	0.049 ms^{-1}

The values for HF radar current and nonlinear correction averages are derived from the data presented in this study and generally depend on the local current and wave climatology

drifters sample the Lagrangian current, which includes the surface Stokes drift (Röhrs et al. 2012). If the HF radar current is Eulerian, the difference $v^{(HF)} - v^{(d)}$ for the iSphere drifters will be correlated with the Stokes drift. In Fig. 7a, we show the results of such a test: the correlation ($r = -0.721$) is significant within the 99 % level. Figure 7b shows the difference $v^{(HF)} - v^{(d)}$ for the SLDMB drifters, which appears to be independent of Stokes drift. A reasonable explanation is that the SLDMB drifters are following the currents at 1 m depth where the Stokes drift is rather small compared to the surface (compare Fig. 3). Figure 7 also shows (color coded) the ratio $r_{S,rad}$ of the radial Stokes drift component compared to total Stokes drift, as defined in Eq. 11. For the iSphere drifter, there is a clear association of high $r_{S,rad}$ with large deviation between drifter speed and HF radar speed, confirming that the Stokes drift can explain the difference.

A similar comparison for the ADCP current ($v^{(HF)} - v^{(A)}$) is not correlated with the Stokes drift ($r = 0.021$), confirming that both the HF radar and the ADCP measure the Eulerian current. To reason why the HF radar currents do not include the Stokes drift, we recall its measurement

Fig. 7 Comparison between the Stokes drift and the residual current given by the difference between HF current and drifter current for (**a**) the iSphere drifters at the surface and (**b**) the SLDMB drifters at 1 m depth. The radial Stokes drift component for the respective drifter position is color coded with dark red for $r_{S,rad} = 1$ and white for $r_{S,rad} = 0$

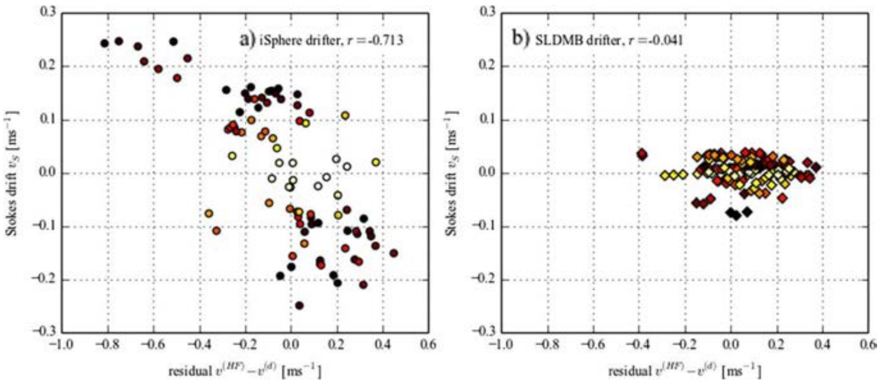

principle: The radar observes the phase speed of surface gravity waves, which is modified by the Doppler shift due to an Eulerian current. The Stokes drift is not a part of the Eulerian current that causes the Doppler shift, and neither should it significantly modify the intrinsic phase velocity of the Bragg waves.

A contribution from nonlinear dispersion (9) appears to be about half of the Stokes drift in magnitude (see Fig. 3). It contains the Stokes drift of waves longer than the Bragg waves (Fig. 3, cyan line) and an additional contribution from shorter waves. A comparison of HF radar currents with Eulerian current estimates with and without the nonlinear correction term (9) from ADCP and surface drifters (Figs. 5 and 6) shows that pure Eulerian estimates yield better agreement. However, the difference is small because the nonlinear correction term itself is small.

Recalling typical magnitudes of the quantities that form the signal measured by the HF radar (Table 1), we conclude that the contribution from the nonlinear phase velocity correction term is smaller than the observation uncertainties of the HF radar currents. This correction term was presented through a series of papers (Broche et al. 1983; Ardhuin et al. 2009) that are based on the analysis of Barrick and Weber (1977), which Creamer et al. (1989) and Janssen (2009) have argued is incorrect, as outlined in Section 2.1. The uncertainty margins of the comparison statistics do not allow for a conclusion on the contribution of this second-order quantity.

6 Conclusions

The presented data allow us to conclude that the HF radar essentially measures the Eulerian current and not the Lagrangian current that includes the Stokes drift. The possible contribution from a nonlinear correction to the phase velocity of the Bragg waves is not significant compared to the uncertainties in the current estimates. The SLDMB drifters in the design of Davis (1985), which follow the current at 1 m depth, are found to be the most suitable in situ platforms for validating HF radar currents because they represent a similar vertical average of ocean currents, and the advection by the Stokes drift for this kind of drifters is small for the wind and wave conditions typical of the area considered in this study.

Acknowledgments This work was funded by the Norwegian Clean Seas Association For Operating Companies (NOFO) and ENI Norge A/S, with contributions from the Research Council of Norway (196438/BIOWAVE and 207541/OILWAVE). The contribution by Ø.B. was carried out as part of the European Union FP7 project MyWave (grant no 284455). The authors would like to thank Svein Sundby and Frode Vikebø (IMR) for helpful discussions and kind assistance during the planning phase, and Erik Berg (IMR), as well as the captain and crew of R/V Johan Hjort, for their kind assistance with the drifter deployments. We would also like to thank Ronald Pedersen (IMR), Tor Gammelsrød (UiB), Erik Kvaleberg, and Anne Hesby (Royal Norwegian Navy) for loan of instruments and assistance with the ADCP rig. Assistance from the captains and crews of the NSO Crusader and R/V Håkon Mosby when deploying and recovering the ADCP rig is also gratefully acknowledged.

References

Ardhuin F, Marie L, Rascle N, Forget P, Roland A (2009) Observation and estimation of lagrangian, stokes, and eulerian currents induced by wind and waves at the sea surface. J Phys Oceanogr 39(11):2820–2838. doi:10.1175/2009JPO4169.1

Barrick DE, Weber BL (1977) On the nonlinear theory for gravity waves on the ocean's surface. part ii: Interpretation and applications. J Phys Oceanogr 7(1):11–21

Breivik O, Allen A, Maisondieu C, Olagnon M (2013) Advances in Search and Rescue at Sea. Ocean Dynam 63:83–88. doi:10.1007/s10236-012-0581-1

Breivik Ø, Janssen PEAM, Bidlot JR (2014) Approximate stokes drift profiles in deep water. J Phys Oceanogr 44:2433–2445. doi:10.1175/JPO-D-14-0020.1

Broche P, de Maistre JC, Forget P (1983) Mesure par radar dcamtrique cohrent des courants superficiels engendrs par le vent. Oceanol Acta 6:43–53

Chapman RD, Graber HC (1997) Validation of hf radar measurements. Oceanography 10:76–79. doi:10.5670/oceanog.1997.28

Creamer DB, Henyey F, J Wright RS (1989) Improved linear representation of ocean surface waves. J Fluid Mech 205:135–161. doi:10.1017/S0022112089001977

Davis RE (1985) Drifter observations of coastal surface currents during CODE: The method and descriptive view. J Geophys Res 90(C3):4741–4755. doi:10.1029/JC090iC03p04741

Emery BM, Washburn L, Harlan JA (2004) Evaluating radial current measurements from codar high-frequency radars with moored current meters. J Atmos Ocean Tech 21(8): 1259–1271

Emery W, Thomson RE (1997) Data Analysis Methods in Physical Oceanography. Elsevier, Amsterdam

Everitt B (2003) The Cambridge Dictionary of Statistics. Cambridge Univ Press

Graber HC, Haus BK, Chapman RD, Shay LK (1997) HF radar comparisons with moored estimates of current speed and direction: Expected differences and implications. J Geophys Res 102 C8:18 766:749–18. doi:10.1029/97JC01190

Janssen P (2009) On some consequences of the canonical transformation in the Hamiltonian theory of water waves. J Fluid Mech 637(1):1–44. doi:10.1017/S0022112009008131

Komen GJ, Cavaleri L, Doneland M, Hasselmann K, Hasselmann S, Janssen PAE (1994) Dynamics and modelling of ocean waves

Law K (2001) Measurements of near surface ocean currents using hf radar. PhD thesis, University of California Santa Cruz

Liu Y, Weisberg RH, Merz CR (2014) Assessment of codar seasonde and wera hf radars in mapping surface currents on the west florida shelf. J Atmos Ocean Tech 31:1363–1382. doi:10.1175/JTECH-D-13-00107.1

Ohlmann C, White P, Washburn L, Terrill E, Emery B, Otero M (2007) Interpretation of coastal hf radar-derived surface currents with high-resolution drifter data. J Atmos Ocean Tech 24:666–680. doi:10.1175/JTECH1998.1

Paduan JD, Washburn L (2013) High-frequency radar observations of ocean surface currents. Annu RevMarine Sci 5:115–136. doi:10.1146/annurev-marine-121211-172315

Röhrs J, Christensen KH, Hole LR, Broström G, Drivdal M, Sundby S (2012) Observation-based evaluation of surface wave effects on currents and trajectory forecasts. Ocean Dynam 62:1519–1533. doi:10.1007/s10236-012-0576-y

Schmidt (1986) Multiple emitter location and signal parameter estimation. IEEE T Antenn Propag 34-3:276–280. doi:10.1109/TAP.1986.1143830

Sperrevik AK, Christensen KH, Röhrs J (2015) Constraining energetic slope currents through assimilation of high-frequency radar observations. Ocean Sci 11:237–249. doi:10.5194/os-11-237-2015

Stewart RH, Joy JW (1974) HF radio measurements of surface currents. Deep Sea Res 21:1039–1049. doi:10.1016/0011-7471(74)90066-7

Stokes GG (1847) On the theory of oscillatory waves. Trans Cambridge Philos Soc 8:441–473

Teague C, Vesecky J, Hallock Z (2001) A comparison of multifrequency hf radar and adcp measurements of near-surface currents during cope-3. IEEE J Ocean Eng 26(3):399–405. doi:10.1109/48.946513

Zhang WG, Wilkin JL, Arango HG (2010) Towards an integrated observation and modeling system in the New York Bight using variational methods. Part I: 4DVAR data assimilation. Ocean Model 35:119–133. doi:10.1016/j.ocemod.2010.08.003

Paper II

5.2 Constraining energetic slope currents through assimilation of high-frequency radar observations

Ann Kristin Sperrevik, Kai Håkon Christensen, and Johannes Röhrs
Ocean Science **11**, 237-249 (2015)

Ocean Sci., 11, 237–249, 2015
www.ocean-sci.net/11/237/2015/
doi:10.5194/os-11-237-2015

Ocean Science
Open Access

Constraining energetic slope currents through assimilation of high-frequency radar observations

A. K. Sperrevik, K. H. Christensen, and J. Röhrs
Norwegian Meteorological Institute, Oslo, Norway

Correspondence to: A. K. Sperrevik (ann.k.sperrevik@met.no)

Received: 11 April 2014 – Published in Ocean Sci. Discuss.: 4 June 2014
Revised: 6 February 2015 – Accepted: 14 February 2015 – Published: 11 March 2015

Abstract. Assimilation of high-frequency (HF) radar current observations and CTD hydrography is performed with the 4D-Var analysis scheme implemented in the Regional Ocean Modeling System (ROMS). We consider both an idealized case, with a baroclinic slope current in a periodic channel, and a realistic case for the coast of Vesterålen in northern Norway. In the realistic case, the results of the data assimilation are compared with independent data from acoustic profilers and surface drifters. Best results are obtained when background error correlation scales are small (10 km or less) and when the data assimilation window is short, i.e. about 1 day. Furthermore, we find that the impact of assimilating HF radar currents is generally larger than the impact of CTD hydrography. However, combining the HF radar currents with a few hydrographic profiles gives significantly better results, which demonstrates the importance of complementing surface observations with observations of the vertical structure of the ocean.

1 Introduction

Skillful ocean forecasts are of key importance for many operations at sea, especially for emergency response services such as search-and-rescue and oil spill mitigation. In particular, near-surface currents are an important input to operational drift forecast models. However, the predictability of ocean currents remains a challenge due to their turbulent nature and high spatial variability, for example, associated with eddies.

Observations of the ocean surface temperature (Wentz et al., 2000; Rayner et al., 2003) and elevation (Fu et al., 1994) from satellites have become plentiful during the last decades. New satellite observations include surface salinity and currents, but the uncertainty of these products still remains too high for use in models with high horizontal resolution, i.e. on the order of 1 km. Through efforts such as the International Argo Program (Roemmich et al., 2009), observations of the subsurface ocean are increasing in number, but still remain too few to resolve the vertical and horizontal density structure of, e.g. oceanic fronts.

Advanced data assimilation (DA) techniques developed in the field of numerical weather prediction are now used to a great extent within ocean modelling. The DA schemes range from multivariate implementations of optimal interpolation, such as Ensemble Optimal Interpolation (Oke et al., 2010) in the BLUElink forecast system (Brassington et al., 2007), to ensemble Kalman filters (EnKF) (Evensen, 2003) in the TOPAZ 4 system (Sakov et al., 2012) and variational methods (Dimet and Talagrand, 1986; Courtier et al., 1994) used in UK Met Office's FOAM (Blockley et al., 2014). Kalnay et al. (2007) and Gustafsson (2007) provide an interesting discussion on the advantages of both EnKF and the time-dependent variational method, 4D-Var. The latter approach is applied in this study. In 4D-Var, the aim is to minimize a cost function, which takes both misfits between model and background state and between model and observations into account. One of the main benefits of 4D-Var lies in the fact that observations are evaluated at the correct time.

Common for these forecast systems is that few, if any, current observations are assimilated, mainly owing to a lack of observations. HF (high-frequency) radars, which can sample surface currents up to 200 km offshore, provide an excellent option for mapping surface currents in coastal areas (e.g. Paduan and Washburn, 2013; Barrick et al., 1977; Chapman et al., 1997; Gurgel et al., 1999). Real-time surface cur-

Published by Copernicus Publications on behalf of the European Geosciences Union.

rents from HF radars can be used for monitoring and emergency applications, but also for data assimilation to improve the ocean forecasts. Previous studies (see Breivik and Saetra, 2001; Oke et al., 2002; Paduan and Shulman, 2004; Barth et al., 2008; Zhang et al., 2010, for some examples) demonstrate the potential of HF radar current observations in ocean data assimilation systems. The aim of this study is to investigate whether assimilation of current observations from a rapidly deployable HF radar system (Kjelaas and Whelan, 2011) in a high-resolution ocean model is a feasible way to improve the regional ocean forecast during, e.g. an oil spill event.

Assimilation of HF radar currents requires an ocean forecast system which is ready to use such observations as soon as they become available. The Regional Ocean Modeling System (ROMS; http://www.myroms.org), for which a sophisticated 4D-Var assimilation system, described in detail in Moore et al. (2011a, b, c), has been developed, is implemented for a region in northern Norway. The circulation pattern in this area is dominated by two northward flowing currents, the North Atlantic Current which flows along the shelf slope, and the Norwegian Coastal Current. Typical current speeds are on the order of 0.2–0.5 $\mathrm{m\,s^{-1}}$. The properties of the water masses associated with these currents are in strong contrast to one another, as the coastal current strongly depends on freshwater from the Baltic Sea and the Norwegian fjords. During winter the coastal water is also noticeably colder than the saltier and warmer water masses of Atlantic origin further offshore. The region just west of Vesterålen, where the continental shelf narrows considerably, is characterized by high eddy kinetic energy levels (Isachsen et al., 2012), which makes this a challenging area for ocean predictions. Additionally, there is a strong tidal signal in the area (Moe et al., 2002), with tidal ranges of 2–3 m. Initial tests using an idealized model were made before the tests with a realistic model configuration. These tests were motivated by the wish to investigate more in detail the possible impact of HF radar observations in constraining unstable, highly energetic and narrow currents on steep slopes, such as we find offshore of Vesterålen. These idealized experiments were carried out prior to the field experiment and provided useful information about the expected impact of assimilating real observations, as well as starting points for tuning the data assimilation system with regard to values of e.g. assimilation window length and horizontal error correlation length scales.

We use the incremental, strong-constraint (perfect model assumption) IS4DVAR driver of ROMS, in which the cost function is minimized iteratively by applying a conjugate gradient algorithm, so-called inner loops. Outer loops allow for relinearization of the full model trajectory where the intermediate estimates of the cost function are taken into account, and is a way to account for nonlinearities not represented in the tangent linear and adjoint models. ROMS IS4DVAR is well documented in a series of studies, such as Powell et al. (2008), Broquet et al. (2009), Zhang et al. (2010) and Zavala-Garay et al. (2012). As a consequence of the perfect model assumption, the analyses produced by IS4DVAR corresponds to a trajectory of the forecast model. Thus, this approach is not capable of correcting discrepancies caused by flaws in the numerical model itself. We show that the skill of the predictions produced by the ocean forecast system indeed increases after just one assimilation cycle when HF radar total currents are included. Including in situ temperature and salinity profiles to the assimilated observational data set adds an additional constraint on the circulation.

We start by describing the observational data sets in Sect. 2. In Sect. 3 we present an idealized assimilation experiment, before a realistic experiment is presented and compared with independent observations in Sect. 4. A summary and some concluding remarks are given in Sect. 5.

2 Field campaign and observation network

An array of three SeaSonde HF radars, manufactured by CODAR Ocean Sensors, was deployed along the coast of Vesterålen in northern Norway in the first week of March 2013. All three stations were demobilized in the beginning of June 2013. The operating frequency of the radars was 13.525 MHz, thus, measuring the Bragg backscatter from waves with wavelength of about 11 m. Paduan et al. (2006) provide an excellent analysis of sources of errors in the raw radial currents. When the radials are combined to form gridded fields of total current vectors, an additional error, geometrical dilution of precision (GDOP) (Chapman et al., 1997), is introduced. Each observation data file transmitted by the HF radar system contained estimates of the observation errors, which are a combination of signal to noise rations, velocity variances within range cells, and GDOP for two or more systems. Typically, these errors were less than 20 % of the observed values within a distance of about 40 km of the radars, gradually increasing to almost 100 % near the limits of their range. The average relative error is found to be similar to what would be expected if the errors were mainly due to GDOP. As the currents observed by HF radars include tidal currents, the observations are usually subjected to a correction of the tidal signal before assimilation to account for discrepancies in observed and modelled tides, as described in Zhang et al. (2010). However, as our time series is too short to provide a good estimate of the observed tidal signal, no corrections of this kind have been made. This would, however, also be the case during a realistic event, and our results are thus a demonstration of the potential impact of a rapidly deployable HF radar system.

The main motivation for deploying the radars in this part of Norway was the co-location with the annual cod stock assessment cruise of the Institute of Marine Research (IMR) (see Fig. 1), during which hydrographic and acoustic data are routinely collected. During the 10-day long 2013 cruise,

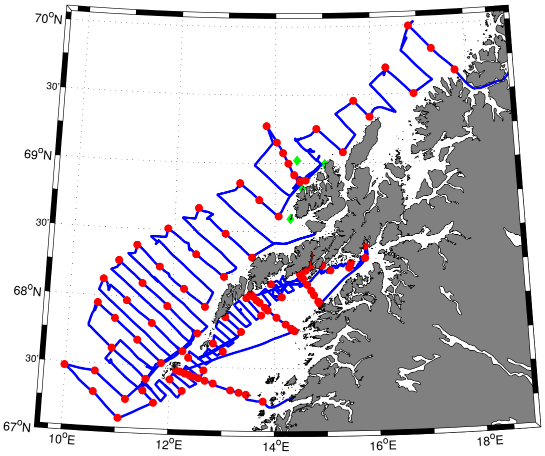

Figure 1. The ship track of R/V *Johan Hjort* during the cod stock assessment cruise in March 2013. The cruise started in Tromsø (north-east in map) and ended in Bodø (bottom middle in map). The red dots indicate stations where CTD profiles where taken. The positions of the three HF radars and the ADCP rig are shown as green diamonds.

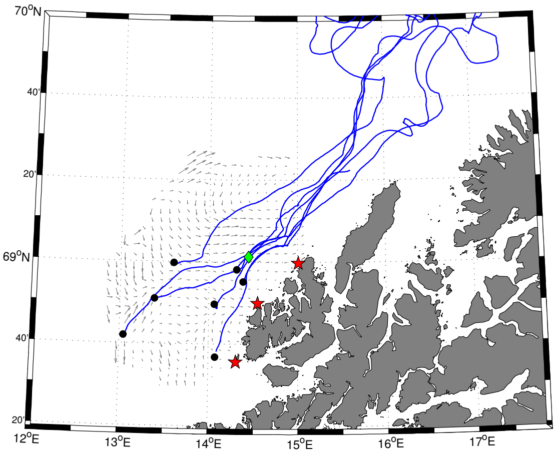

Figure 2. Positions of the HF radar stations, drifter trajectories, and ADCP rig. Starting from the south the HF radar stations were at Litløy, Hovden and Nyksund. The grey arrows are total vector currents from the HF radar system, indicative of the coverage when all three stations were operational. The blue lines indicate the iSLDMB trajectories. The position of the ADCP rig is marked by a green diamond.

a total of 96 CTD profiles were collected (CTD stations are shown in Fig. 1). Cross-shelf sections allow for sampling of water masses of different characteristics. The near-surface observations vary from 2 °C and a salinity of 33 inside the archipelago to 6 °C and a salinity of 35 at the furthest point offshore.

Seven surface drifters from MetOcean, Canada, were deployed from the research vessel (R/V) *Johan Hjort* as it passed the area covered by the HF radars (see Fig. 2). These were iSLDMB (iridium Self Locating Datum Marker Buoy) drifters, which have a drogue centred at 65 cm below the surface. The precision of the GPS positions are approximately 10 m, implying an error circle with a radius of 10 m. The analysis in Sect. 4.3 focuses on 3 h long trajectory segments during which the buoys travelled an average of ~ 2700 m. The errors are thus typically less than 1 % of the observed distance.

Prior to the cod stock assessment cruise we deployed a mooring with three separate acoustic Doppler current profilers (ADCPs). The total water depth at the site was 86 m, its location is shown in Fig. 2. Two Anderaa ADCPs of 600 kHz were mounted at a depth of about 40 m, one upward looking and one downward looking, in addition to an upward looking 1 MHz Nortek Aquadopp Profiler at about 10 m depth. The observed ocean currents at 1 m depth from the Nortek Aquadopp ADCP had a variability (standard deviation) of 17 cm s^{-1}. The accuracy is 2 cm s^{-1} for 30 min averaged samples. This accuracy is obtained as the mean error of the 30 min averages, given by the standard deviation of bootstrapped samples in each averaging period. The field campaign is described in more detail in Röhrs et al. (2015) and Christensen et al. (2013).

3 Idealized experiments

Prior to applying the assimilation system to a realistic case we investigate various options associated with the IS4DVAR scheme using an idealized setup. More specifically, the IS4DVAR scheme is tested for an idealized case of strongly nonlinear, unstable baroclinic flow along a steep slope. The impact of varying the horizontal error correlation scales, which are isotropic, the number of inner and outer loops, as well as the length of the assimilation window is assessed to provide an indication on how to configure the assimilation system for the realistic case later on. The tests are set up such that the model system is essentially without any systematic error and the evaluation of the test cases is primarily based on the standard deviation of the analysis error. The main motivation of these experiments is to test the applicability of IS4DVAR for such energetic and nonlinear flow as we find in our study area. Focus is therefore on the ability of IS4DVAR to reproduce the observed flow features; hence, we have not added any errors to the synthetic observations. We use a linear equation of state, and density changes are accommodated by imposing surface and bottom heat fluxes; hence, in contrast to the realistic experiments described later on, salinity plays no role here.

There are seven prognostic variables in ROMS $(u, v, T, S, \zeta, \bar{u}, \bar{v})$ representing horizontal velocity in easterly direction, horizontal velocity in northerly direction, potential temperature, salinity, vertically averaged velocity in easterly direction, vertically averaged velocity in northerly direction, and sea surface height, respectively.

3.1 Model grid

The model domain is configured as a channel with periodic north–south boundary conditions and solid walls along the eastern and western boundaries. The grid is Cartesian with a horizontal resolution of 2.4 km. We use the f plane approximation with a constant Coriolis parameter equivalent to 65° N. The domain size is 100×120 interior grid points (easterly/northerly directions), and we use 35 vertical levels.

The main topographic features are (i) a shelf along the eastern boundary, with average depth of 200 m, and width of approximately 70 km, (ii) a sharp shelf break with a hyperbolic tangent profile (maximum slope is approximately 0.1), and (iii) a deep ocean floor with average depth of approximately 1800 m towards the western boundary. In order to trigger instabilities, the depth is perturbed with random values between ±50 m.

3.2 Initialization and forcing of the model

The initial conditions are uniform with $T = 10\,°\mathrm{C}$, $S = 35$, $\zeta = 0\,\mathrm{m}$ and zero velocities. Constant heat fluxes over a period of 150 days are applied. The aim is to produce unstable baroclinic currents that will be guided by topography. To accommodate this, we apply a net bottom heat flux into the ocean on the shelf and a net surface heat flux out of the ocean over the deep ocean (Isachsen, 2011). These fluxes are exactly balanced, such that the net heat flux into the ocean is zero. Since the deep ocean is wider than the shelf, the surface fluxes are smaller than the bottom fluxes (approximately 160 and 440 $\mathrm{W\,m^{-2}}$, respectively). The momentum and net freshwater fluxes are zero.

The water heated over the shelf bottom is rapidly mixed upwards through the entire water column resulting in a sharp temperature front near the shelf break. Due to geostrophic adjustment, a northward flowing, topographically controlled slope current develops. This current is baroclinically unstable and heat exchange with the deep water region is facilitated by macro turbulence (ocean eddies), see Fig. 3.

The domain is periodic so that the water masses flowing out of the domain at the northern boundary reappear at the southern boundary. As shown in Fig. 3, the mean northward surface velocity has a maximum of about 1 $\mathrm{m\,s^{-1}}$ over the slope, which means that a drifting object can potentially be advected through the domain in about 3 days. The flow is also characterized by baroclinic and barotropic waves and eddies with propagation speeds that are generally different from the mean flow speeds. To investigate how upstream conditions influence the dynamics in this region, we performed an adjoint sensitivity study (e.g. Moore et al., 2009; Zhang et al., 2009), focusing on the advection of water masses, hence, investigating the sensitivity of the surface velocity variance to temperature in a short section over the slope in the middle of the domain. Based on our results we conclude that an upper limit of 3 days for the assimilation experiments is adequate.

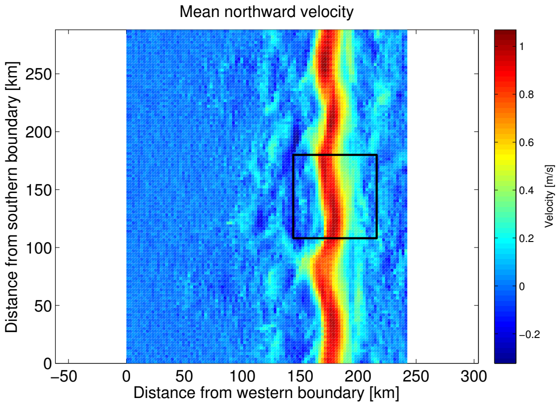

Figure 3. The mean northward surface velocity during a 3-day simulation. The region enclosed by the black line is used for assessing the performance of the data assimilation system.

3.3 Configuration of the data assimilation system

In our experiments, data assimilation is only considered for interior grid points and no adjustment of the surface/bottom fluxes or boundary conditions are made. The 4D-Var schemes implemented in ROMS also has options for multivariate background error correlations, which is based on the assumption of geostrophic balances and the baroclinic contribution to sea surface height as described in Moore et al. (2011c). In our case, the Rossby radius is small and the flow is highly unstable and energetic, implying considerable ageostrophic forcing. In addition, the main current is close to the coast and runs along very steep bathymetry; hence, we do not make use of any such options here. Correlation between state variables are, however, implicitly accounted for by the model physics. The estimates of background errors are taken from day 120 to 150 of the spin-up period, using the standard deviation of each variable in each grid point. The vertical error correlation lengths for all variables is set to 30 m. Horizontal length scales are isotropic and the same for all variables in the entire model domain (Moore et al., 2011c).

3.4 Synthetic observations

Synthetic observations are taken from a separate model simulation that has been forced with time-varying momentum and heat fluxes. An example of the difference between the simulation used for synthetic observations and the simulation that forms the basis for the assimilation experiments is shown in

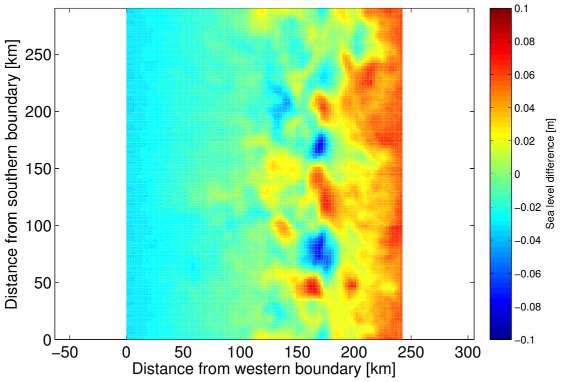

Figure 4. The difference between the restart fields used for the assimilation experiments and for obtaining synthetic observations, here showing sea surface height.

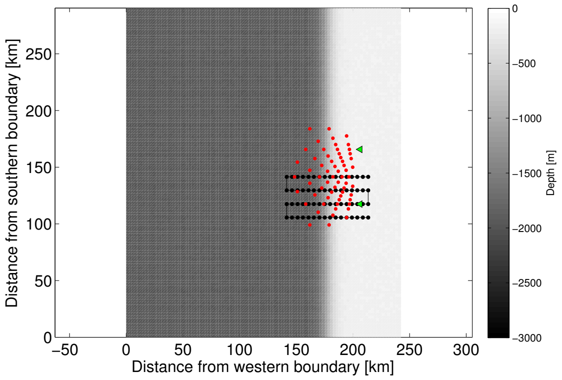

Figure 5. The black dots show where temperature profiles are taken. One full vertical profile is taken every hour and four sections are made, starting from the north. The red dots are the intersection points of the two simulated HF radars (which are marked as green triangles). Hourly observations of total current vectors are produced for the assimilation. The water depth is indicated in grey and ranges from 200 m on the shelf (light grey) and 1800 m in the deep part (dark grey).

Fig. 4. The difference between the simulations is primarily related to small-scale features associated with the baroclinically unstable current over the slope. An estimate of realistic observation errors is assigned to the synthetic observations for use in the assimilation system, but no random or systematic errors are added to the observation values themselves.

The observation locations are shown in Fig. 5. Hydrographic observations, e.g. such as those taken from a research vessel with a CTD, are simulated by taking a single vertical profile of temperature every hour, zigzagging southwards with four sections across the slope. A total of 64 temperature profiles are processed and each individual observation is assigned a constant error of 0.05 K. Two simulated HF radars are used to provide hourly total current vectors in 61 locations. These HF radar stations are positioned a distance of $y_a = 118$ km and $y_b = 166$ km from the southern boundary. The idealized observations are taken at positions where the beams from the two simulated HF radars intersect.

We assume that the HF radars retrieve radial currents from an effective depth, $D_\mathrm{e} = 2$ m, with an azimuthal resolution of $\Delta\theta = 11.25°$. Furthermore, we assume that the maximum range of the radars is $R = 80$ km, and that the relative observation error σ_R associated with the radial currents is a linear function of radial distance r. The azimuthal resolution determines the number of beam directions and, combined with the maximum range R, also the number of intersecting beams from which we can estimate total current vectors.

To obtain the synthetic HF radar observation errors we have first used standard vector algebra to determine the positions were the beams intersect and then calculated the errors in the easterly and northerly directions ($\sigma_{\mathrm{GDOP}}^{(\mathrm{E})}, \sigma_{\mathrm{GDOP}}^{(\mathrm{N})}$) due to geometric dilution of precision (GDOP) (Chapman et al., 1997). The total errors are then assumed given by

$$(\sigma_{\mathrm{tot}}^{(\mathrm{E})}, \sigma_{\mathrm{tot}}^{(\mathrm{N})}) = \left(\sigma_{\mathrm{GDOP}}^{(\mathrm{E})} \sigma_R u, \sigma_{\mathrm{GDOP}}^{(\mathrm{N})} \sigma_R v\right), \qquad (1)$$

where (u, v) are the observed speeds in the easterly and northerly directions, respectively. The errors in a real HF radar system are more complex than those given by Eq. (1), but a comparison with error statistics from a CODAR SeaSonde system deployed near Fedje in western Norway indicate that the values obtained from Eq. (1) are reasonable (not shown here).

Finally, in order to cover the region with the most energetic currents near the slope, the entire simulated HF radar system is translated approximately 40 km westwards from the eastern boundary, see Fig. 5.

3.5 Results of the idealized experiments

We only consider the velocities (u, v) and the temperature T in the evaluation of the idealized experiments. Furthermore, we only consider a limited region of interest similar to the HF radar coverage area (see Fig. 3) and also restrict the evaluation to the two uppermost vertical levels of the model. We evaluate a 3-day period using sequential data assimilation when the assimilation window is shorter than 72 h.

The procedure is as follows: each model simulation results in an analysis, i.e. a solution of IS4DVAR, which is compared with the "truth" as represented by the simulation that provides the synthetic observations. Average bias and standard deviation for each of the variables (u, v, T) are calculated based on all grid points and all output times in the region of interest. Due to the idealized design of the experiments, the (u, v, T) variables have little bias compared to what we would expect from a realistic model. The standard deviation is used when deciding which options yield the best results.

Table 1. Standard deviation (SD) of analysis error in idealized experiments: comparison between different error correlation scales.

	SD(u) in m s^{-1}	SD(v) in m s^{-1}	SD(T) in K
None	0.183	0.223	0.511
5 km	0.168	0.209	0.437
10 km	0.174	0.216	0.447
20 km	0.180	0.223	0.452

Table 2. Standard deviation of analysis error in idealized experiments: comparison between different observation data sets.

	SD(u) in m s^{-1}	SD(v) in m s^{-1}	SD(T) in K
No assimilation	0.183	0.223	0.511
HF only	0.150	0.188	0.442
CTD only	0.183	0.223	0.471
Both HF and CTD	0.168	0.209	0.437

A total of 15 different model simulations with IS4DVAR have been made. In the simulations we have considered (i) the horizontal background error correlation scales, (ii) relinearization of tangent linear and adjoint models using outer loops, (iii) length of assimilation window, and (iv) the relative impact of HF radar observations compared to hydrographic observations.

The results show that using a small horizontal error correlation scale of 5 km gives best results (see Table 1); a likely explanation is that observation values are erroneously distributed across sharp gradients when larger correlation scales are used. Furthermore, using outer loops is beneficial, with no significant improvement when using more than two relinearizations. The length of the assimilation window also plays a role: slight improvement is obtained when reducing the window length from 72 to 24 h, but there is essentially no difference when the window length is further reduced to 6 h. The impact of assimilating HF radar currents is generally larger than the impact of assimilating hydrography, but in both cases we obtain improvement for the temperature. Assimilating only hydrography profiles does not improve the currents, while assimilating HF radar currents has a positive impact on both the velocities and the temperature (see Table 2).

4 Realistic experiments

The realistic experiments were carried out with a model application covering the region of the Lofoten and Vesterålen archipelago with 2.4 km horizontal resolution (see Fig. 6). The bathymetry of the domain resembles that of the idealized application, with a shelf in the eastern part of the domain and a steep shelf break.

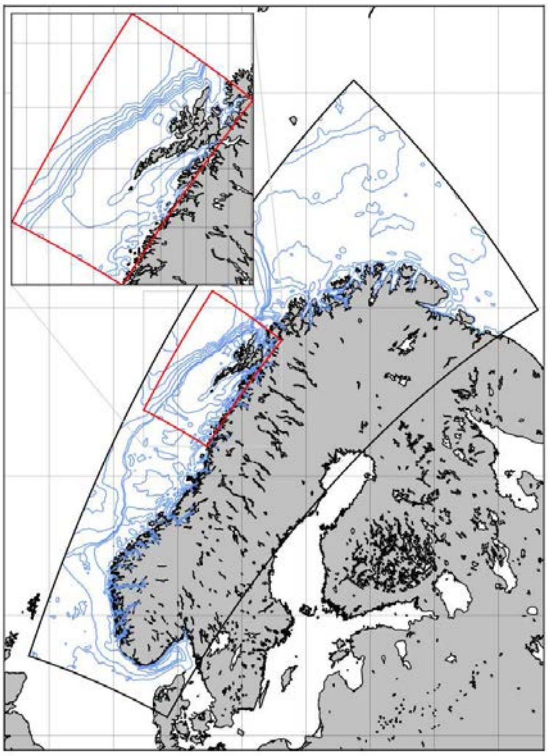

Figure 6. The model domain. The full domain of "NorKyst800" is shown with the black border while our coarser subdomain is shown with the red border.

4.1 Model grid and forcing data

The model domain of the realistic model simulations is a subset of the operational high-resolution ocean model at MET Norway (Albretsen et al., 2011) centred around the Lofoten and Vesterålen archipelago. The model has 35 vertical layers with increased resolution near the surface. This model setup has also been used for transport estimates of northeastern Arctic cod eggs and larvae, and a more thorough validation using in situ and drifter data is presented in Röhrs et al. (2014). As ocean data assimilation requires extensive supercomputing resources, the horizontal resolution has been decreased from 800 m to 2.4 km compared to the operational setup.

The lateral boundary conditions are retrieved from the operational setup at 800 m resolution, using 3-hourly fields of sea surface elevation, temperature, salinity, and currents. To remove fine-scale features from the high-resolution fields, that are unresolved in the coarser grid, the fields are averaged over 3×3 grid points before they are interpolated to the coarser grid.

The simulations use open boundary conditions for sea surface elevation and barotropic currents (Chapman, 1985; Flather, 1976). For tracers and baroclinic velocities, boundary conditions as described in Marchesiello et al. (2001) are used. The adjoint and tangent linear models do not have the same options for boundary conditions, however, so that clamped boundary conditions with a sponge layer are applied for these.

As atmospheric forcing we use hourly fields of air temperature and humidity 2 m above ground, 10 m winds, sea level pressure, cloud cover, and precipitation from MET Norway's operational weather forecast at 4 km resolution (Kristiansen et al., 2009).

A spin-up model simulation was initialized at 15 February 2013 from the smoothed high-resolution fields, from the operational setup, and run through 15 April 2013. The initial conditions for the assimilation simulations were obtained from the spin-up simulation.

4.2 Configuration of the data assimilation system

The configuration of the assimilation system in the realistic experiment is based on the results from the idealized case (see Sect. 3.3). Overall, the parameters values we find to be optimal in the idealized case are also optimal in the realistic case, with the exception of the horizontal error correlation length scale, which is increased. Based on the outcome of a series of tests, we proceed with horizontal background error correlation scales of 10 km, 10 inner and 2 outer loops.

To further assess the impact of the assimilation window length on the performance of the assimilation system, a twin experiment was conducted with the realistic model setup. A model simulation covering the winter months of 2011 was used as the true ocean state. Observations of u and v, in an area similar to that of HF radar coverage during the field campaign, were collected from the true state at every hour for a duration of 72 h. Random errors, with mean value of zero, were added to the observations. A period in 2013 with similar weather conditions was identified, and used as initial conditions for the assimilation experiments. The assimilation system was run for this 72 h period several times, successively decreasing the window length from 72 to 3 h. Comparing surface currents in the resulting analyses with the "true" state, we find the assimilation window length to have little impact on analysis quality. Based on the results from the idealistic experiments, as well as results from the realistic model with real observations, a window length of 24 h has been used in the following experiments.

In our tests, we also experimented with correlated observation errors in u and v (which is inevitable due to the way total vectors are calculated). The difference between runs with correlated vs. uncorrelated errors added to the synthetic observations was marginal.

We evaluate the performance of the data assimilation system using independent observations from the field campaign (Sect. 2); that is, observations that have not been used during the data assimilation and, therefore, serve as an independent measure of skill.

4.3 Comparison with surface drifters

Ocean forecasts are used for input to trajectory models, which predict the drift of, e.g. oil spills or objects in the sea. Thus, the ability of the forecast to reproduce the trajectories of the surface drifters is a good measure of forecast skill.

To evaluate the error of the assimilated HF radar observations we compare radial HF radar currents with the corresponding component of drifter speeds, shown in Fig. 7. Only radials from the two northernmost HF radars, Hovden and Nyksund, are included due to few drifter positions within the range of the Litløy radar. We find the overall agreement between the two data sources to be good, with a correlation coefficient of 0.72.

As the drifters are rapidly advected northwards after deployment and thus leaving the range of the HF radars, the results discussed in this section are limited to a single data assimilation cycle. The experiments are started on 18 March 2013 at 00:00 UTC. IS4DVAR is run for 24 h, assimilating observations collected during this period and producing modified initial conditions for 18 March 00:00 UTC. Next, a 5-day free simulation is run, initiated from this updated ocean state. In the following discussions, the first day of these simulations is termed "analysis", while the remaining 4-day period is termed "forecast". This is due to the fact that the observations taken within the first 24 h were used during assimilation. It should be noted that the atmospheric forcing used in these experiments is of higher quality than what would have been available in a near real-time setting, which affects the predictability of the ocean forecast.

This procedure has been repeated three times, with different sets of observations to assess the impact the different observation data sets have on the analysis and subsequent forecast. During the first simulation, only CTD hydrography profiles (both temperature and salinity) were assimilated (six profiles just south of the HF coverage area fall within the assimilation window). The observation error standard deviations are set to 0.1 °C for temperature and 0.01 for salinity. These are the same values as used by Broquet et al. (2009) and, as argued in their paper, a choice that may enhance the impact of this observation type, which is typically limited in numbers.

In the following, results from this simulation will be denoted "CTD". The second simulation only included HF radar total vectors, and is denoted "HF", while the third simulation assimilated both CTD profiles and HF radar currents, and is denoted "ALL". Additionally, a control simulation, in which no data assimilation was performed, was conducted for the same time period, in the following denoted "CTRL".

During the free simulations, initiated from the analyses produced by IS4DVAR, simulated surface drifters are re-

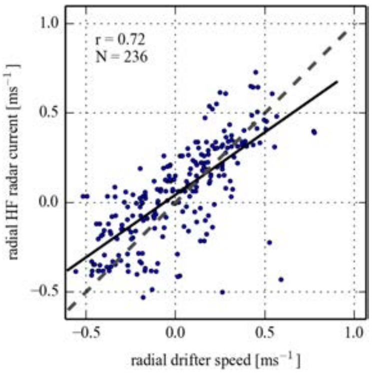

Figure 7. Correlation between radial HF radar currents and the corresponding component of drifter speeds.

leased in the positions occupied by the real surface drifters from the field campaign. Simulated surface drifters are released every 3 h at the position of the real drifters at that time. The depth of the simulated drifters is set to 65 cm below the sea surface, which corresponds to the average drogue depth of the iSLDMB drifters. In the same manner, numerical floats were released in the control simulation. We validate the results from the analysis period and the forecast period of the simulations separately.

The trajectories of the iSLDMB surface drifters released during the field campaign are compared with their numerical twin from the free simulations following the same methods as used in Röhrs et al. (2012). First, the vector correlation between predicted and observed drifter velocities is evaluated using an analysis similar to the method described in Davis (1985). The trajectories are split into 3 h long segments, and the drift velocities for these segments are then calculated. Defining the vector correlation as

$$r = 1 - \frac{\langle (\boldsymbol{v}_i - \boldsymbol{v}_j)^2 \rangle}{\langle \boldsymbol{v}_i^2 \rangle + \langle \boldsymbol{v}_j^2 \rangle}, \tag{2}$$

the correlation coefficients r for simultaneous pairs of drifter velocities may be calculated. The results are given as a value between 1 and −1, where a value of 1 means perfect correlation in both speed and direction, and a value of 0 means no correlation, while a value of −1 means that the drifters are anti-correlated, i.e. having opposite direction but the same speeds.

The resulting vector correlations between the assimilation simulations and the real drifters are shown in Fig. 8. The quality of the CTRL simulation decreases rapidly and, as the simulation enters into the forecast period, modelled and observed drifter velocities become uncorrelated. The CTD simulation follows the CTRL closely. In fact, the correlation coefficient for the CTD simulation is mostly below the CTRL simulation. As stated above, only six CTD profiles, sampled south of the area where the drifters were deployed, were used. We do not have CTD data co-located with any drifters and, therefore, cannot draw any conclusions regarding the impact of the CTD data. Assimilation of HF radar currents, on the other hand, significantly improves the simulated drifter velocities during both the analysis and the forecast period. Note that adding CTD hydrography to the HF currents further improves the model predictions during the first forecast day, which is in contrast to the detrimental effect of only using CTD observations. A likely explanation is that the addition of hydrographic observations acts as an additional constraint of the vertical density structure, demonstrating the importance of constraining all state variables.

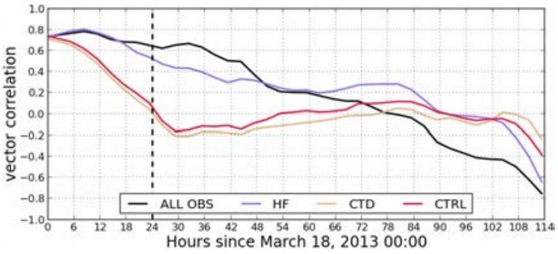

Figure 8. Vector correlation as a function of time, when comparing velocity vectors from simulated drifters with the corresponding values derived from the trajectories of the iSLDMB surface drifters. The vertical, dashed line indicates the shift from the analysis to the forecast period. A value of 1 means perfect correlation in both speed and direction and a value of 0 means no correlation, while a value of −1 means that the velocities are anti-correlated, i.e. same speeds but opposite directions.

The significance of the improvement has been tested comparing ALL and CTRL using a Wilcoxon rank–sum test. The improvement in current direction is statistically significant, while not so for the speeds. Our interpretation is that the major benefit of assimilating HF radar currents in these simulations is the correction of the current direction, e.g. adjustments in the positions of eddies and the coastal current. This test does not imply that no improvement in speed is obtained (Fig. 8 indicates that the results are better) but that the impact cannot be statistically verified with the limited observational data available.

The impact of data assimilation is also evaluated by comparing observed and predicted trajectories. For this comparison we use the method presented in Liu and Weisberg (2011), in which not only the end points of the observed and modelled trajectories are compared but also the entire history of the drifter trajectories. The normalized cumulative Lagrangian separation is defined as

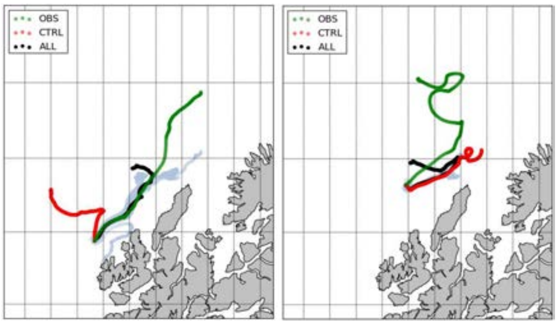

Figure 9. Drifter pathways for two different drifters as observed (green), predicted by CTRL (red) and predicted by ALL (black). The grey tracks shows the pathways of the perturbed initial position floats. The trajectories shown here were released at the start of the analysis.

Table 3. Skill score during analysis and forecast when comparing with the surface drifters.

Observation set	Analysis	Forecast
CTRL	0.42	0.18
HF	0.44	0.30
CTD	0.40	0.16
ALL	0.43	0.33

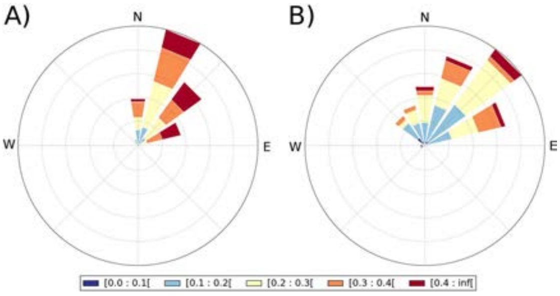

Figure 10. The current roses show current speed and direction distributions at the ADCP location during the observation campaign for **(a)** ADCP (at 1 m) and **(b)** HF radar. Only simultaneous observations have been used.

$$s = \sum_{i=1}^{N} d_i \Big/ \sum_{i=1}^{N} l_{\mathrm{o}i}, \tag{3}$$

where d_i is the separation distance between observed and modelled trajectory endpoints at time t_i after initialization, $l_{\mathrm{o}i}$ is the length of the observed trajectory and N is the total number of time steps evaluated. A skill score S is then defined as

$$S = \begin{cases} 1 - s, & \text{if } s \leq 1, \\ 0, & \text{if } s > 1. \end{cases} \tag{4}$$

High skill score means that observed and modelled trajectories agree well throughout the period under evaluation.

The skill score is calculated both for the analysis period and for the following 48 h of the forecast period. The results are shown in Table 3. Assimilation do improve predictions of drifter trajectories, although the impact is more limited compared to the drifter velocities. The results show that the skill improves when we consider periods longer than a day. In these cases, data assimilation seems to constrain the ocean circulation in such a way that the predicted trajectories does not stray as far away from the observed paths as they do in a free simulation. As an example of the ability of the model to predict pathways of drifting objects before and after assimilation, two examples of modelled versus observed trajectories are shown in Fig. 9. Note that the drifter in the left panel is released within the area covered by the HF radar antennas, while the drifter in the right panel is released outside of the coverage area.

4.4 Comparison with ADCP measurements

We proceed by comparing model results with current measurements from the ADCP rig deployed in our area of interest. A brief comparison of the HF radar total currents with the ADCP measurements is shown in Fig. 10. Hourly averages of the ADCP observations at 1 m depth have been generated to better match the HF observations, and only observations from periods where observations from both sources are available are included. The ADCP measures greater current speeds than the HF radar, which may be due to the fact that the HF radar currents are spatially averaged as well as temporally. It should also be noted that the dominating current direction is slightly more eastward in the HF measurements and that the current directions measured by the HF radars exhibit greater spread.

The results shown in this section are based on 10 sequential data assimilation cycles, where HF radar currents as well as CTD profiles of temperature and salinity are assimilated. Starting from the analysis of the “ALL” experiment described above, the model state at the end of the assimilation window is used as the initial condition for a new assimilation cycle, thus, generating an analysis for the following day. This procedure is then repeated. From each resulting analysis a forecast run is initiated, in the same way as described above. Each forecast thus has a 4-day overlap with the forecast from the previous day.

We compare the results from these forecasts with the speed and direction measured by the ADCPs. The upper ADCP measured currents starting 0.5 m below the surface and down to 8 m in vertical bins of 25 cm, while the lower ADCP measures currents from 41 m to the surface in 1 m bins. From the lower ADCPs, only data below 8 m are used for validation.

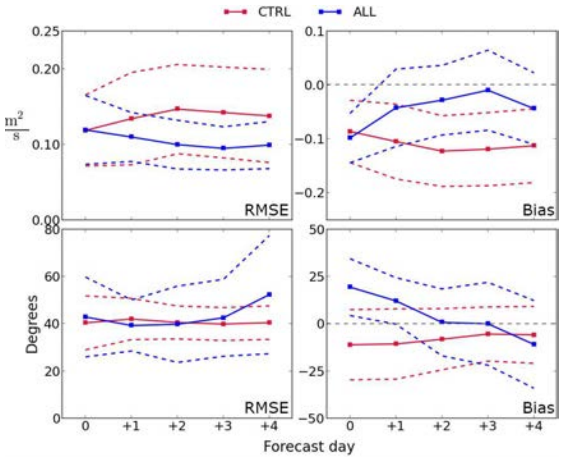

Figure 11. RMSE and bias of transport speed (upper panels) and direction (lower panels) in the water column stretching from 0.5 to 8 m below the surface relative to the ADCP, as a function of forecast day.

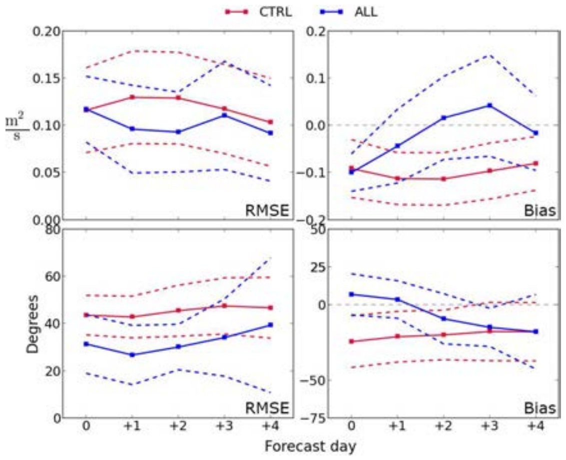

Figure 12. RMSE and bias of transport speed (upper panels) and direction (lower panels) in the water column stretching from 8 to 41 m below the surface relative to the ADCP, as a function of forecast day.

To account for discrepancies between the vertical resolution of the model and the observations, we have chosen to focus the comparison on depth-integrated values. To evaluate the depth-integrated flow, we integrate from 0.5 m below the surface and down to 8 m for the upper ADCP, while for the lower ADCP we integrate from 8 m and down to 41 m. Transport magnitude and direction, given by the vertically integrated ADCP currents, are compared with the same quantities calculated from model results. Root mean square error (RMSE) and bias values are calculated as a function of forecast day, and values corresponding to the same forecast day number are binned together

From inspection of time series of transport magnitude and direction (not shown), we find that the upper ADCP measures a transport with mostly north–northeasterly heading during the period. The CTRL simulation predicts a north–northwest-headed current during the period in question. In addition to the discrepancy in direction, the transport magnitude predicted by the CTRL is too weak during the whole simulation in both upper and lower sections. Figures 11 and 12 show mean RMSE and mean bias of the series of simulations along with the means ± 1 standard deviation.

In both upper and lower sections it is evident that assimilation causes a reduction in speed RMSE and bias compared with the control run. The change in bias indicates that the predicted current remains more energetic throughout the forecast period. As for direction, the assimilation runs perform better than the control run in the lower section, with reduced RMSE for all forecast days. In the upper section, however, direction predictions seem to be of similar quality in the assimilation runs as in the control run. A possible explanation for this might be that the currents in the near-surface layers are strongly affected by the wind stress. Any changes made to the current in the near-surface layers by the assimilation system may thus have a short life span in the model if the wind stress imposed on the surface yields a different direction. Changes at deeper depths, on the other hand, have a greater chance of being sustained. This advocates for the inclusion of surface forcing in the control vector.

5 Discussion and concluding remarks

In the presented experiments we have assimilated HF radar and hydrography profiles in both an idealistic and a realistic model. In both cases hydrography profiles were sparse in comparison with the number of HF radar current observations. The realistic experiments were carried out for a specific time period and the results are therefore influenced by local weather conditions and do not necessarily represent the variations in predictability of different flow regimes.

Starting with an idealized test case with synthetic HF total currents and hydrography profiles being assimilated, we find that it is necessary to keep the horizontal error correlation length scales fairly small. The strong currents along the steep topography are associated with sharp fronts and, when large correlation length scales are used, the information provided by the observations may be erroneously spread across these fronts. As the incremental strong constraint 4D-Var is based on repeated iterations of a tangent linear version of the model and its associated adjoint model, the linearization assumption needs to hold throughout the assimilation window. In our case, with strongly nonlinear and energetic currents, this window needs to be quite short. Both the idealized and the realistic experiments give best results when the window is 24 h. We also find that relinearizing the preliminary solution through outer loops is beneficial for the performance of the data assimilation system. These findings are confirmed when similar experiments are performed with a realistic model with real observational data.

Hydrographic observations alone did not yield a significant positive impact on the surface currents, not even in the idealized experiments where more (synthetic) profiles were assimilated, compared to the realistic case. The profiles do, however, have a positive impact on the density field in the model, reducing analysis salinity RMSE from 0.31 in the control run to 0.16 in the experiment where both HF currents and hydrography profiles were assimilated. Also, the temperature RMSE is reduced from 3.0 to 2.2 °C. As the ship was moving in the opposite direction of the dominating currents, ship-based observations of temperature and salinity during the forecast period have little value for validation purposes. Comparison with satellite observations of sea surface temperature (not shown here), however, suggests that temperature predictions are improved throughout the forecast when CTD profiles are assimilated.

With assimilation of HF currents, on the other hand, the current forecasts are improved. Gridded fields of surface currents, with temporal resolution of 1 h provide the data assimilation system with improved positioning of eddies and more realistic current speed. In the idealized experiments we even see improvement in the temperature. There are indications that this also holds in the realistic experiments, but independent observations are too sparse to confirm this. Using both HF currents and CTD profiles for assimilation yields the best results. Although CTD profiles did not improve the current forecasts alone, together with the HF radar surface currents they seem to add an additional constraint on the circulation. These results demonstrate the importance of sampling not only the surface but also the subsurface density structure.

We conclude that using HF radar currents in operational data assimilation systems is useful for improving predictions of upper ocean transports, which is highly relevant for oil spill mitigation purposes and search-and-rescue operations. Assimilation of the HF radar radial components directly by utilizing a suitable observation operator holds the potential for further improvement and is the focus of ongoing efforts. Using radials will increase both the number of observations available for assimilation as well as the coverage area. Errors introduced by the algorithms combining radials from two or more antennas will also be eliminated.

Acknowledgements. This work was funded by the Norwegian Clean Seas Association for Operating Companies (NOFO) and ENI Norge A/S, with contributions from the Research Council of Norway (196438/BIOWAVE and 207541/OILWAVE) for analysing field data. The authors would like to thank Svein Sundby and Frode Vikebø(IMR) for helpful discussions and kind assistance during the planning phase, and Erik Berg (IMR) and the captain and crew of R/V *Johan Hjort*, for their kind assistance with the drifter deployments. We would also like to thank Ronald Pedersen (IMR), Tor Gammelsrød (UiB), Erik Kvaleberg and Anne Hesby (Royal Navy) for the loan of instruments and assistance with the ADCP rig. Assistance from the captains and crews of the M/V *NSO Crusader* and R/V *Håkon Mosby* when deploying and recovering the ADCP rig is also gratefully acknowledged.

Edited by: M. Hoppema

References

Albretsen, J., Sperrevik, A. K., Staalstrøm, A., Sandvik, A. D., Vikebø, F., and Asplin, L.: NorKyst-800 report no. 1: User manual and technical descriptions, Tech. Rep. 2, Institute of Marine Research, Bergen, Norway, available at: http://www.imr.no/filarkiv/2011/07/fh_2-2011_til_web.pdf/nb-no (last access: 5 March 2015), 2011.

Barrick, D. E., Evans, M. W., and Weber, B. L.: Ocean surface currents mapped by radar, Science, 198, 138–144, 1977.

Barth, A., Alvera-Azcarate, A., and Weisberg, R. H.: Assimilation of high-frequency radar currents in a nested model of the West Florida Shelf, J. Geophys. Res., 113, C08033, doi:10.1029/2007JC004585, 2008.

Blockley, E. W., Martin, M. J., McLaren, A. J., Ryan, A. G., Waters, J., Lea, D. J., Mirouze, I., Peterson, K. A., Sellar, A., and Storkey, D.: Recent development of the Met Office operational ocean forecasting system: an overview and assessment of the new Global FOAM forecasts, Geosci. Model Dev., 7, 2613–2638, doi:10.5194/gmd-7-2613-2014, 2014.

Brassington, G. B., Pugh, T., Spillman, C., Schulz, E., Beggs, H., Schiller, A., and Oke, P. R.: BLUElink> Development of operational oceanography and servicing, J. Res. Pract. Inf. Tech., 39, 151–164, 2007.

Breivik, Ø. and Saetra, Ø.: Real time assimilation of HF radar currents into a coastal ocean model, J. Marine Syst., 28, 161–182, 2001.

Broquet, G., Edwards, C. A., Moore, A. M., Powell, B. S., Veneziani, M., and Doyle, J. D.: Application of 4D-Variational data assimilation to the California Current System, Dynam. Atmos. Oceans, 48, 69–92, 2009.

Chapman, D. C.: Numerical treatment of cross-shelf open boundaries in a barotropic coastal ocean model, J. Phys. Oceanogr., 15, 1060–1075, 1985.

Chapman, R. D., Shay, L. K., Graber, H. C., Edson, J. B., Karachintsev, A., Trump, C. L., and Ross, D. B.: On the accuracy of HF radar surface current measurements: Intercomparisons with ship-based sensors, J. Geophys. Res.-Oceans, 102, 18737–18748, 1997.

Christensen, K. H., Sperrevik, A. K., and Röhrs, J.: The spring 2013 field experiment of the ENI/NOFO HF radar project, Tech. Rep. 25, Norwegian Meteorological Institute, Oslo, Norway, available at: http://met.no/Forskning/Publikasjoner/MET_report/2013/filestore/fieldEXP.pdf (last access: 5 March 2015), 2013.

Courtier, P., Thépaut, J.-N., and Hollingsworth, A.: A strategy for operational implementation of 4D-Var, using an incremental approach, Q. J. Roy. Meteorol. Soc., 120, 1367–1387, 1994.

Davis, R. E.: Drifter observations of coastal surface currents during CODE: The method and descriptive view, J. Geophys. Res., 90, 4741–4755, 1985.

Dimet, F.-X. L. E. and Talagrand, O.: Variational algorithms for analysis and assimilation of meteorological observations: theoretical aspects, Tellus A, 38, 97–110, 1986.

Evensen, G.: The Ensemble Kalman Filter: theoretical formulation and practical implementation, Ocean Dynam., 53, 343–367, 2003.

Flather, R. A.: A tidal model of the north-west European continental shelf, Memoires de la Society Royal des Sciences de Liege, 10, 141–164, 1976.

Fu, L.-L., Christensen, E. J., Yamarone, C. A., Lefebvre, M., Ménard, Y., Dorrer, M., and Escudier, P.: TOPEX/POSEIDON mission overview, J. Geophys. Res., 99, 24369–24381, 1994.

Gurgel, K.-W., Antonischki, G., Essen, H.-H., and Schlick, T.: Wellen Radar (WERA): a new ground-wave HF radar for ocean remote sensing, Coastal Eng., 37, 219–234, 1999.

Gustafsson, N.: Discussion on “4D-Var or EnKF?”, Tellus A, 59, 774–777, 2007.

Isachsen, P. E.: Baroclinic instability and eddy tracer transport across sloping bottom topography: How well does a modified Eady model do in primitive equation simulations?, Ocean Model., 39, 183–199, 2011.

Isachsen, P. E., Koszalka, I., and LaCasce, J. H.: Observed and modeled surface eddy heat fluxes in the eastern Nordic Seas, J. Geophys. Res., 117, C08020, doi:10.1029/2012JC007935, 2012.

Kalnay, E., Li, H., Miyoshi, T., Yang, S.-C., and Bakkabrera-Poy, J.: 4-D-Var or ensemble Kalman filter?, Tellus A, 59, 758–773, 2007.

Kjelaas, A. G. and Whelan, C.: Rapidly deployable SeaSonde for modeling oil spill response, Sea Technol., 52, 10–13, 2011.

Kristiansen, J., Bjørge, D., Berge, H., Simonsen, M., Torheim, T., Aasen, I.-L., Rooney, G., and Edwards, J.: Improving the screen temperature forecasts of the Norwegian configuration of the UM: on model interoperability with respect to soil initial conditions, in: Unified Model User Workshop, Exeter, United Kingdom, 9–11 November, 2009.

Liu, Y. and Weisberg, R. H.: Evaluation of trajectory modeling in different dynamic regions using normalized cumulative Lagrangian separation, J. Geophys. Res., 116, C09013, doi:10.1029/2010JC006837, 2011.

Marchesiello, P., McWilliams, J. C., and Shchepetkin, A.: Open boundary conditions for long-term integration of regional oceanic models, Ocean Model., 3, 1–20, 2001.

Moe, H., Ommundsen, A., and Gjevik, B.: A high resolution tidal model for the area around the Lofoten Islands, northern Norway, Cont. Shelf Res., 22, 485–504, 2002.

Moore, A. M., Arango, H. G., Di Lorenzo, E., Miller, A. J., and Cornuelle, B. D.: An adjoint sensitivity analysis of the Southern California Current circulation and ecosystem, J. Phys. Oceanogr., 39, 702–720, 2009.

Moore, A. M., Arango, H. G., Broquet, G., Edwards, C., Veneziani, M., Powell, B., Foley, D., Doyle, J. D., Costa, D., and Robinson, P.: The Regional Ocean Modeling System (ROMS) 4-dimensional variational data assimilation systems: Part II – Performance and application to the California Current System, Prog. Oceanogr., 91, 50–73, 2011a.

Moore, A. M., Arango, H. G., Broquet, G., Edwards, C., Veneziani, M., Powell, B., Foley, D., Doyle, J. D., Costa, D., and Robinson, P.: The Regional Ocean Modeling System (ROMS) 4-dimensional variational data assimilation systems: Part III – Observation impact and observation sensitivity in the California Current System, Prog. Oceanogr., 91, 74–94, 2011b.

Moore, A. M., Arango, H. G., Broquet, G., Powell, B. S., Weaver, A. T., and Zavala-Garay, J.: The Regional Ocean Modeling System (ROMS) 4-dimensional variational data assimilation systems: Part I – System overview and formulation, Prog. Oceanogr., 91, 34–49, 2011c.

Oke, P. R., Allen, J. S., Miller, R. N., Egbert, G. D., and Kosro, P. M.: Assimilation of surface velocity data into a primitive equation coastal ocean model, J. Geophys. Res., 107, 5–1, 2002.

Oke, P. R., Brassington, G. B., Griffin, D. A., and Schiller, A.: Ocean data assimilation: a case for ensemble optimal interpolation, Australian Meteorological and Oceanographic Journal, 59, 67–76, 2010.

Paduan, J. D. and Shulman, I.: HF radar data assimilation in the Monterey Bay area, J. Geophys. Res., 109, CO7S09, doi:10.1029/2003JC001949, 2004.

Paduan, J. D. and Washburn, L.: High-frequency radar observations of ocean surface currents, Annual Review of Marine Science, 5, 115–136, 2013.

Paduan, J. D., Kim, K. C., Cook, M. S., and Chavez, F. P.: Calibration and validation of direction-finding high-frequency radar ocean surface current observations, IEEE J. Oceanic Eng., 31, 862–875, 2006.

Powell, B. S., Arango, H. G., Moore, A. M., Di Lorenzo, E., Milliff, R. F., and Foley, D.: 4DVAR data assimilation in the intra-Americas sea with the Regional Ocean Modeling System (ROMS), Ocean Model., 25, 173–188, 2008.

Rayner, N. A., Parker, D. E., Horton, E. B., Folland, C. K., Alexander, L. V., Rowell, D. P., Kent, E. C., and Kaplan, A.: Global analyses of sea surface temperature, sea ice, and night marine air temperature since the late nineteenth century, J. Geophys. Res.-Atmos., 108, 4407, doi:10.1029/2002JD002670, 2003.

Roemmich, D., Johnson, G. C., Riser, S., Davis, R., Gilson, J., Owens, W. B., Garzoli, S. L., Schmid, C., and Ignaszewski, M.: The Argo Program: Observing the global ocean with profiling floats, Oceanography, 22, 34–43, 2009.

Röhrs, J., Christensen, K. H., Hole, L. R., Broström, G., Drivdal, M., and Sundby, S.: Observation-based evaluation of surface wave effects on currents and trajectory forecasts, Ocean Dynam., 62, 1519–1533, 2012.

Röhrs, J., Christensen, K. H., Vikebø, F., Sundby, S., Saetra, Ø., and Broström, G.: Wave-induced transport and vertical mixing of pelagic eggs and larvae, Limnol. Oceanogr., 59, 1213–1227, 2014.

Röhrs, J., Sperrevik, A. K., Christensen, K. H., Broström, G., and Breivik, Ø.: Comparison of HF radar measurements with Eulerian and Lagrangian surface currents, Ocean Dynam., in press, 2015.

Sakov, P., Counillon, F., Bertino, L., Lisæter, K. A., Oke, P. R., and Korablev, A.: TOPAZ4: an ocean-sea ice data assimilation system for the North Atlantic and Arctic, Ocean Sci., 8, 633–656, doi:10.5194/os-8-633-2012, 2012.

Wentz, F. J., Gentemann, C., Smith, D., and Chelton, D.: Satellite measurements of sea surface temperature through clouds, Science, 288, 847–850, 2000.

Zavala-Garay, J., Wilkin, J. L., and Arango, H. G.: Predictability of mesoscale variability in the east australian current given strong-constraint data assimilation, Jo. Phys. Oceanogr., 42, 1402–1420, 2012.

Zhang, W. G., Wilkin, J. L., Levin, J. C., and Arango, H. G.: An adjoint sensitivity study of buoyancy- and wind-driven circulation on the New Jersey inner shelf, J. Phys. Oceanogr., 39, 1652–1668, 2009.

Zhang, W. G., Wilkin, J. L., and Arango, H. G.: Towards an integrated observation and modeling system in the New York Bight using variational methods. Part I: 4DVAR data assimilation, Ocean Model., 35, 119–133, 2010.

Paper III

5.3 Impact of data assimilation on Eulerian versus Lagrangian estimates of upper ocean circulation

Ann Kristin Sperrevik, Johannes Röhrs, and Kai Håkon Christensen

in revision for Journal of Geophysical Research - Oceans

Impact of data assimilation on Eulerian versus Lagrangian estimates of upper ocean circulation

Ann Kristin Sperrevik[1], **Johannes Röhrs**[1], **and Kai Håkon Christensen**[1,2]

[1]Norwegian Meteorological Institute, Oslo, Norway
[2]University of Oslo, Oslo, Norway

Abstract

Using four-dimensional variational analysis, we produce an estimate of the state of a coastal region in Northern Norway during the late winter and spring in 1984. We use satellite sea surface temperature and in-situ observations from a series of intensive field campaigns, and obtain a more realistic distribution of water masses both in the horizontal and the vertical than a pure downscaling approach can achieve. Although the distribution of Eulerian surface current speeds are similar, we find that they are more variable and less dependent on model bathymetry in our reanalysis compared to a hindcast produced using the same modeling system. Lagrangian drift currents on the other hand are significantly changed, with overall higher kinetic energy levels in the reanalysis than in the hindcast, particularly in the sub-inertial frequency band.

1 Introduction

Modeling the transport of plankton, pollution, and drifting objects presents an ongoing challenge in operational oceanography. To obtain realistic Lagrangian trajectories, circulation models need to resolve the horizontal structure of the time-varying currents as well as correctly describe the vertical dynamical balances that determine the vertical position or distribution of the quantity of interest. Shelf and coastal seas are of particular interest as human activity is concentrated near the coast, and shelf seas are most relevant for primary production, fisheries, and oil exploitation.

Ocean circulation models set up for a specific coastal or shelf sea are commonly used to provide the Eulerian current fields used for Lagrangian transport studies. Such regional ocean circulation models crucially depend on initial and boundary conditions from coarser models, which may lack important details relevant for the specific region. Increasing the model resolution usually implies better physics as more processes and scales are resolved, but errors propagating in from parent grids reduces model skill. Traditionally, ocean model errors have mainly been associated with initialization, and errors due to the boundary conditions have been most pronounced in limited area numerical weather prediction (NWP) models (e.g., Warner et al., 1997). Such limitations in predictability due to the boundary conditions are becoming increasingly relevant in the high resolution ocean models used for coastal applications.

One way to improve a regional ocean model is through data assimilation (DA), combining observations and model fields in an optimal way to provide the best possible estimate of the true state. Ocean DA is rapidly developing as advanced methods are inherited from NWP and adapted to ocean circulation models. For instance, the four-dimensional variational analysis scheme used in this study (Moore et al., 2011a,b,c) uses linear model physics to propagate information in time, which allows the model state to be adjusted in a dynamically consistent way, even though the observations are not taken at the analysis time. In addition, the analysis scheme allows us to correct for errors in the lateral boundary conditions and the surface forcing.

Particle transport crucially depends on transient current features such as tides and eddies. In the uppermost part of the ocean the Stokes drift and the wind- and wave-induced mixing become important factors, particularly for buoyant particles (Drivdal et al., 2014; Röhrs et al., 2014). To realistically resolve the small scale transient currents, it is not only required that the ocean model has sufficient spatial resolution, but also that the model has a correct water mass distribution in order to resolve frontal instabilities and the baroclinic response to large scale forcing.

The focus region in this work is the Lofoten and Vesterålen shelf sea in northern Norway (see Fig. 1), where we

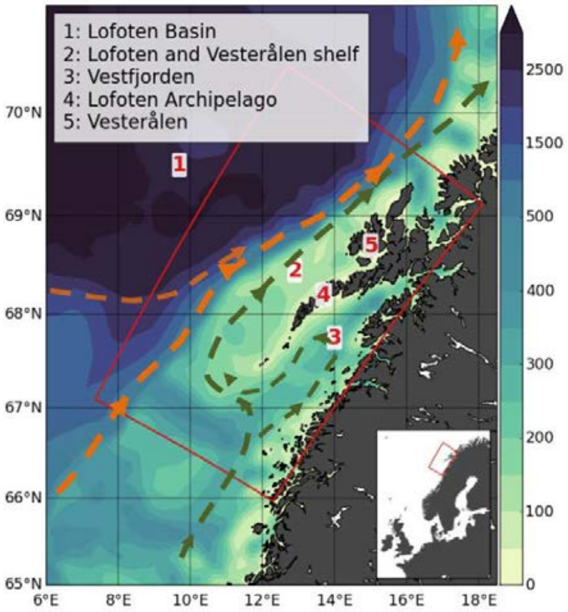

Figure 1. Study area in Northern Norway. Ocean depth is illustrated by shading, while the red box indicates the model domain. The overall pathways of the Norwegian Atlantic Current and the Norwegian Coastal Current are indicated in orange and green, respectively.

find the primary spawning ground for Northeast Arctic Cod (*Gadus morhua*) in addition to rich oil and gas reservoirs. Cod eggs spawned in Vestfjorden are transported with the Norwegian Coastal Current and the Norwegian Atlantic Current to the nursery grounds in the Barents Sea. The Lofoten and Vesterålen area has so far been protected from oil and gas exploitation as a preventive measure, but the continuation of this state of affairs remains uncertain. Previous studies of transport processes in this region have focused on connectivity (primarily cod egg and larvae transport), oil spill drift modeling, and marine ecosystem models (e.g., De Hoop et al., 2016; Eide et al., 2007; Svendsen et al., 2007; Vikebø et al., 2013).

The large scale pathways of zooplankton and ichtyoplankton from the Lofoten and Vesterålen shelf sea northward to the Barents Sea are generally known (Ådlandsvik and Sundby, 1994; Vikebø et al., 2007). Recently, the focus have turned to smaller scales and the upper ocean dynamics that impact on particle transport near the coast. Particularly interesting for this study is the work of Myksvoll et al. (2014), who demonstrate the impact of vertical stratification. The eggs of the Coastal cod are denser than the Northeast Arctic cod eggs, and hence have a different distribution with depth, resulting in a retention of Coastal cod eggs near the coast. Field studies using different types of drifters also demonstrate a remarkable variation in the drift currents with depth, implying that the direct impact of the atmospheric forcing on the transport diminishes very rapidly away from the surface (Röhrs and Christensen, 2015). Previous studies thus point to two different aspects of the role of stratification for the transport: (i) the role of stratification for the vertical distribution of buoyant particles, and (ii) the role of stratification for the intrinsic ocean response to atmospheric forcing. It is the second point that we will focus on here, and we will compare our results to a downscaled version of the SVIM hindcast archive, which has been used in several previous transport studies in this region (Kvile et al., 2016; Langangen et al., 2016; Stige et al., 2015).

We present a reanalysis of the Lofoten and Vesterålen shelf sea circulation made with a four-dimensional variational DA scheme. The observations are taken from a series of intensive field campaigns in 1984 (Sundby and Bratland, 1987) and from re-processed satellite sea surface temperature (SST) measurements. We emphasize on the impact of improved hydrography on the overall circulation and the Lagrangian transport statistics. The outline of the paper is as follows: In Sec. 2 we briefly describe the oceanography of the Lofoten and Vesterålen shelf sea; in Sec. 3 we describe the numerical model and the observations; in Sec. 4 we summarize our results. Finally, Sec. 5 contains a brief discussion and some concluding remarks.

2 The Lofoten and Vesterålen shelf sea

The shelf in northern Norway is restricted to the east by a mountainous coastline with deep fjords and numerous islands and skerries, and there is a steep shelf break toward the deep Norwegian Sea basin to the west. This shelf break controls a branch of the relatively warm and saline Norwegian Atlantic Current (NAC). On the inner part of the shelf we find the fresh and cold Norwegian Coastal Current (NCC), which contains the river runoff from all along the Norwegian coast and freshwater originating in the Baltic Sea.

The Vesterålen shelf sea off the Lofoten and Vesterålen archipelago (Fig. 1) is the narrowest part of the Norwegian shelf, being about 60 km wide. On this part of the shelf, the NAC and the NCC converge, giving rise to baroclinic instabilities and eddies shedding off to the Lofoten Basin (Isachsen, 2015; Poulain et al., 1996; Volkov et al., 2015). On the inner part of the shelf, a branch of the NCC enters Vestfjorden, a wide bay separated from the surrounding shelf sea by a deep sill ($\sim$230 m) in the south and the Lofoten archipelago to the west. The outflow from Vestfjorden is primarily found on the western side, along the Lofoten archipelago. The general circulation pattern in Vestfjorden is cyclonic, occasionally interrupted by complex transient circulation patterns that develop in response to local winds.

The winds during winter and spring in Vestfjorden are often from northeast due to catabatic flow of cold air from the mainland. These winds force near-surface water in Vestfjorden toward the outer part of the shelf. A second mode of wind driven circulation is set up by southwesterly winds during the passage of low pressure systems. In such cases, the cyclonic circulation pattern in Vestfjorden is interrupted and water masses are retained in Vestfjorden and piled up towards the inner parts (Ellertsen et al., 1981; Furnes and Sundby, 1981). The water flushes out when the wind drops, and is driven to the Lofoten and Vesterålen shelf by rotational effects. This interaction between Vestfjorden and the Lofoten and Vesterålen shelf is repeated throughout winter and spring, and is a source of great variability in the NCC.

The Vestfjorden bay is up to 500 m deep and below the surface layer there is remnant Atlantic water. The water in Vestfjorden is stably, albeit weakly, stratified: since the deeper Atlantic water is warmer than the coastal water, the temperature is often found to increase with depth. Depending on the wind situation, there is upwelling of Atlantic water along the rim of the bay, with southwesterly winds resulting in upwelling of Atlantic water toward the Lofoten archipelago. The stratification on the shelf and on the shelf slope depends on both the amount of fresh water advected by the coastal current, the wind- and wave-induced mixing, and the amount of coastal upwelling and downwelling. The stratification exhibits a strong seasonal cycle both inside Vestfjorden and in the surrounding shelf sea. During late spring and summer, the stratification is enhanced due to increased runoff associated with snow melting, as well as solar heating of the surface layer, resulting in a wide and shallow NCC. In contrast, low runoff levels combined with surface cooling causes a deepening of the mixed layer during winter. In the cold season the NCC thus becomes narrow and deep.

The most dominant tidal constituents are the semi-diurnal lunar M2 component followed by the solar semi-diurnal S2. Very strong tidal flows in narrow sounds and shallow regions contribute to the coast-shelf exchange. The period of M2 (12.42h) is close to the inertial period (12.1h) in this region, and both the tides and inertial oscillations add to the variability of currents around the Lofoten archipelago.

3 Models and Observations

The numerical ocean model used in this study is the Regional Ocean Modeling System (ROMS), which is a free-surface, hydrostatic, primitive equation model with terrain-following vertical coordinates (Haidvogel et al., 2008; Shchepetkin and McWilliams, 2005). ROMS comes with a set of tools for strong and weak constraint four-dimensional variational (4D-Var) data assimilation, as well as a framework for assessing observation impacts and model sensitivities using adjoint techniques (Moore et al., 2011a, 2004, 2011b,c). In this study we utilize the strong constraint, incremental 4D-Var driver (IS4DVAR) to perform state estimation.

The model covers an area centered around the archipelago of Lofoten and Vesterålen in Northern Norway (Fig. 1), with a horizontal resolution of 2.4 km and with 35 vertical levels. This setup have been used in previous studies, assessing the impact of assimilating High Frequency radar observations on forecast skill (Sperrevik et al., 2015), and, at a higher resolution of 800 m, the impact of wave-current interactions and wave-induced mixing on the Lagrangian transport of cod eggs and larvae (Röhrs et al., 2014). We will present results from two different model realizations: (i) a downscaling of the SVIM archive (Lien et al., 2013, 2014) and (ii) a reanalysis generated by IS4DVAR using in-situ hydrography and satellite SST. These two model realizations will be denoted as SVIM-DS and ANA, respectively.

3.1 The SVIM downscaling

SVIM is a hindcast archive that covers the Nordic Seas and parts of the Arctic Ocean with a horizontal resolution of 4 km and with 32 vertical layers. The archive covers the time period from 1958 until present, being updated four times per year. Our downscaling, SVIM-DS, has the same atmospheric forcing as the original hindcast archive, with six-hourly fields of winds, temperature, humidity, mean sea level pressure, total cloud cover, and net precipitation from the Norwegian Reanalysis 10 km (NORA10) archive (Reistad et al., 2011). Daily means of salinity, potential temperature, sea surface elevation, and barotropic and baroclinic velocities from the SVIM archive are used both for initial and boundary conditions. The boundary conditions are applied using a combination of radiation and nudging conditions as proposed by Marchesiello et al. (2001), while surface elevation and barotropic currents are imposed following the recommendations of Flather (1976) and Chapman (1985). In addition, tidal forcing from the TPXO global inverse barotropic model of ocean tides (Egbert and Erofeeva (2002)) is applied. The model is also forced with daily estimates of river discharges from the Norwegian Water Resources and Energy Directorate (Beldring et al., 2001).

3.2 4D-Var reanalysis

The model configuration for the reanalysis is the same as for SVIM-DS, but due to limitations in the adjoint and tangent linear models used by IS4DVAR, clamped boundary conditions with a sponge layer are used for the baroclinic variables. The configuration of the IS4DVAR driver is similar to that of Sperrevik et al. (2015) with two exceptions: the assimilation window length is increased from 24 to 72 h, and the control vector now includes the open boundary conditions.

In IS4DVAR, the background error covariance matrix is estimated from a combination of a multivariate balance operator (not used here), a univariate covariance operator, and background error standard deviations provided in input files (Moore et al., 2011a). Here we have used a 3 years hindcast simulation to estimate monthly values of background error standard deviations. To account for seasonal changes in the stratification and the circulation patterns, the background errors in any given DA cycle is estimated using a weighted mean of the monthly values.

A reanalysis covering the time period of 1 January to 30 June 1984 is constructed in the following manner: The initial conditions for 1 January are retrieved from SVIM-DS, and a best estimate of the ocean state over the assimilation window is found by running IS4DVAR. The updated ocean state at the end of the assimilation window is then used as initial conditions for the next assimilation cycle. This procedure is repeated until the simulation reaches 30 June, by which a total of 61 assimilation cycles have been completed.

This sequential data assimilation procedure generates a reanalysis that is dynamically consistent within each assimilation window. The transition between adjacent assimilation windows will, however, not be continuous since the solution within a window is optimized for the observations available during the given period. Trajectory modeling requires continuous fields, and for this reason we have applied an incremental analysis update method (Ourmières et al., 2006). A continuous solution for the entire period is obtained by running the model with the same configuration as for SVIM-DS, but exchanging the boundary conditions and surface forcing with the corresponding fields from the IS4DVAR solution, and nudging temperature and salinity towards the analysis fields with a timescale of 12 h.

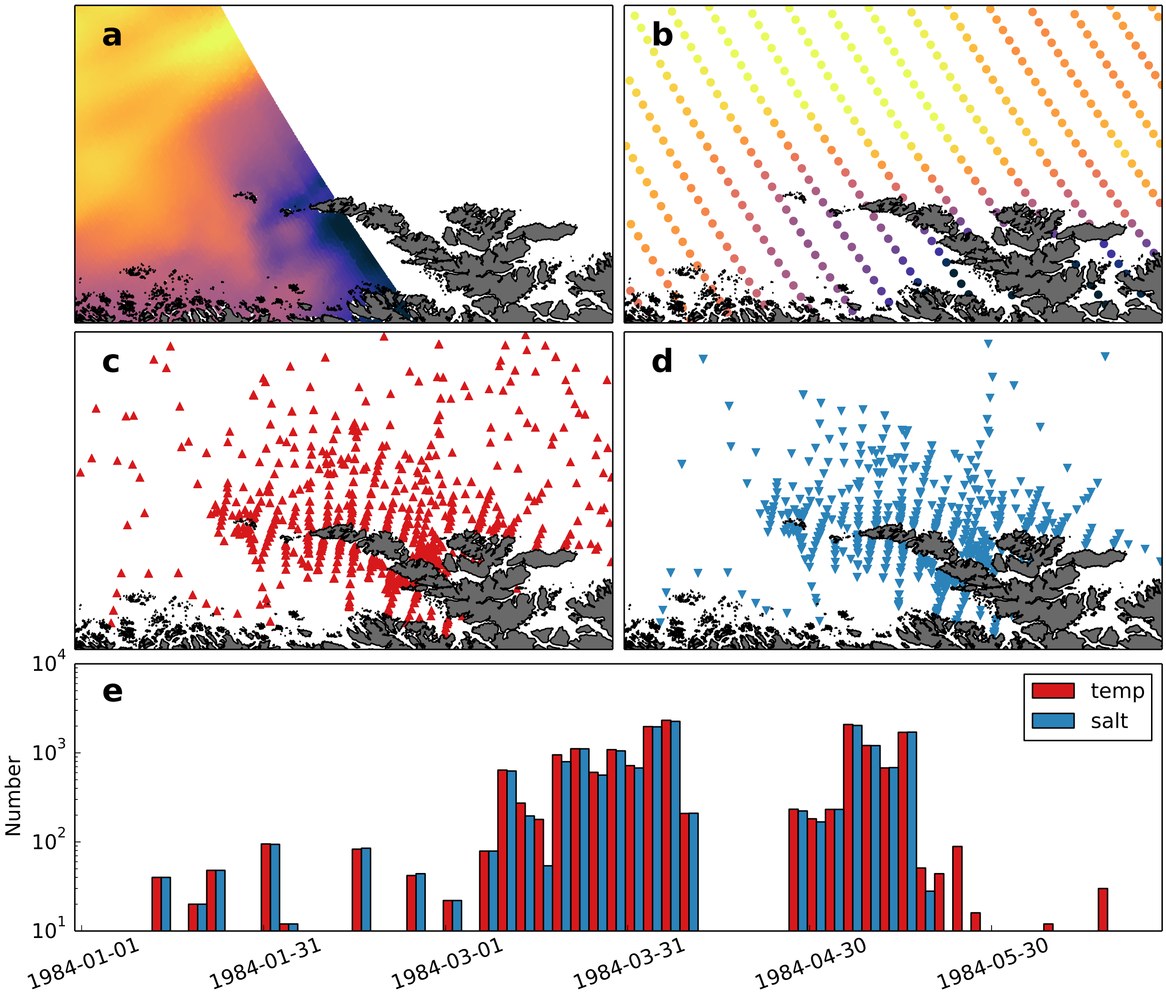

Figure 2. SST for 15 April 1984 from DMI (a) and NOAA (b). All in-situ temperature (c) and salinity (d) observations for the duration of the experiment, and the number of in-situ observations per assimilation cycle (e).

3.3 Observations

Two different SST data sets are used in the reanalysis. The first is the global SST analysis provided by the National Oceanic and Atmospheric Administration (Reynolds et al., 2007), which is produced by blending AVHRR data with in-situ measurements, generating daily averages at a 0.25 degree spherical grid. The second is a regional SST analysis provided by the Danish Meteorological Institute (also daily averages, see Høyer and She, 2007). This product has a spatial resolution of 0.03 degrees which is comparable to the resolution of our model, but it only covers the model domain up to 68°N. The coverage and resolution of the two products is illustrated in panels (a-b) of Fig. 2.

In-situ observations of temperature and salinity were retrieved from the EN4 data set available from the UK Met Office (Good et al., 2013). For the region of interest, the data set mainly consists of ship-borne CTD observations, collected during extensive cruises by the Institute of Marine Research during the spring months (Sundby and Bratland, 1987). As can be seen in panels (c-d) of Fig. 2, the observations are mainly from inside Vestfjorden and the Lofoten and Vesterålen shelf. In total there are 1272 profiles, taken as unique observation points with 5 or more measurements in the vertical, available for the period of the reanalysis. Fig. 2e shows the temporal distribution of

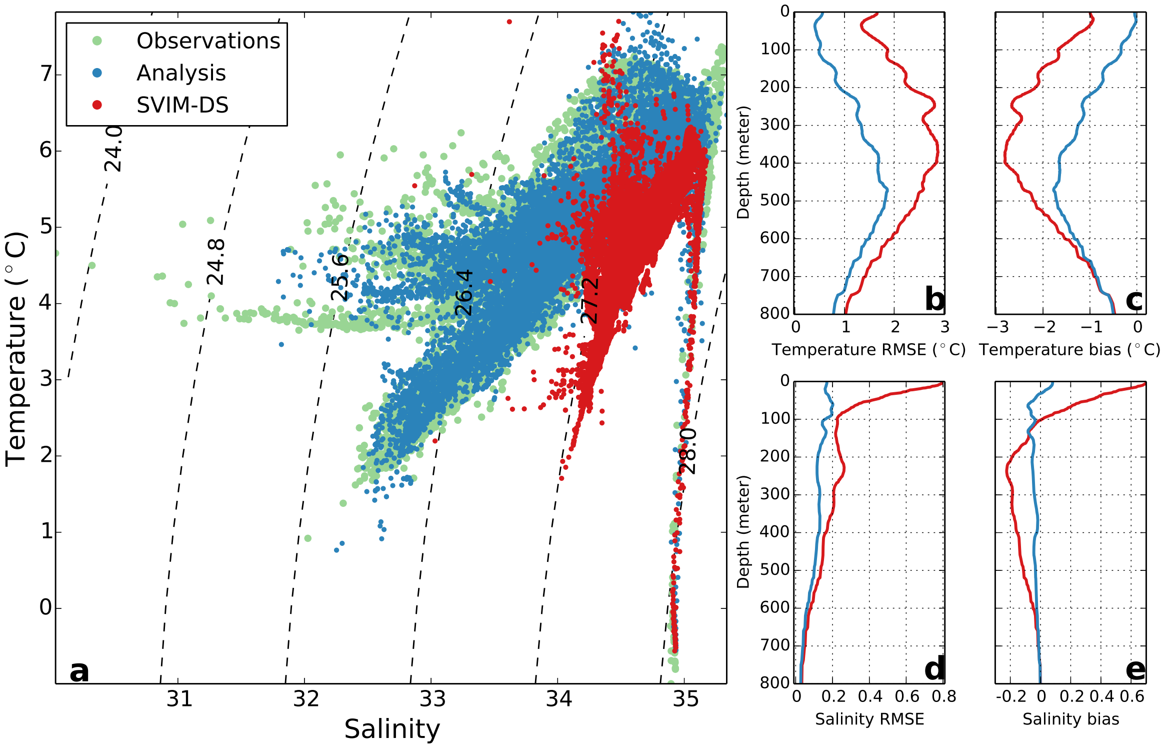

Figure 3. a) TS-diagram showing the water masses in the the observation data set (green), and the corresponding model values for the re-analysis (blue), SVIM-hires (red) and the SVIM archive (orange). The smaller panels at the right show the models's RMSE and bias for temperature (b and c) and salinity (d and e) as a function of depth.

in-situ observations.

4 Impact of state estimation

4.1 Water mass distribution

The two model simulations are compared by evaluating error statistics with respect to the in-situ observations, which to a large extent are taken inside Vestfjorden and on the Lofoten and Vesterålen shelf, and hence mainly in coastal waters. Close to 90% of the observations are taken in the upper 100 meters of the water column, thus the ocean below the mixed layer is poorly sampled. Independent observations are not available since all the in-situ profiles have been used in the reanalysis to provide maximum constraint on the model (e.g. Janeković et al., 2013).

Panel (a) in Fig. 3 shows a T-S diagram of all in-situ observations of temperature and salinity along with the corresponding values from the two model simulations. To aid in the interpretation of the diagram, the panels (b-e) in Fig. 3 show root-mean-square errors (RMSE) and bias for temperature and salinity as a function of depth. The diagram shows that SVIM-DS is too saline and cold, and has much less variation than the observations. SVIM-DS thus resembles the original SVIM hindcast, in which the NCC have a strong positive salinity bias (Lien et al., 2013). In contrast, the cold and saline deep water is well reproduced.

The ANA simulation, on the other hand, has a much better representation of the water masses, demonstrating that the analysis scheme has brought the model much closer to the observations. With the exception of extreme salinity values, the reanalysis is able to reproduce the observed water masses with a realistic variation in density. The salinity bias from SVIM-DS is much reduced at all depths, particularly in the upper 100 m. A negative temperature

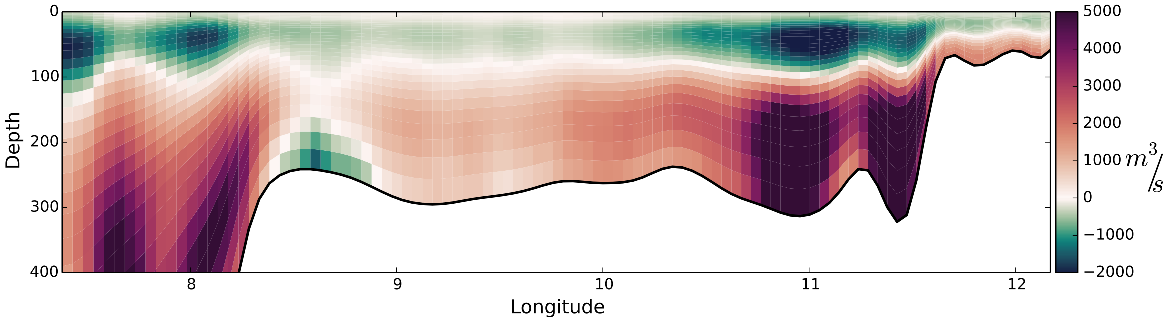

Figure 4. The difference in mean salinity flux through the southern boundary for the period 25 March - 10 April (ANA - SVIM-DS).

bias still persists below the surface layer, but the bias is reduced by approximately 1° C at all depths above 400 m and the RMSE is decreased by a similar magnitude.

It is interesting to note the impact of adjusting the boundary conditions through the analysis scheme. Figure 4 shows the average difference between ANA and SVIM-DS in the salinity flux through the southern boundary during a two week period when in-situ observations are abundant. The salinity flux is here taken as

$$\overline{F_s} = \overline{\oint uS\,\mathrm{d}A}, \tag{1}$$

where u is the normal velocity component at the boundary, S is the salinity, and A is the grid cell area. Most salinity observations are too far away to directly affect the salinity at the boundary given the background error covariances we provide, hence the salinities at the boundary hardly differ between the two simulations. Compared to SVIM-DS, the salinity flux in ANA is decreased in the surface layer and increased in the deeper parts primarily through changes in the velocities at the boundary, and these changes contribute to maintaining a stronger stratification in the reanalysis.

4.2 Baroclinic dynamics

The above comparison between ANA and SVIM-DS demonstrates a significant difference in the stratification, hence we now evaluate the impact of the state estimation on the first baroclinic Rossby radius of deformation, R_1. Since R_1 is the scale at which rotational effects become important, and is closely linked to the scale of boundary currents, fronts, and eddies, any differences between the two simulations are likely to translate into large differences in transport estimates.

The first baroclinic Rossby radius R_1 is defined as

$$R_1 = \frac{c_1}{|f|}, \tag{2}$$

where f is the local Coriolis parameter and c_1 is the phase speed of the first baroclinic mode internal gravity wave. The phase speed can be found as a solution of an eigenvalue problem, but we will use an approximate WKB solution (Chelton et al., 1998). Thus, we use the following relation:

$$R_1 \approx R_1^{WKB} = \frac{1}{|f|\pi}\int_{-H}^{0} N(z)dz, \tag{3}$$

where H is the local water depth and N is the buoyancy frequency. It should be noted that Nurser and Bacon (2014) and Osinski et al. (2010), estimating values of R_1 in the Arctic and Baltic, found the WKB approximation to underestimate R_1, particularly in shallow areas. It is thus likely (and more exact solutions not shown here support this) that the results presented here yield smaller values of R_1 compared to a solution of the full eigenvalue problem.

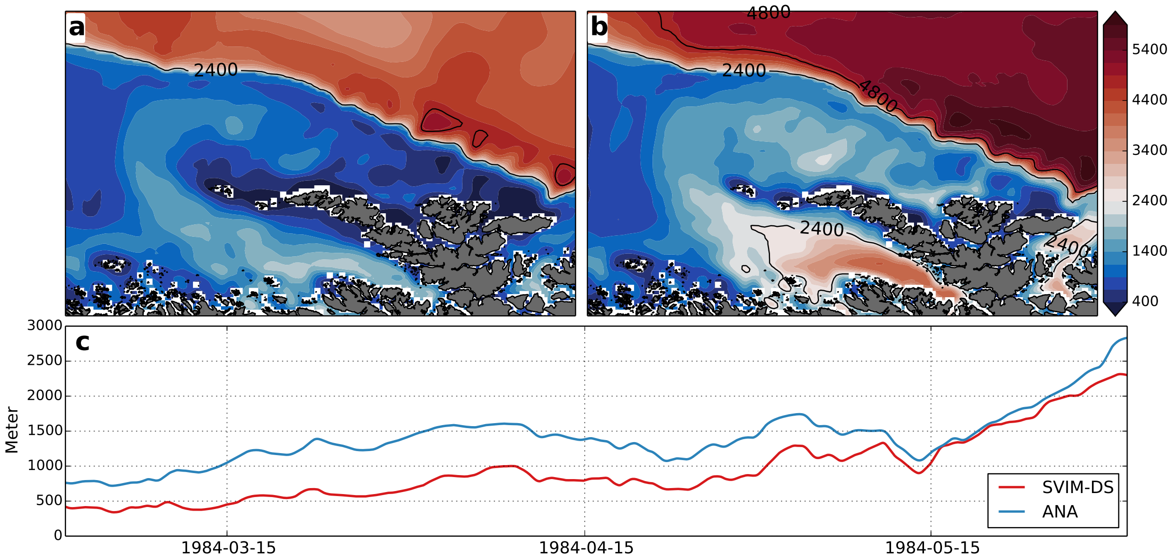

Figure 5. Spring season mean of R_1 for SVIM-DS (a) and ANA (b) with values lower than the horizontal model resolution in blue tones and higher values in reds. c) shows a time series of average on-shelf values of R_1.

The panels (a-b) in Fig. 5 shows the average R_1 over the spring months calculated from the two model simulations. Since the variations of the Coriolis parameter are small in our case, variations in R_1 can primarily be attributed to changes in the depth and the stratification. As a consequence, the shelf break is clearly distinguishable in the results, marking a sharp transition from low to high R_1 values.

For the purposes of this discussion, we define $R_1 > 2\Delta x$ as eddy-resolving and $\Delta x < R_1 < 2\Delta x$ as eddy-permitting, where Δx is the horizontal resolution of our model. It is clear that neither of the simulations are eddy-resolving on the shelf. Over the deep basin, however, ANA is eddy-resolving, while SVIM-DS remains eddy-permitting. ANA also has higher values of R_1 on the shelf, which is particularly evident inside Vestfjorden, where the model now is eddy-permitting, and outside the Lofoten archipelago where the average R_1 values approach the horizontal resolution of the model.

As R_1 depends on the stratification, it exhibits a seasonal cycle. The lowest values are found in March, at the end of the winter season when stratification is weak, and the highest values during summer when there is an increase in runoff due to snow melt and also high insolation. This seasonal cycle seems to be well reproduced by both ANA and SVIM-DS (see Fig. 5c), with a shelf-average (H ¡ 500 m) of R_1 that slowly increases during the spring, before a rapid increase in mid-May caused by snow melt. The shelf average of R_1 is approximately 500 m larger in ANA throughout the period, indicating that the effective model resolution is increased as a result of the state estimation.

4.3 Upper ocean transport

The upper ocean velocities depend on the stratification through the baroclinic response, and in this section statistics of the upper ocean Eulerian and Lagrangian velocities are presented.

Figure 6 shows histograms of Eulerian surface current speeds. The main panel (a) shows histograms based on data from the full model domain and the inlet panels (b-d) show histograms based on data from three sub-domains. For the full model domain, the distributions of surface current speeds differ only slightly between ANA and SVIM-DS. Low current speeds occur more frequently in SVIM-DS, while intermediate speeds (0.3-0.5 ms^{-1}) are more frequent in ANA. SVIM-DS has a slightly higher occurrence of velocities above 0.6 ms^{-1}, probably caused by a stronger degree of topographical steering. While the distributions of ANA and SVIM-DS are rather similar when averaged over the entire model domain, the comparisons between sub-domains reveal some interesting differences. Inside

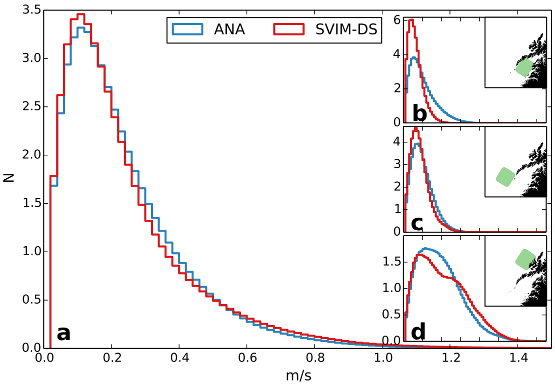

Figure 6. Normalized frequency of occurrence for Eulerian surface current speeds during spring season, obtained from the uppermost model layer that has a thickness of 0.7 m on average. a) For the full model domain. (b-d) For the sub-domains indicated in green. The x-axes have the same range in all panels.

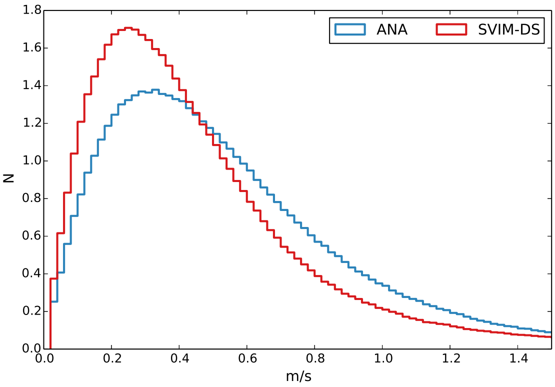

Figure 7. Normalized frequency of occurrence for Lagrangian surface current speed, obtained from artificial model drifters at 1m depth released during spring season.

Vestfjorden (Fig. 6b), the surface currents are much more energetic in the reanalysis ANA. Outside Vesterålen (Fig. 6d), where the shelf is very narrow, SVIM-DS has a tendency toward a bi-modal distribution. The highest speeds are associated with the topographically steered currents along the shelf break, which become more pronounced in SVIM-DS since the surface currents over the deep basins are weak. In ANA, on the other hand, there is no such bi-modality and no clear separation between the currents along the shelf break and over the deep basin.

Lagrangian velocities have been obtained by seeding numerical drifters into the Eulerian velocity fields using the OpenDrift trajectory model (Dagestad et al., 2016; Jones et al., 2016). The drifters were kept at a constant depth of 1 m. A total number of 7680 (288 each third day for 80 days during spring season) numerical drifters were seeded on a uniform grid with 12 km spacing, covering the entire model domain within 30 grid points from the model boundary. Each drifter was active for 256 hours (10.6 days). Drifters that stranded or left the model domain within 10.6 days have been removed from the analysis.

Histograms of the drifter speeds are shown in Fig. 7. The average Lagrangian drift speeds for both ANA and SVIM-DS are higher (0.42 ms^{-1} and 0.35 ms^{-1}, respectively) than their Eulerian counterparts (0.22 ms^{-1} and 0.22 ms^{-1}, respectively, compare with Fig. 6a). Also, the reanalysis ANA has a much higher occurrence of high Lagrangian drift speeds than SVIM-DS, despite the fact that ANA and SVIM-DS have similar distributions for the

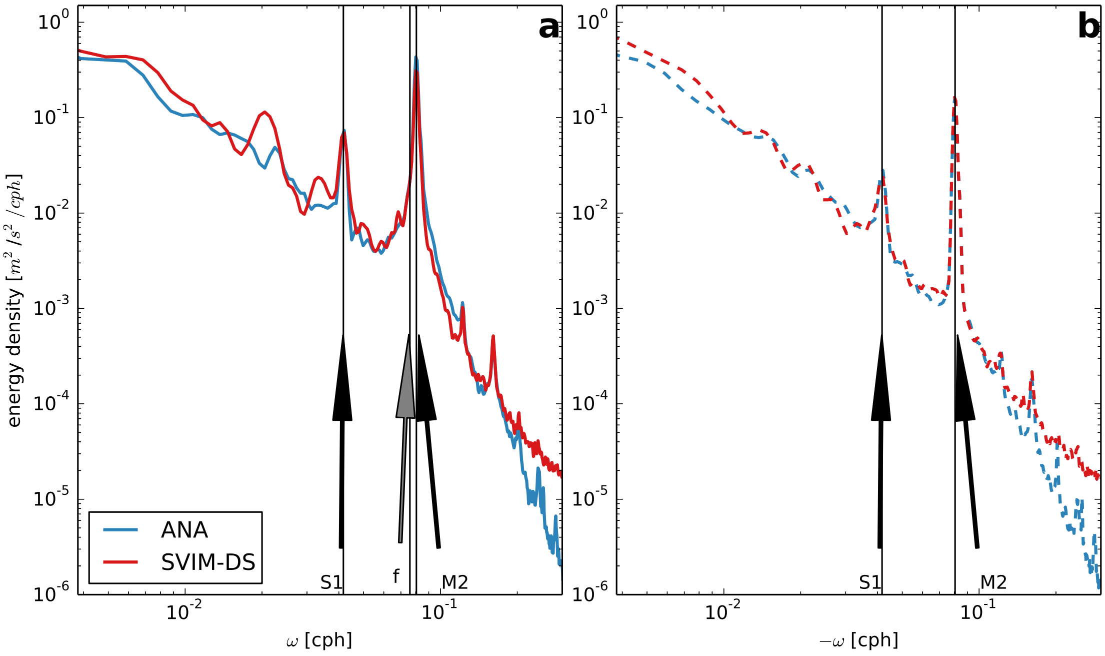

Figure 8. Rotary Spectra of Eulerian surface currents. a) anti-cyclonic rotary components and b) cyclonic rotary components. The vertical bars indicate the solar tide S1, inertial period f, and lunar tide M2.

Eulerian speeds.

To further investigate the differences between Eulerian and Lagrangian velocities, rotary spectra from both data sets have been calculated. To obtain the Eulerian rotary spectra, hourly surface velocity fields were divided into 512 hour long segments, using every tenth grid point to provide some degree of de-correlation between the segments. The rotary spectra for each segment was calculated following Gonella (1972), and all the segments were averaged. Figure 8a shows the energy levels of the negative frequency components, which represent anti-cyclonic motion. SVIM-DS and ANA have approximately the same level of energy at most frequencies, with distinct peaks near the inertial frequency and at the M2 tidal frequency. Figure 8b shows the energy levels of the positive frequency components that represent cyclonic motion. The sharp peak around the M2 frequency is the most dominant feature. SVIM-DS and ANA again have similar energy levels at most frequencies. At higher frequencies (near the Nyquist frequency), the SVIM-DS model is more energetic than ANA in both the negative and positive component spectra. It is not clear to us what is causing this difference, but we speculate whether it can be attributed to the suppression of numerical instabilities being slightly different in the two simulations.

Lagrangian rotary spectra were calculated from the velocities of the numerical drifters, using the methodology in Röhrs and Christensen (2015). Each drifter trajectory has a sampling frequency of 0.5 h and a duration of 256 h. The spectra for each segment are averaged to provide the Lagrangian rotary spectra shown in Fig. 9a. The spectra compare well with the results obtained for observed drifters in Röhrs and Christensen (2015), indicating a realistic representation of upper ocean currents in the model simulations. We note that the Lagrangian energy levels are higher for ANA than for SVIM-DS, although this is not the case for the Eulerian rotary spectra. Figure 9b shows the ratio between the SVIM-DS and ANA energy levels for the positive and negative frequencies, respectively. The differences are highest in the sub-inertial frequency band where ANA is up to twice as energetic as SVIM-DS, indicating that ANA has more near-inertial oscillations, which is likely to be caused by the fact that the more pronounced stratification in ANA should allow for more intense near-surface response to wind forcing, as discussed in Röhrs and Christensen (2015).

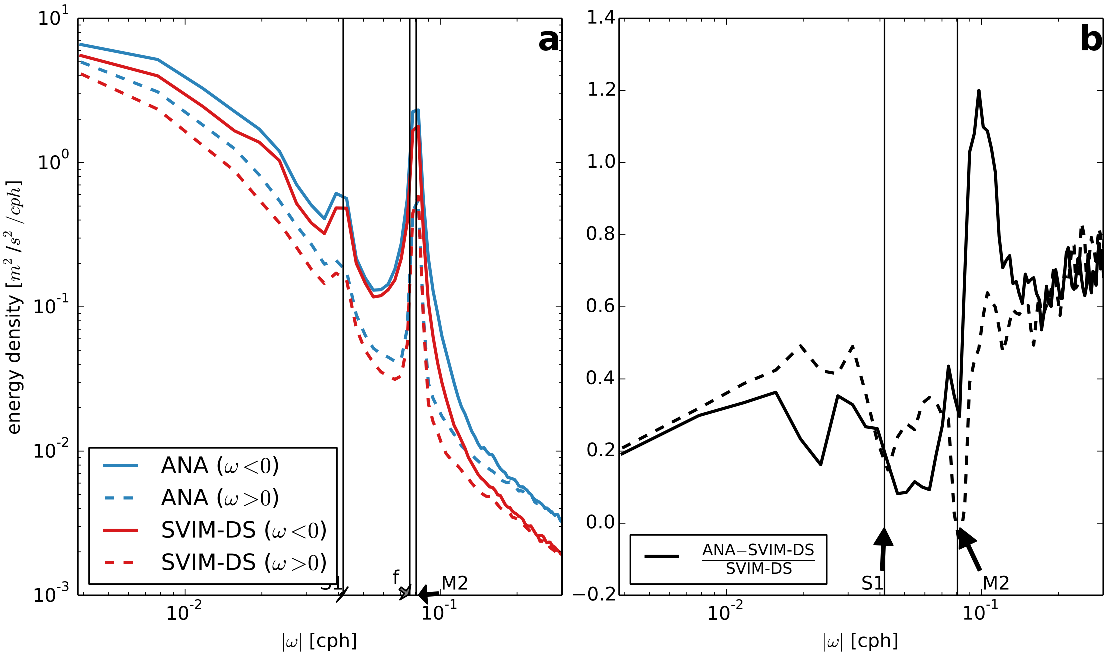

Figure 9. a) Rotary spectra of Lagrangian surface currents, obtained from the trajectories of artificial model drifters. Anti-cyclonic rotary components are shown using solid lines and cyclonic rotary components using dashed lines. b) Difference of rotary components between ANA and SVIM-DS model runs, normalized by SVIM-DS rotary components.

5 Discussion and concluding remarks

In this study we have compared a downscaled version of the hindcast archive SVIM with a data assimilative equivalent, both simulating the circulation in the Lofoten/Vesterålen area during the spring of 1984. The SVIM archive has previously been used to study plankton transport and connectivity, but biases in the modeled salinity and temperature are likely to have influenced the results. The assimilation of satellite SST and in-situ salinity and temperature brings the reanalysis much closer to the observations, and the distribution of water masses becomes more realistic. It is clear that including the boundary conditions in the control variable vector is beneficial. In our case part of the salinity bias in the interior of the model domain is removed through adjustment of the depth dependent velocities at the southern boundary.

There are still biases in the reanalysis, in particular a cold bias in the deeper layers, but the reductions are significant in the upper part of the ocean. A recommendation for future research cruises is therefore to collect more hydrography profiles that extend to the bottom. The internal deformation radius (first baroclinic mode) is generally higher in the reanalysis compared to the downscaled hindcast. This increase results in a higher effective resolution in the reanalysis, and is a direct consequence of the improved representation of the stratification. The estimates of the deformation radius indicate, however, that the horizontal resolution of 2.4 km that we have used is too coarse to properly resolve baroclinic instabilities.

The distributions of the Eulerian speeds in the two model simulations are similar, with some local differences that point to the impact of assimilation on the model hydrography. For instance, inside Vestfjorden the speed distribution of the reanalysis is wider, indicating that the currents have become more variable and responsive to the local wind forcing. On the shelf, the downscaled hindcast has a bi-modal distribution, with the higher speeds dominated by the strong topographically trapped flow along the shelf break. The reanalysis shows no such tendency toward a bi-modal distribution, which again indicates that the currents have become more variable and less dependent on model bathymetry.

We find distinct differences between the reanalysis and the downscaled hindcast when we investigate the energy spectra of Lagrangian drift currents. The energy levels of the reanalysis are generally larger for all frequencies. The differences are particularly large in the sub-inertial frequency band for the anti-cyclonic drift velocity components, which indicates a different response to the wind forcing and more near-inertial oscillations in the upper layers. Our analysis does not reveal why the Lagrangian energy levels are higher in the reanalysis, but there are two possible explanations: (i) the differences in the upper ocean dynamics leads to more clustering, and convergence of numerical drifters in regions of strong divergence (Jacobs et al., 2016), and/or (ii) the increase in periodic flow features (cf. the increase in the sub-inertial frequency band) leads to an increase in the residual drift currents (Longuet-Higgins, 1969; Wei et al., 2004). A detailed analysis of this issue is outside the scope of the present paper, but will be the focus of future investigations.

In this study we have used numerical drifters at a fixed depth of 1 meter, thus only evaluating the impact of improved stratification on the currents. For the case of transport of buoyant particles, such as cod eggs and oil droplets, the effect may be even more profound as the particles are likely to have different vertical distributions in the two simulations as a consequence of density differences and its effect on mixing.

Acknowledgments
The model results will be provided upon request to the corresponding author. The NORA10 data used here are available on request to the Norwegian Meteorological Institute, while the SVIM archive is available at ftp://ftp.met.no/projects/SVIM-public/.

We gratefully acknowledge financial support from the Research Council of Norway through grants 244262 (RETROSPECT) and 237906 (CIRFA). This research was also supported with computational resources provided by NOTUR (project NN9197K). We would also like to thank Prof. Svein Sundby and Dr. Frode Vikebø (IMR, Norway), Prof. Johnny Johannessen (NERSC, Norway), and Prof. Andrew Moore (UCSC, USA) for stimulating and fruitful discussions.

References

Ådlandsvik, B., and S. Sundby, 1994: Modelling the transport of cod larvae from the Lofoten area. *ICES Marine Science Symposia*, Vol. 198, 379–392.

Beldring, S., K. Engeland, L. A. Roald, N. R. Sælthun, and A. Voksø, 2001: Estimation of parameters in a distributed precipitation-runoff model for Norway. *Hydrol. Earth Syst. Sci.*, **7 (3)**, 304–316, doi:10.5194/hess-7-304-2003.

Chapman, D. C., 1985: Numerical Treatment of Cross-Shelf Open Boundaries in a Barotropic Coastal Ocean Model. *J. Phys. Oceanogr.*, **15 (8)**, 1060–1075, doi:10.1175/1520-0485(1985)015⟨1060:NTOCSO⟩2.0.CO;2.

Chelton, D. B., R. A. deSzoeke, M. G. Schlax, K. El Naggar, and N. Siwertz, 1998: Geographical Variability of the First Baroclinic Rossby Radius of Deformation. *J. Phys. Oceanogr.*, **28 (3)**, 433–460, doi:10.1175/1520-0485(1998)028⟨0433:GVOTFB⟩2.0.CO;2.

Dagestad, K.-F., J. Röhrs, Ø. Breivik, and B. Ådlandsvik, 2016: Opendrift: A generic framework for trajectory modeling. *in preparation*.

De Hoop, L., O. J. Broch, A. J. Hendriks, and F. De Laender, 2016: Crude oil affecting the biomass of the marine copepod Calanus finmarchicus: Comparing a simple and complex population model. *Mar. Environ. Res.*, **119**, 197–206, doi:10.1016/j.marenvres.2016.06.008.

Drivdal, M., G. Broström, and K. H. Christensen, 2014: Wave-induced mixing and transport of buoyant particles: application to the Statfjord A oil spill. *Ocean Sci.*, **10 (6)**, 977–991, doi:10.5194/os-10-977-2014.

Egbert, G. D., and S. Y. Erofeeva, 2002: Efficient Inverse Modeling of Barotropic Ocean Tides. *J. Atmos. Oceanic Technol.*, **19 (2)**, 183–204, doi:10.1175/1520-0426(2002)019⟨0183:EIMOBO⟩2.0.CO;2.

Eide, M. S., Ø. Endresen, Ø. Breivik, O. W. Brude, I. H. Ellingsen, K. Røang, J. Hauge, and P. O. Brett, 2007: Prevention of oil spill from shipping by modelling of dynamic risk. *Mar. Pollut. Bull.*, **54 (10)**, 1619–1633, doi:10.1016/j.marpolbul.2007.06.013.

Ellertsen, B., G. Furnes, P. Solemdal, and S. Sundby, 1981: Effects of upwelling on the distribution of cod eggs and zooplankton in Vestfjorden. *Proc. from Norwegian Coastal Current Symposium, Geilo, Norway, 9–12 September 1980 (Eds: R. Sætre and M. Mork.) University of Bergen, 1981: 604–628.*

Flather, R. A., 1976: A tidal model of the north-west european continental shelf. *Mem. Soc. R. Sci. Liege*, **10 (6)**, 141–164.

Furnes, G., and S. Sundby, 1981: Upwelling and wind induced circulation in vestfjorden. *Proc. from Norwegian Coastal Current Symposium, Geilo, Norway, 9–12 September 1980 (Eds: R. Sætre and M. Mork). University of Bergen 1981: 152–178.*

Gonella, J., 1972: A rotary-component method for analysing meteorological and oceanographic vector time series. *Deep-Sea Res.*, **19 (12)**, 883–846.

Good, S. A., M. J. Martin, and N. A. Rayner, 2013: EN4: Quality controlled ocean temperature and salinity profiles and monthly objective analyses with uncertainty estimates. *J. Geophys. Res. C: Oceans*, **118 (12)**, 6704–6716, doi:10.1002/2013JC009067.

Haidvogel, D. B., and Coauthors, 2008: Ocean forecasting in terrain-following coordinates: Formulation and skill assessment of the Regional Ocean Modeling System. *J. Comput. Phys.*, **227 (7)**, doi:10.1016/j.jcp.2007.06.016.

Høyer, J. L., and J. She, 2007: Optimal interpolation of sea surface temperature for the North Sea and Baltic Sea. *J. Mar. Syst.*, **65**, 176–189, doi:10.1016/j.jmarsys.2005.03.008.

Isachsen, P. E., 2015: Baroclinic instability and the mesoscale eddy field around the Lofoten Basin. *J. Geophys. Res. C: Oceans*, **120 (4)**, 2884–2903, doi:10.1002/2014JC010448.

Jacobs, G. A., H. S. Huntley, A. D. Kirwan, B. L. Lipphardt, T. Campbell, T. Smith, K. Edwards, and B. Bartels, 2016: Ocean processes underlying surface clustering: PROCESSES UNDERLYING SURFACE CLUSTERING. *J. Geophys. Res. C: Oceans*, **121 (1)**, 180–197, doi:10.1002/2015JC011140.

Janeković, I., B. S. Powell, D. Matthews, M. A. McManus, and J. Sevadjian, 2013: 4d-Var data assimilation in a nested, coastal ocean model: A Hawaiian case study: 4D-VAR IN NESTED MODEL. *J. Geophys. Res. C: Oceans*, **118 (10)**, 5022–5035, doi:10.1002/jgrc.20389.

Jones, C. E., and Coauthors, 2016: Measurement and modeling of oil slick transport. *J. Geophys. Res. C: Oceans*, **121 (10)**, 7759–7775.

Kvile, K. Ø., Ø. Langangen, I. Prokopchuk, N. C. Stenseth, and L. C. Stige, 2016: Disentangling the mechanisms behind climate effects on zooplankton. *Proc. Natl. Acad. Sci. U.S.A.*, **113 (7)**, 1841–1846, doi:10.1073/pnas.1525130113.

Langangen, Ø., G. Ottersen, L. Ciannelli, F. B. Vikebø, and L. C. Stige, 2016: Reproductive strategy of a migratory fish stock: implications of spatial variations in natural mortality. *Can. J. Fish. Aquat. Sci.*, 1–8, doi:10.1139/cjfas-2015-0321, URL http://www.nrcresearchpress.com/doi/abs/10.1139/cjfas-2015-0321.

Lien, V. S., Y. Gusdal, J. Albretsen, A. Melsom, and F. B. Vikebø, 2013: Evaluation of a Nordic Seas 4 km numerical ocean model hindcast archive (SVIM), 1960–2011. *Fisken og Havet*, 7–79.

Lien, V. S., Y. Gusdal, and F. B. Vikebø, 2014: Along-shelf hydrographic anomalies in the Nordic Seas (1960–2011): locally generated or advective signals? *Ocean Dyn.*, **64 (7)**, 1047–1059, doi:10.1007/s10236-014-0736-3.

Longuet-Higgins, M. S., 1969: On the transport of mass by time-varying ocean currents. *Deep Sea Res.*, **16 (5)**, 431–447, doi:10.1016/0011-7471(69)90031-X.

Marchesiello, P., J. C. McWilliams, and A. Shchepetkin, 2001: Open boundary conditions for long-term integration of regional oceanic models. *Ocean Modell.*, **3**, 1–20, doi:10.1016/S1463-5003(00)00013-5.

Moore, A. M., H. G. Arango, G. Broquet, B. S. Powell, A. T. Weaver, and J. Zavala-Garay, 2011a: The Regional Ocean Modeling System (ROMS) 4-dimensional variational data assimilation systems: Part I - System overview and formulation. *Prog. Oceanogr.*, **91 (1)**, 34–49, doi:10.1016/j.pocean.2011.05.004.

Moore, A. M., H. G. Arango, E. Di Lorenzo, B. D. Cornuelle, A. J. Miller, and D. J. Neilson, 2004: A comprehensive ocean prediction and analysis system based on the tangent linear and adjoint of a regional ocean model. *Ocean Modell.*, **7**, 227–258, doi:10.1016/j.ocemod.2003.11.001.

Moore, A. M., and Coauthors, 2011b: The Regional Ocean Modeling System (ROMS) 4-dimensional variational data assimilation systems: Part II - Performance and application to the California Current System. *Prog. Oceanogr.*, **91 (1)**, 50–73, doi:10.1016/j.pocean.2011.05.003.

Moore, A. M., and Coauthors, 2011c: The Regional Ocean Modeling System (ROMS) 4-dimensional variational data assimilation systems: Part III - Observation impact and observation sensitivity in the California Current System. *Prog. Oceanogr.*, **91 (1)**, 74–94, doi:10.1016/j.pocean.2011.05.005.

Myksvoll, M. S., K.-M. Jung, J. Albretsen, and S. Sundby, 2014: Modelling dispersal of eggs and quantifying connectivity among Norwegian coastal cod subpopulations. *ICES J. Mar. Sci.*, **71 (4)**, 957–969, doi:10.1093/icesjms/fst022.

Nurser, A. J. G., and S. Bacon, 2014: The Rossby radius in the Arctic Ocean. *Ocean Sci.*, **10 (6)**, 967–975, doi:10.5194/os-10-967-2014.

Osinski, R., D. Rak, W. Walczowski, and J. Piechura, 2010: Baroclinic rossby radius of deformation in the southern baltic sea. *Oceanologia*, **52 (3)**, 417–429.

Ourmières, Y., J.-M. Brankart, L. Berline, P. Brasseur, and J. Verron, 2006: Incremental Analysis Update Implementation into a Sequential Ocean Data Assimilation System. *J. Atmos. Oceanic Technol.*, **23 (12)**, 1729–1744, doi:10.1175/JTECH1947.1.

Poulain, P.-M., A. Warn-Varnas, and P. P. Niiler, 1996: Near-surface circulation of the Nordic seas as measured by Lagrangian drifters. *J. Geophys. Res. C: Oceans*, **101 (C8)**, doi:10.1029/96JC00506.

Reistad, M., Ø. Breivik, H. Haakenstad, O. J. Aarnes, B. R. Furevik, and J.-R. Bidlot, 2011: A high-resolution hindcast of wind and waves for the North Sea, the Norwegian Sea, and the Barents Sea. *J. Geophys. Res. C: Oceans*, **116 (C5)**, doi:10.1029/2010JC006402.

Reynolds, R. W., T. M. Smith, C. Liu, D. B. Chelton, K. S. Casey, and M. G. Schlax, 2007: Daily High-Resolution-Blended Analyses for Sea Surface Temperature. *J. Clim.*, **20 (22)**, 5473–5496, doi:10.1175/2007JCLI1824.1.

Röhrs, J., and K. H. Christensen, 2015: Drift in the uppermost part of the ocean. *Geophys. Res. Lett.*, **42 (23)**, 2015GL066 733, doi:10.1002/2015GL066733.

Röhrs, J., K. H. Christensen, F. Vikebø, S. Sundby, Ø. Sætra, and G. Broström, 2014: Wave-induced transport and vertical mixing of pelagic eggs and larvae. *Limnol. Oceanogr.*, **59 (4)**, 1213–1227, doi:10.4319/lo.2014.59.4.1213.

Shchepetkin, A. F., and J. C. McWilliams, 2005: The regional oceanic modeling system (ROMS): a split-explicit, free-surface, topography-following-coordinate oceanic model. *Ocean Modell.*, **9 (4)**, 347–404, doi:10.1016/j.ocemod.2004.08.002.

Sperrevik, A. K., K. H. Christensen, and J. Röhrs, 2015: Constraining energetic slope currents through assimilation of high-frequency radar observations. *Ocean Sci.*, **11 (2)**, 237–249, doi:10.5194/os-11-237-2015.

Stige, L. C., Ø. Langangen, N. A. Yaragina, F. B. Vikebø, B. Bogstad, G. Ottersen, N. C. Stenseth, and D. Ø. Hjermann, 2015: Combined statistical and mechanistic modelling suggests food and temperature effects on survival of early life stages of Northeast Arctic cod (Gadus morhua). *Prog. Oceanogr.*, **134**, 138–151, doi:10.1016/j.pocean.2015.01.009.

Sundby, S., and P. Bratland, 1987: Kartlegging av gytefeltene for norsk-arktisk torsk i Nord-Norge og beregning av eggproduksjonen i årene 1983-1985. *Fisken og Havet*, **1**, 1–58, URL http://brage.bibsys.no/xmlui/handle/11250/112859.

Svendsen, E., and Coauthors, 2007: An ecosystem modeling approach to predicting cod recruitment. *Deep Sea Res. Part II*, **54**, 2810–2821, doi:10.1016/j.dsr2.2007.07.033.

Vikebø, F., C. Jørgensen, T. Kristiansen, and Ø. Fiksen, 2007: Drift, growth, and survival of larval Northeast Arctic cod with simple rules of behaviour. *Mar. Ecol. Prog. Ser.*, **347**, 207–219, doi:10.3354/meps06979.

Vikebø, F. B., P. Rønningen, V. S. Lien, S. Meier, M. Reed, B. Ådlandsvik, and T. Kristiansen, 2013: Spatio-temporal overlap of oil spills and early life stages of fish. *ICES J. Mar. Sci.*, doi:10.1093/icesjms/fst131.

Volkov, D. L., A. A. Kubryakov, and R. Lumpkin, 2015: Formation and variability of the Lofoten basin vortex in a high-resolution ocean model. *Deep Sea Res. Part I*, **105**, 142–157, doi:10.1016/j.dsr.2015.09.001, URL http://www.sciencedirect.com/science/article/pii/S0967063715001508.

Warner, T. T., R. A. Peterson, and R. E. Treadon, 1997: A Tutorial on Lateral Boundary Conditions as a Basic and Potentially Serious Limitation to Regional Numerical Weather Prediction. *Bull. Am. Meteorol. Soc.*, **78**, 2599–2617, doi:10.1175/1520-0477(1997)078⟨2599:ATOLBC⟩2.0.CO;2.

Wei, H., D. Hainbucher, T. Pohlmann, S. Feng, and J. Suendermann, 2004: Tidal-induced Lagrangian and Eulerian mean circulation in the Bohai Sea. *J. Mar. Syst.*, **44 (3-4)**, 141–151, doi:10.1016/j.jmarsys.2003.09.007.

Paper IV

5.4 On the variability in the onset of the Norwegian Coastal Current

Kai Håkon Christensen, Ann Kristin Sperrevik, and Göran Broström

manuscript

On the variability in the onset of the Norwegian Coastal Current

Kai Håkon Christensen[1,2], **Ann Kristin Sperrevik**[1], **and Göran Broström**[3,1]

[1]Norwegian Meteorological Institute, Oslo, Norway
[2]University of Oslo, Oslo, Norway
[3]University of Gothenburg, Gothenburg, Sweden

Abstract

A high resolution reanalysis of the circulation in the Kattegat and Skagerrak is used to investigate the mechanisms that control the variability in the onset of the Norwegian Coastal Current. In the reanalysis, we have used all available in-situ and remote sensing observations of salinity and temperature, in addition we use surface current observations from two coastal high frequency radars that were ideally placed to monitor the exchange between the two basins. We find a strong correlation between the variability in the wind forcing in the Skagerrak and the transport in the Norwegian Coastal Current through the Torungen-Hirtshals section. Two cases with winds into and out of the Skagerrak are studied in more detail, and the results suggest asymmetries in the forcing mechanisms. For winds out of the Skagerrak, strong outflows of Baltic Sea water associated with a deflection of the Kattegat-Skagerrak front may disrupt local processes in the Skagerrak, which is not accounted for in previously published conceptual models for the variability of the coastal currents in this region.

1 Introduction

The Kattegat and the Skagerrak connect the Baltic Sea and the North Sea. Here three water masses meet: Baltic Sea water coming through the sounds in the south, North Sea water carried with the Jutland current along the Danish west coast, and subsurface Atlantic water branching off the Atlantic Current north of Scotland and flowing south along the coast of Norway (see Fig. 1). The Jutland and Baltic currents converge outside the northern tip of Denmark, Skagen, forming the Kattegat-Skagerrak front.

The ship traffic in the region is heavy, with approximately 40,000-60,000 larger vessels passing through every year, and major oil spills in recent years have been caused by groundings or ship collisions (e.g. Broström et al., 2011). There are hundreds of shipwrecks in the region, containing bunker oil, mustard gas, white phosphorous and other hazardous loads, and leakage of toxic material from sunken vessels poses another environmental hazard. In addition, there are hundreds of thousands of pleasure crafts in the region, the use of which peaks strongly in the summer months. Operational circulation models are thus needed both for ship routing, oil spill drift models, and for search-and-rescue support. The circulation in the Kattegat-Skagerrak is challenging to model, however, and multi-model ensembles show large differences between modeling systems (Golbeck et al., 2015).

Of particular interest is the onset of the Norwegian Coastal Current (NCC), since the NCC influences the environmental conditions along the entire Norwegian coast. The NCC originates in the Skagerrak as a continuation of the Baltic Sea outflow and it flows along the Norwegian coast all the way up into the Barents Sea. It carries freshwater from the Baltic Sea and the Norwegian rivers into the Arctic and hence plays an important role in the Arctic freshwater budget. Along most of the Norwegian coast, the cold and fresh NCC is wedged between the warm and saline Norwegian Atlantic Current and the coast, and mixing between the Atlantic and coastal waters gradually reduce the contrast between the two water masses as they flow northward. Typical current speeds in the NCC are about 0.25 ms^{-1}, but occasionally exceed 1 ms^{-1} (Aure et al., 2007). There is a seasonal variation in the NCC: in the summer it is wide and shallow, while in the winter it turns narrow and deep. From a climate perspective there is a trend towards increasing temperatures in the NCC of the order of 1° C (Albretsen et al., 2012).

In this paper we use a reanalysis of the Kattegat-Skagerrak circulation to investigate the variability in the onset of the NCC, and the causes for this variability. Our focus is on the response to the large scale wind forcing in

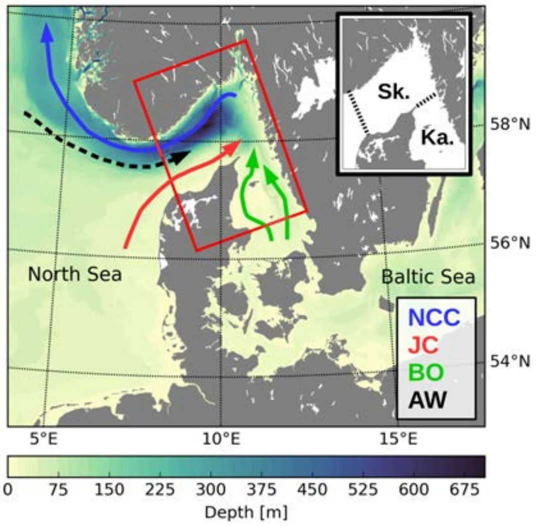

Figure 1. The map shows the lateral boundaries of the model (red) as well as the main currents in the Kattegat-Skagerrak system: the Norwegian Coastal Current (NCC, blue), the Jutland Current (JC, red), the Baltic outflow (BO, green), and the Dooley Current with Atlantic water (AW, black). The inset shows the approximate boundaries of the Kattegat and the Skagerrak.

the Skagerrak, which is associated with Ekman transport across the Skagerrak, and upwelling and downwelling along the Norwegian and Danish coasts. We use the four-dimensional variational analysis scheme in the Regional Ocean Modeling System, assimilating satellite sea surface temperature and in-situ salinity and temperature from a variety of sources. The observations also include data from two high frequency (HF) coastal radars that were temporarily deployed just north of the Kattegat-Skagerrak front, hence providing an excellent constraint on the exchange between the two basins. Previous observation and modeling studies have focused on integrated parameters such as freshwater height and available potential energy, linking these quantities to the circulation (e.g. Gustafsson and Stigebrandt, 1996; Røed and Albretsen, 2007). We do not rely on such integrated parameters to estimate the currents as these are taken directly from the model, although we use the freshwater height to investigate the time development of the surface layer for different surface forcing conditions.

The outline of the paper is as follows: In Sec. 2 we briefly describe the main features of the circulation in the Kattegat-Skagerrak; in Sec. 3 we describe the modeling system and the observations that we use to produce our reanalysis; in Sec. 4 we present the results from the reanalysis, focusing on the components of the overall circulation that have a major influence on the NCC. Finally, Sec. 5 contains a discussion and some concluding remarks.

2 The circulation in the Kattegat-Skagerrak

The Kattegat and Skagerrak basins are mostly shallow, with the exception of the Norwegian Trench, which extends from the Norwegian Sea and follows the coastline into the Skagerrak (Fig. 1). The northern part of the Skagerrak is therefore the deepest, with a maximum depth of 710 m. The southern part toward Denmark is much more shallow, with depths decreasing slowly from about 50 m in the central part of the basin to the sandy northern coastline of Denmark. The Norwegian Trench continues as the Deep Trench into the Kattegat along the Swedish coast, with depths slowly decreasing from about 100 m in northern Kattegat to the Belt Sea and Öresund in the south. Here the Kattegat connects to the Baltic Sea through narrow straits and the main flows are over the Darss Sill (18 m) and the Drogden Sill (8 m). The tides are dominated by the semi-diurnal component, and the tidal range is small in both basins (typical offshore range is 5-10 cm). The largest rivers that flow into the Kattegat and Skagerrak are Glomma, Drammenselva and Göta Älv (see Fig. 2), with average discharges in the years 2014-2015 of 853, 448 and

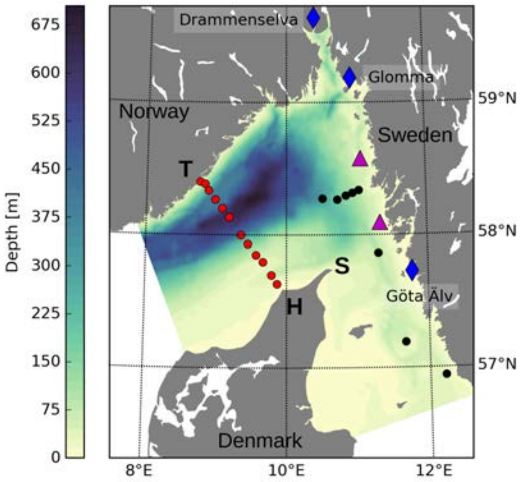

Figure 2. The map shows the location of the three largest rivers Glomma, Göta Älv and Drammenselva (diamonds). Also shown are the locations of the two HF radars at Måseskär (southernmost) and Väderöarna (triangles). The range of these HF radars were approximately equivalent to the distance from the Swedish coast to the tip of Denmark, at Skagen (S). The black dots show hydrographic stations that are part of regular Swedish monitoring cruises while the red dots show the stations on the Torungen-Hirtshals section.

604 m^3s^{-1}, respectively (data from the national hydrological services).

The outflow from the Baltic Sea has been shown to correlate well with large scale gradients in mean sea level pressure (Stigebrandt, 1983), but is out of phase with the freshwater supply to the Baltic Sea (Aure et al., 2007). The response to the weather systems can be very strong in the Danish straits, with barotropic flows exceeding the freshwater flow out of the Baltic Sea by one order of magnitude (Stigebrandt, 1983). The Kattegat is well represented as a two-layer system, with the surface layer increasing in salinity from about 10-12 in the south to about 20-25 toward the Kattegat-Skagerrak front, and below the surface layer we find Skagerrak water with salinities between 30-35 (e.g., Gustafsson, 1997; Jakobsen, 1997; Stigebrandt, 1983). The overall circulation in the surface layer is anticyclonic with variations due to changes in the Baltic outflow and the position of the Kattegat-Skagerrak front (McClimans et al., 2000; Nielsen, 2005; Stigebrandt, 1987).

In the Skagerrak the surface circulation is primarily cyclonic, and the sea surface height has its minimum in the central part of the basin. The NCC flows westward out of the Skagerrak on the northern side while the Jutland current (JC) brings North Sea water influenced by the discharge from major rivers in the southern part of the North Sea (i.e., the Rhine, the Meuse and the Elbe). The so-called Dooley Current (Dooley, 1974) brings Atlantic water in from the Northern North Sea along the southern rim of the Norwegian Trench, and this water forms the bottom layer. The surface layer is thinnest in the central part of the Skagerrak where the Atlantic water often can be found at 10-20 m depth (e.g., Gustafsson and Stigebrandt, 1996). There is a seasonal variability in freshwater height in the Skagerrak, which on average is related to the seasonal variability in the Baltic Sea outflow (Aure et al., 2007; Gustafsson and Stigebrandt, 1996). The response to local wind forcing is complex and Ekman transport across the central part of the Skagerrak contributes to exchange between the NCC and the JC, and also influences the exchange between the Skagerrak and the Kattegat (e.g., Danielssen et al., 1997).

The transport out of the Kattegat and into the Skagerrak has been estimated to be between 45,000-80,000 m^3s^{-1}, and the average outflow from the Skagerrak in the NCC has been estimated to 400,000 m^3s^{-1} (Gustafsson, 1997). The difference between these two transports is due to the JC and the Dooley Current (see Fig. 1). Thus, the Baltic Sea outflow is only a small part of the total transport in the NCC and there is considerable mixing of the various water masses in the Skagerrak. Extensive field campaigns were launched in 1990-91 (SKAGEX, see e.g. Berntsen and Svendsen, 1999, and references therein), which provided near synoptic hydrographic data for extended periods. Analysis of the SKAGEX data set has indicated that the coastal currents are strongly correlated with the local wind forcing, with a response time of about one week (Gustafsson, 1999). This response time is consistent with a baroclinic signal propagating with a speed of about 1 ms^{-1} around the rim of the Skagerrak basin.

3 Methods

3.1 Ocean circulation model

We use the Regional Ocean Modeling System (ROMS), which is a primitive equation model with split-explicit time stepping, and that uses topography-following vertical coordinates (Shchepetkin and McWilliams, 2005, 2009). The model domain is indicated in Fig. 1. The horizontal resolution is approximately 1 km and we use 50 vertical layers. The minimum depth in the model is set to 10 m. The quadratic bottom friction coefficient is increased in shallow areas both for reasons of numerical stability and also to reduce the flow in the regions where the actual depth is less than the model minimum depth. Vertical mixing is parameterized using the two-equation k-ω scheme (Umlauf et al., 2003; Warner et al., 2005), with surface wave breaking as a source of turbulent kinetic energy parameterized as in Craig and Banner (1994). The model has been spun up from Jan. 1, 2014, with four-dimensional variational (4D-Var) data assimilation from Sep. 1, 2014. We show results here for the period Oct. 1, 2014 to Nov. 30, 2015.

The model is forced with hourly data from the numerical weather prediction model AROME-MetCoOp of the Norwegian Meteorological Institute and the Swedish Hydrological and Meteorological Institute (SMHI). This model has a horizontal resolution of 2.5 km. Surface fluxes are obtained via the COARE 3.0 bulk flux algorithms (Fairall et al., 2003) that are built into ROMS. The lateral boundary conditions are obtained from the operational Baltic and Northwest Shelf ocean model components of the Copernicus Marine Environment Monitoring Service (see http://marine.copernicus.eu, the data streams are BALTICSEA_ANALYSIS_FORECAST_PHYS_003_006-TDS and NORTHWESTSHELF_ANALYSIS_FORECAST_PHYS_004_001_b, respectively). These model fields are averaged to provide daily inputs, interpolated to our native model grid to provide model values in boundary relaxation zones towards the North Sea and the Baltic Sea, respectively. The matching to exterior values is implemented as in Marchesiello et al. (2001) with a mixture of nudging and radiation conditions. The model is also forced with 7 tidal components from the TPXO global inverse barotropic model (Egbert and Erofeeva, 2002). Freshwater discharge from 38 rivers are provided as daily climatological values, except for the three largest rivers (Glomma, Drammenselva and Göta Älv) for which we provide daily averages obtained from Norwegian and Swedish authorities.

3.2 Analysis scheme

We use the 4D-Var analysis scheme implemented in ROMS (ROMS-4DVAR, Moore et al., 2011a,b,c). More specifically, we use the physical-space statistical analysis system (PSAS) with the restricted preconditioned conjugate gradient (RPCG) algorithm of Gratton and Tshimanga (2009) and a 24 h assimilation window. It is possible to include the surface fluxes and the lateral boundary conditions in the control variable vector of ROMS-4DVAR, and this has been done here. The background error variances needed for ROMS-4DVAR are estimates obtained from the intrinsic model variability from a model hindcast (e.g., Broquet et al., 2009) covering the same period as the reanalysis. Univariate error covariances are modeled using a diffusion operator (Moore et al., 2011a; Weaver and Courtier, 2001), and the horizontal and vertical decorrelation scales are taken to be 10 km and 20 m, respectively. No balance relations between control variables have been used for explicit multivariate error covariances. Examination of the ROMS-4DVAR output (i.e., the linear and nonlinear cost function values) indicates that the assumption of linear dynamics within the 24 h assimilation window is reasonable (e.g. Neveu et al., 2016, not shown here).

3.3 Observations

In-situ observations of temperature and salinity were collected from three different sources: The Copernicus Marine Environment Monitoring Service (see http://marine.copernicus.eu), the EN4 data set available from the UK Met Office (Good et al., 2013), and from The International Council for the Exploration of the Sea (sse http://ocean.ices.dk). The compiled data set consists of observations from a variety of observational platforms, such as monitoring cruises, FerryBox (Haller et al., 2015) and moorings. The sea surface temperature (SST) data are from individual satellite

	Posterior bias	Prior bias	Posterior RMSE	Prior RMSE
u (native) [ms^{-1}]	-0.006	0.000	0.168	0.225
v (native) [ms^{-1}]	-0.007	0.052	0.195	0.255
temperature [K]	0.006	-0.079	0.552	0.767
salinity	-0.028	-0.057	0.873	0.981

Table 1. Verification statistics: biases and root-mean-square errors (RMSE).

overpasses projected onto a grid with 1.5 km resolution (Eastwood, 2011). The SST data used here are obtained from infrared senors, and thus observations are only available during cloud free conditions.

The SMHI deployed medium-range (13.5 MHz) CODAR SeaSonde HF radars late in 2014 on two sites on the Swedish west coast at Måseskär and Väderöarna (see Fig. 2). The radars were operative throughout 2015, but changes in carrier frequency and bandwidth were made in winter/spring 2015 due to issues with noise. For this reason we only use HF radar data collected from Apr. 1, 2015. The combined data ("total vectors") from the two sites were assimilated as horizontal velocity vectors with an effective depth of 0.7 m (Röhrs et al., 2015).

3.4 Transports, wind forcing and freshwater height

For the analysis of the NCC variability we calculate the transports through the section Torungen-Hirtshals (Fig. 2). The model results show that, on average, neither the NCC or the JC extend across the deepest point of the Norwegian Trench, and the NCC and JC transport estimates are calculated for the sub-sections indicated in Fig. 7. In addition, we do not include the transport below 200 m depth to reduce the influence of the subsurface Atlantic water in the Norwegian Trench. The impact of assimilation on the NCC transport is calculated using adjoint techniques (e.g. Moore et al., 2011c; Neveu et al., 2016), and the analysis increments to the NCC due to the various observation types are shown later on in Sec. 4.2.

We also calculate the time integrated wind stress τ in the direction n normal to the Torungen-Hirtshals section as

$$\tau(t) = \frac{1}{T}\int_{-T+t}^{t} (\overline{\tau}_A \cdot n)\, dt', \tag{1}$$

where the overbar denotes the spatial average of the model wind stress in the region indicated in Fig. 7. In Sec. 4.4, we correlate this average wind stress with the modeled NCC and JC transports, and the time period T is varied in order to identify the response time of the coastal currents to changes in the wind forcing.

Finally, to investigate the transport of freshwater in the surface layer we calculate the freshwater height from the salinity S as

$$\mathrm{FWH} = \int_{\zeta-10}^{\zeta} \frac{\max(0, 35 - S)}{35}\, dz, \tag{2}$$

where ζ is the instantaneous sea surface height. For comparison with other studies utilizing the freshwater height (e.g. Gustafsson, 1999; Gustafsson and Stigebrandt, 1996), please note that we restrict the integration to the upper 10 m of the water column to avoid excessive influence of bathymetry on the results.

4 Results

4.1 Verification

Average prior and posterior model error statistics for the period Oct. 1, 2014 to Nov. 30, 2015 are shown in Table 1. The posterior biases are reduced compared to the prior biases, demonstrating that the analysis scheme successfully draws the model closer to the observations. The only exception is the native u-velocity component, which has a negligible bias from the outset. The HF radar observations are taken at a location where the native u-velocities are more or less normal to the coastline and thus close to zero, hence a small bias for this variable is not surprising. The

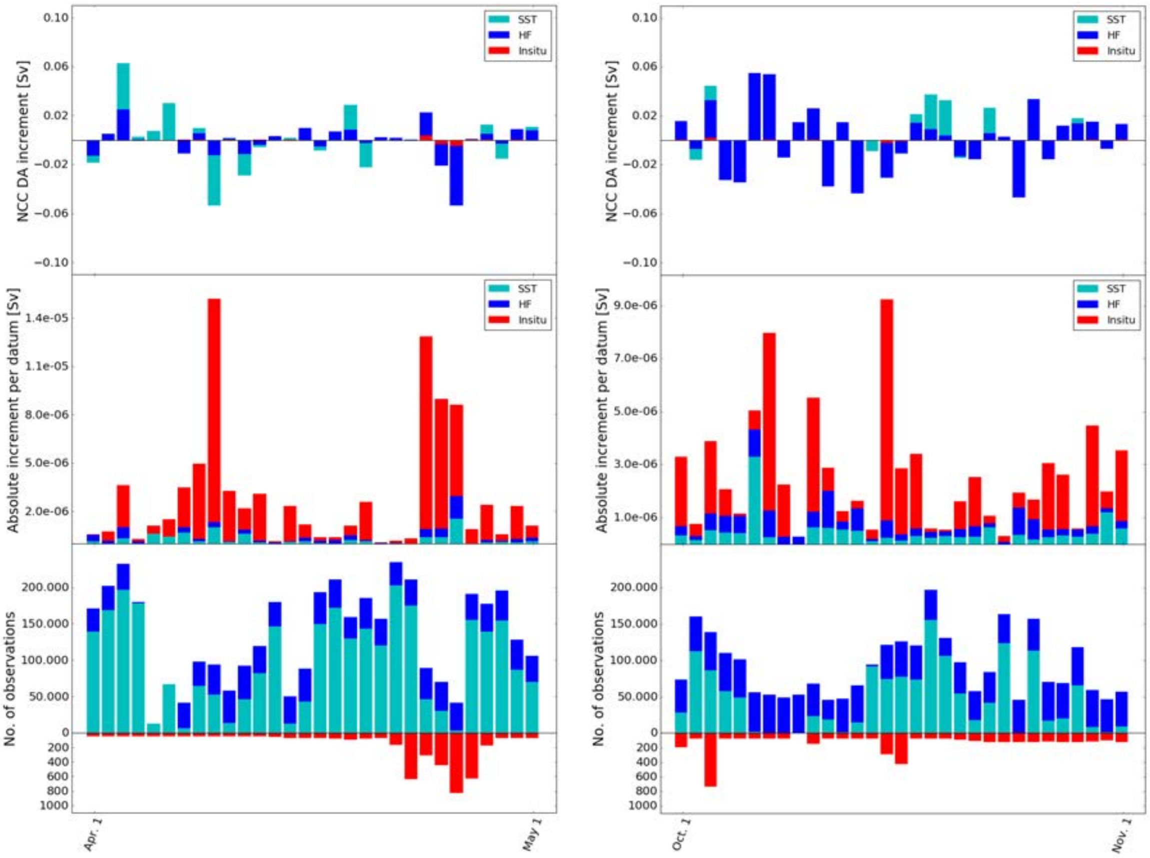

Figure 3. The upper panels show the impact of the observations on the analysis increment in the NCC in Apr. and Oct. 2015, respectively. Each bar represents one assimilation cycle of 24 h. The middle panels shows the average impact per observation (absolute value). The lower panels show the number of observations per assimilation cycle. Note the difference in scale above and below the zero line.

biases are in general small, which is encouraging since the analysis scheme assumes a bias free model, although that is difficult to achieve in practice. The posterior root-mean-square errors (RMSE) are smaller than the prior RMSE for all state variables. We may note here that many of the salinity observations are from a mooring close to the Swedish coast where we would expect the model to be less accurate due to unresolved processes. If these observations are left out, the prior and posterior RMSE values for salinity become 1.031 and 0.655, respectively, which should be more representative for observations collected by research vessels, drifting buoys, FerryBox, and other instrument platforms operating further offshore.

4.2 Observation impacts

Figure 3 shows the observation count and the analysis increments in the NCC transport for all assimilation cycles in Apr. and Oct. 2015, respectively. The bottom panels show that the total number of observations vary greatly from one assimilation cycle to the next. The bulk of the observations are satellite SST but the HF radars provide a substantial amount of data as well. In-situ data are primarily from regular monitoring cruises and FerryBox in addition to the observations received every day from the mooring mentioned above. The top panels of Fig. 3 show the analysis increments in the NCC transport through the part of the Torungen-Hirtshals section shown in Fig. 7. We note that the increments are both positive and negative, indicating that the transport estimates are not significantly

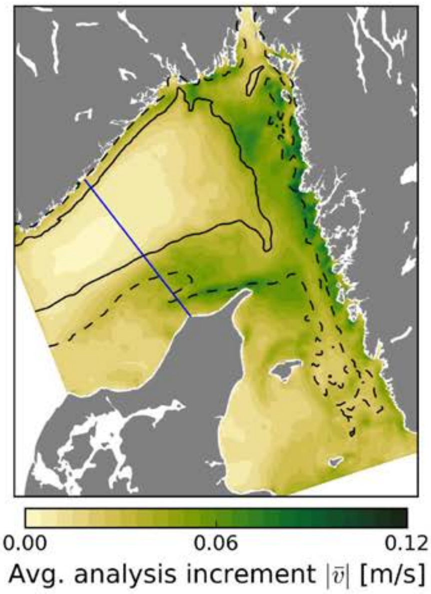

Figure 4. Average analysis increment in the vertically averaged current speeds (Apr. 1 to Oct. 31, 2015). The isolines denote the 200 m isobath (solid) and 50 m isobath (dashed). The straight line across the Skagerrak in this and the following figures shows the Torungen-Hirtshals section.

biased, and that the analysis scheme adjusts the estimates either way depending on the specific conditions and the available observations. The middle panels show the average impact per datum (absolute value), and here we see that although the number of insitu observations is generally small, the value of a single insitu observation is large compared to a single SST or HF radar observation.

The HF radar coverage area is quite some distance from the Torungen-Hirtshals section and hence the currents here are not observed directly. The high impact of the HF radar observations shown in the top panels of Fig. 3 thus point to a significant indirect influence through multivariate adjustments of the upstream conditions. These adjustments will necessarily have to be close enough to the section to influence the transport within the 24 h assimilation window. The distance to the HF radar coverage area is about 70-80 km, which suggests that the main impact is through adjustments of the fast barotropic mode. Another alternative is a baroclinic signal propagating directly from the coverage area across the isobaths to the section (assuming a propagation speed of about 1 ms^{-1}). We have calculated the average analysis increments in the barotropic speed for the period Apr. 1 to Oct. 31, 2015 (Fig. 4). This average shows that the largest increments are found north of Skagen and along the Swedish coast, with smaller increments along the Norwegian coast of 3-5 cms^{-1}, which might explain the high impact of assimilating HF radar data. Dedicated data-denial or observation sensitivity experiments have not yet been made, however, hence the details of this upstream influence and the isolated impact of the various observation platforms are presently unknown.

4.3 Annual averages in velocities, freshwater distribution and sea surface height

Figure 5 shows maps of average surface velocities, vertically averaged velocities, freshwater height, and sea surface height for the period Nov. 1, 2014 to Oct. 31, 2015. Panel (a) shows that the strongest surface velocities are associated with the JC and the NCC, and also with the current flowing northward along the Swedish coast. The circulation in the Kattegat is primarily anticyclonic in agreement with previous studies (e.g. Nielsen, 2005). Interestingly, there is an average flow from the Danish to the Norwegian side of the Skagerrak that crosses the deep Norwegian Trench. The average surface currents in the Skagerrak are often assumed to follow the coastlines, but it has been noted

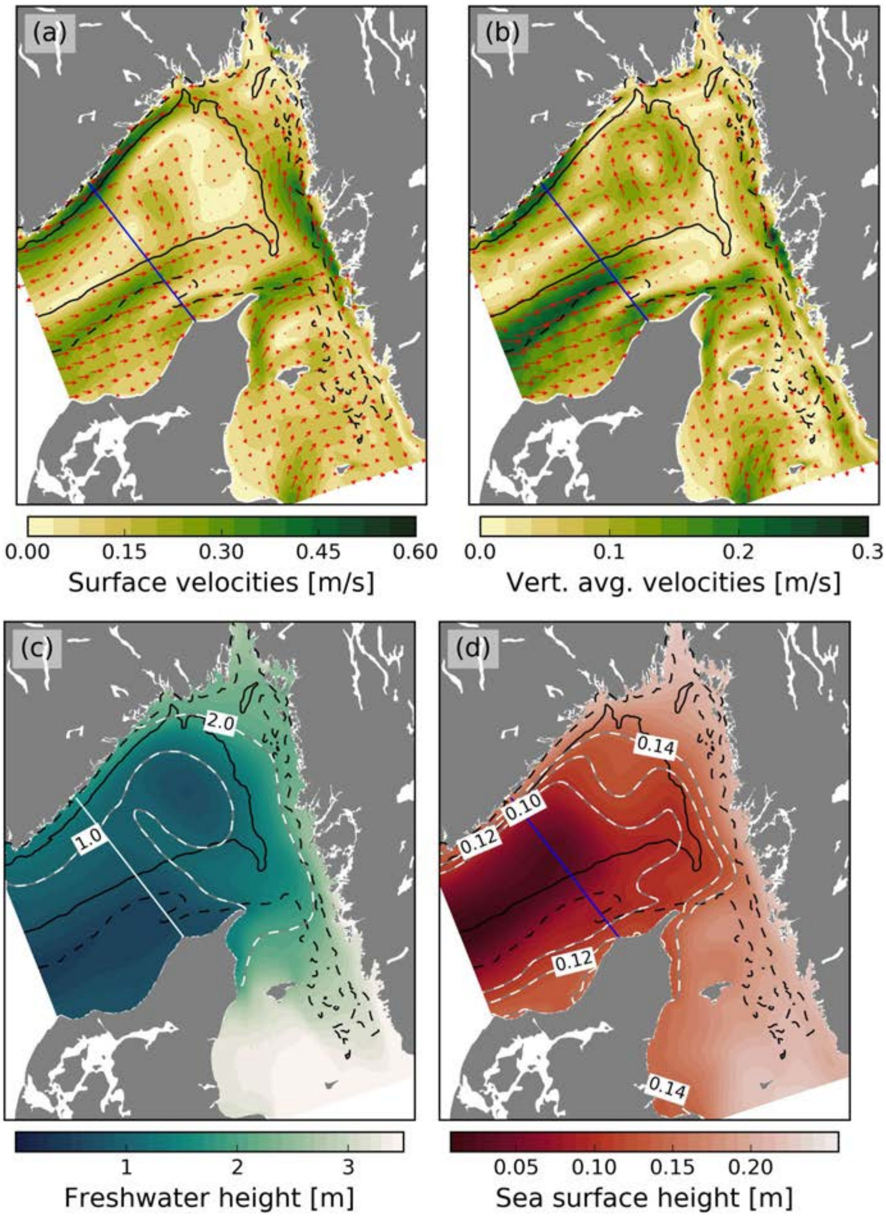

Figure 5. Maps of (a) surface velocities, (b) vertically averaged velocities, (c) freshwater height, and (d) sea surface height averaged over the period Nov. 1, 2014 to Oct. 31, 2015. Additional white-dashed isolines are shown in Panels (c) and (d) for emphasis. The black isolines denote the 200 m isobath (solid) and 50 m isobath (dashed).

that the currents northeast of Skagen are comparatively weak and more variable (Rodhe, 1996). It should also be emphasized that we only consider one specific year here and that our averages are not necessarily representative for longer periods.

In Panel (b) we see that the vertically averaged currents have a similar pattern as the surface currents. There is evidence, however, of a persistent anticyclonic eddy at the northeastern end of the Norwegian Trench. This eddy is

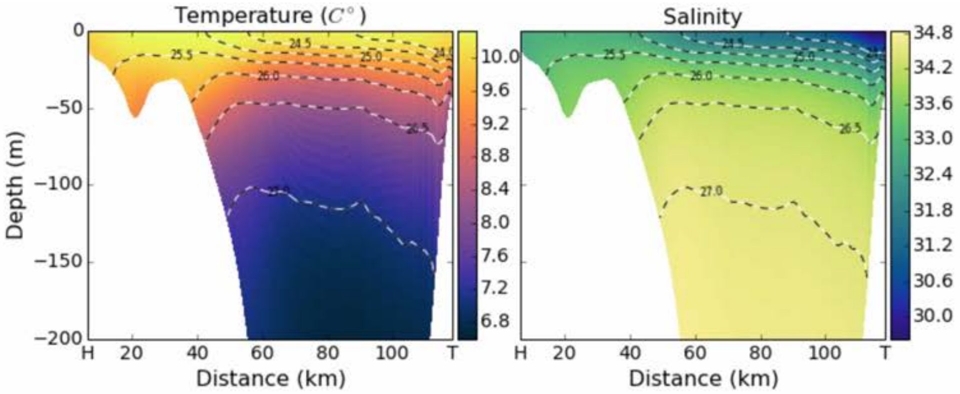

Figure 6. Temperature and salinity in the section between Torungen (T) and Hirtshals (H) averaged over the period Nov. 1, 2014 to Oct. 31, 2015.

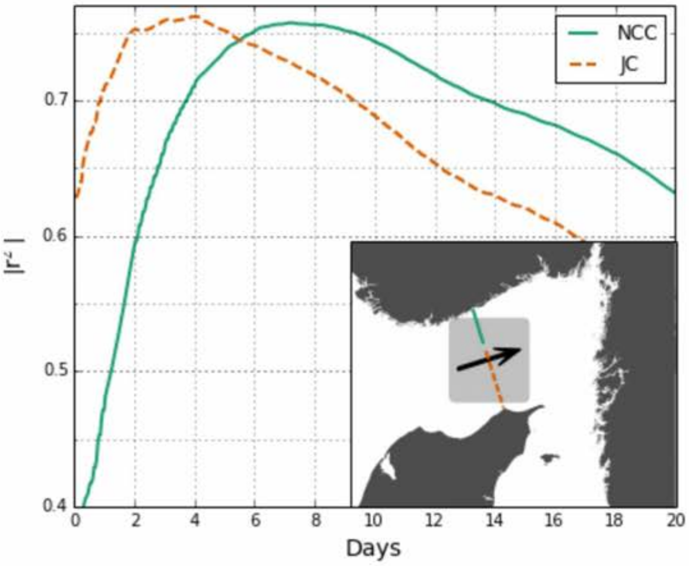

Figure 7. Correlation between the time integrated wind forcing (1) and the JC (dashed) and NCC (solid) transports as a function of integration period T. The inset shows the lateral extents of the Torungen-Hirtshals section used in the calculation of each transport, as well as the area over which the wind forcing is averaged. The arrow points in what we here define as the positive direction.

also visible in the freshwater height (Panel c) as a pool of surface water with higher salinity, and to some extent in the sea surface height (Panel d) as a slight increase in the surface level not following the isobaths. Such an eddy has previously been observed, for example in satellite SAR images showing sea ice trapped in an eddy very much like the one depicted in Panel (b), see Hansen et al. (2010). We will briefly discuss mechanisms for generating and maintaining such anticyclonic circulation in Sec. 4.4.

Otherwise, the distribution of freshwater is as expected, with the freshwater content increasing gradually from the North Sea toward the Baltic Sea, and with more freshwater associated with transport of Baltic Sea water in the NCC compared to the more saline JC coming in from the North Sea. The average sea surface height also increases gradually from the North Sea toward the Baltic Sea, and reflects the dominating cyclonic circulation in

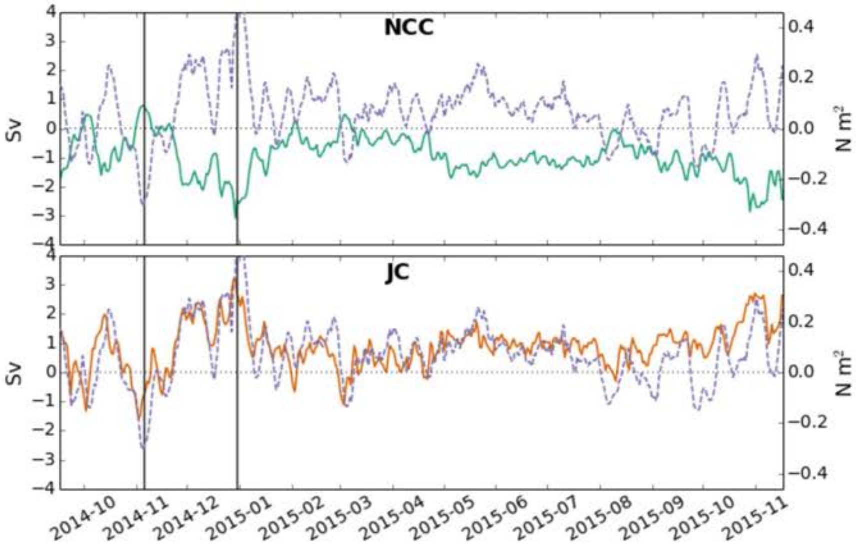

Figure 8. Time series of the JC and NCC transports (solid) and the time integrated wind forcing (1) for an integration period $T = 7$ days (dashed). The two vertical black lines denote a minimum and a maximum in the NCC transport and correspond to the two cases studied in more detail.

the Skagerrak with a minimum in the deepest part. The average temperature and salinity in the upper 200 m of the Torungen-Hirtshals section is shown in Fig. 6. Here we also see that the lighter water masses are found close to either coast and that the salinities are lower toward the Norwegian side. The "doming" of the isotherms in the central Skagerrak noted in previous studies is also well reproduced in the annual average (e.g. Danielssen et al., 1996; Pingree et al., 1982; Røed and Albretsen, 2007).

4.4 Correlations between the wind forcing and the coastal transports

Figure 7 shows the correlations between the time integrated wind stress (1) and the JC and NCC transports through the Torungen-Hirtshals section for a range of integration periods T. The correlations increase sharply from T close to zero until attaining their maxima at $T \approx 4$ days and $T \approx 7$ days for the JC and NCC transports, respectively. As the integration period is further increased the correlations decrease slowly. A response time of 7 days for the NCC is in agreement with Gustafsson (1999), who based his estimate on a baroclinic propagation speed of 1 ms^{-1}. Whatever causes these particular response times, it is nevertheless clear that the time integrated wind forcing explains about 75% of the variance NCC transport, which may be considered as one of the main results of this paper.

Figure 8 shows time series of the time integrated wind stress and the JC and NCC transports using $T = 7$ days. The direction is defined as in Fig. 7, that is, the NCC transport is on average negative while the JC transport is on average positive, and a positive wind stress is produced by winds into the Skagerrak. The time series show that the largest variations are in the cold season and the fluctuations are small from late spring through summer. Gustafsson (1997, see also references therein) describes how winds into the Skagerrak will lead to upwelling along the Norwegian coast, with a reduction in available potential energy and hence a reduction in the NCC. At the same time the Ekman transport across the Skagerrak will lead to an intensification of the JC. This intensification then propagates along the rim of the Skagerrak and after some time the NCC transport should increase again. A shift in the wind direction from southwesterly to northeasterly during this period will further strengthen the NCC transport out of the Skagerrak. Our results show that the intensification of the JC peaks after 4 days of sustained winds into the Skagerrak and that the intensification of the NCC lags the JC with an additional 3 days. The distance between Hirtshals and Torungen, measured along the coast in a counterclockwise direction, is approximately 300 km, which indicates a propagation speed of about 1.2 ms^{-1}.

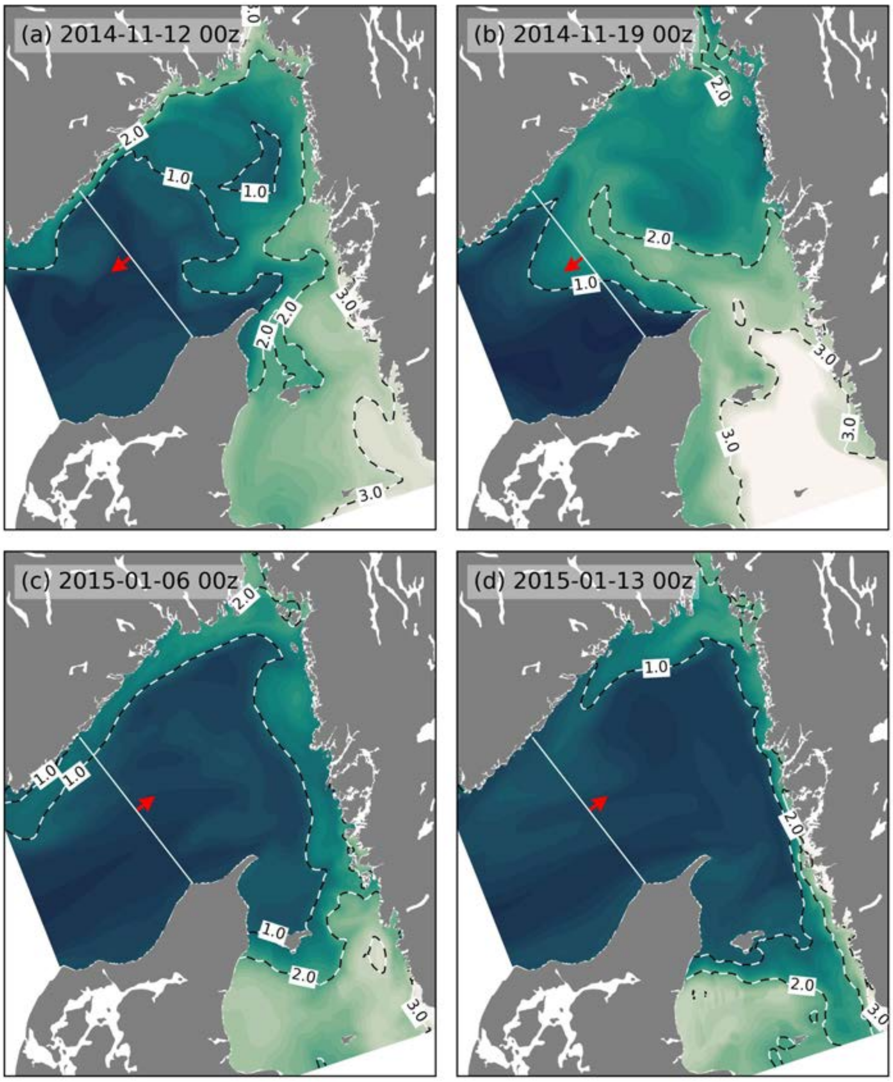

Figure 9. Maps of freshwater height at the time of the NCC minimum (b) and the week before (a), and at the NCC maximum (d) and the week before (c). The red arrows indicate the dominating wind direction for each case.

We now proceed to investigate two cases in more detail. The two vertical black lines in Fig. 8 mark a minimum (in fact a reversal) and a maximum in the NCC. Figure 9 shows maps of the freshwater height at these extremes as well as the situations one week before, consistent with our finding of a response time of 7 days for the NCC to the wind forcing. Figure 10 shows the surface velocities for the two extremes. The case with winds out of the Skagerrak and a minimum in the NCC is shown in Panels (a) and (b) in Fig. 9, and in Panel (a) in Fig. 10. We see that the Kattegat-Skagerrak front initially passes from Skagen toward the Swedish coast, and there is slightly more freshwater in the surface layer north of the front as compared to the annual average (Fig. 5). At the time of the minimum the JC is blocked and the Kattegat-Skagerrak front is deflected away from the Swedish coast and cuts across the Skagerrak toward the Norwegian coast (for a description of a similar case, see Aure et al., 2007). Near the Norwegian coast we see that a tongue of freshwater turns east, interacting with the more saline water masses to

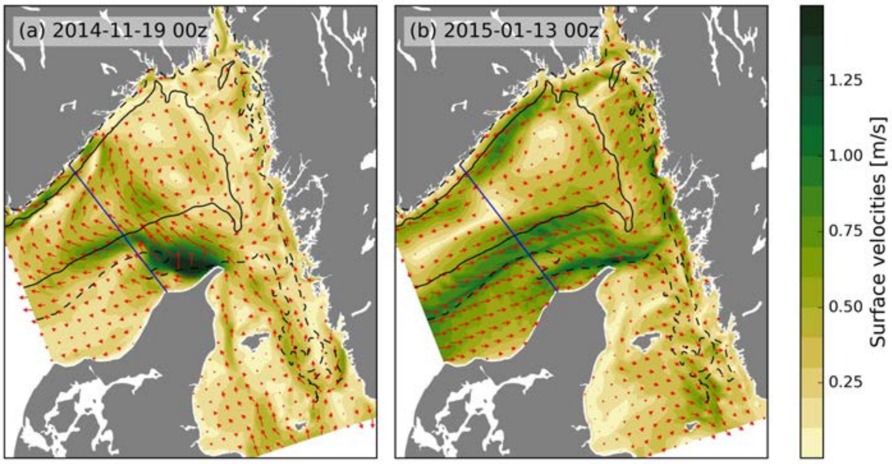

Figure 10. Surface velocities at the time of (a) the NCC minimum and (b) the NCC maximum. The black isolines denote the 200 m isobath (solid) and 50 m isobath (dashed).

the east and forming an anticyclonic eddy such as mentioned in Sec. 4.3 (Fig. 10, Panel a). The case with winds into the Skagerrak and a maximum in the NCC starts altogether differently. In Fig. 9, Panel (c) we see that there is initially much less freshwater in the Skagerrak and that the Kattegat-Skagerrak front is pushed back into the Kattegat. At the peak (Panel d), the front is pushed even further south and saline surface water extends all the way toward the southern boundary on the Swedish side of the Kattegat. A local minimum in the freshwater height appears at the northeastern end of the Norwegian Trench in approximately the same position as the local minimum in the annual average, coinciding with the location of the anticyclonic eddy seen in Fig. 5, Panel (b). The circulation in this case is, however, cyclonic (Fig. 10, Panel b). The density in the late autumn and winter is primarily controlled by salinity, which would explain the differences between the two eddies seen in Fig. 10: the anticyclonic circulation in Panel (a) is consistent with a light core eddy, where the core consists of freshwater brought by the deflected Kattegat-Skagerrak front. The reason why we have a local maximum in the salinity (Fig. 9, Panel b), and hence near surface density, is more elusive, although the cyclonic circulation is consistent with a dense core eddy.

Figure 11 shows the velocities through the Torungen-Hirtshals section at the peaks and one week before. The case with winds out of the Skagerrak and a blocking of the coastal currents (left hand-side panels) is hard to explain in terms of Ekman transport and upwelling, primarily because the Kattegat-Skagerrak front crosses the section twice and a significant part of the flow is along the section. At the point in time when we have a minimum in the coastal currents, the sea surface height has a local maximum in the interior of the Skagerrak associated with the presence of freshwater from the Kattegat. The case with winds into the Skagerrak and intensification of the coastal currents (right hand-side panels) is easier to explain in terms of Ekman transport and upwelling: sharp gradients in the density field on the Norwegian side are reduced due to upwelling (not shown here), and the sea surface slope toward the Danish side increases as the surface water is transported toward Denmark, leading to an intensification of the JC. From the bottom panel on the right we do see that the part of the NCC closest to the coast decrease in strength, but an increase in the interior parts implies an overall strengthening of the total transport on the Norwegian side of the basin. It is also clear that there is a net inflow to the Skagerrak with an overall increase in the surface level.

5 Discussion and concluding remarks

Numerous authors have commented on the large variability in the Kattegat and Skagerrak circulation and several conceptual models for how this circulation depends on local and remote atmospheric forcing has been presented in the literature (e.g. Gustafsson, 1997; Nielsen, 2005; Stigebrandt, 1983). Our approach has been to use a high resolution reanalysis assimilating all available in-situ and remote sensing observations of salinity and temperature.

In addition, we have assimilated surface currents from two coastal HF radars that were ideally placed to observe the exchange between the Kattegat and Skagerrak. We can investigate details of the circulation in our analyzed fields that are missing in data sets from large field campaigns. Such modeling effort is costly in terms of computing resources and we have so far only covered a period of slightly more than one year. Therefore we do not know if our results are representative of the circulation on longer time scales, but note that the model bias and RMSE values are small, and that annual averages reproduce the main features of the circulation as reported in previous studies, such as an anticyclonic surface flow in the Kattegat, an overall cyclonic circulation in the Skagerrak, and realistic stratification across the Torungen-Hirtshals section.

When investigating the relation between the time integrated wind forcing in the Skagerrak and the strength of the coastal currents, we find remarkably high correlations. The Norwegian Coastal Current has a response time to the local wind forcing of about 7 days, in agreement with previous estimates (Gustafsson, 1999). The two cases studied more in detail in Sec. 4.4 suggest an asymmetry in the forcing mechanisms. For winds into the Skagerrak, if the Kattegat-Skagerrak front is either in its normal position between Skagen and the Swedish coast, or located even further south, the direct influence of the Baltic outflow will be small. In such cases the conceptual models presented in earlier studies could be valid. For winds out of the Skagerrak, a strong outflow of Baltic Sea water from the Kattegat can disrupt local processes near the coasts on either side. If the Kattegat-Skagerrak front crosses over toward the Norwegian coast both the JC and the NCC will be blocked, in particular if such situations tend to induce an anticyclonic eddy at the northeastern end of the Norwegian Trench. From our results it appears that this anticyclonic eddy is a common feature meriting further investigation. In addition, there is an assymetry in the barotropic response to wind forcing. The Skagerrak is open to the west and there are no physical barriers blocking a surge from the North Sea. In contrast, winds out of Skagerrak will initially lead to a decrease in the sea surface level here, which will again trigger a more complex response in the Kattegat and in the flows through the narrow straits toward the Baltic further south (e.g. Nielsen, 2005; Stigebrandt, 1983). Despite these asymmetries in the forcing mechanisms, the time series of the transport and the history of the local winds (Fig. 8) indicate that the coastal currents respond just as strongly to winds out of the Skagerrak as into the Skagerrak.

Acknowledgments
We wish to express our thanks to Anders Stigebrandt (Univ. Gothenburg) and Andrew Moore (UCSC) for stimulating discussions, and to Pia Andersson, Johan Kronsell and Magnus Wenzer at the SMHI for generously sharing the HF radar data. Financial support from the Research Council of Norway (grants 244262 ”RETROSPECT” and 237906 ”CIRFA”), and the Swedish Research Council Formas (grant ”Microplastics in marine waters: Sources, pathways, fate and indicator species”) is gratefully acknowledged. High performance computing resources has been provided by NOTUR (NN9197K).

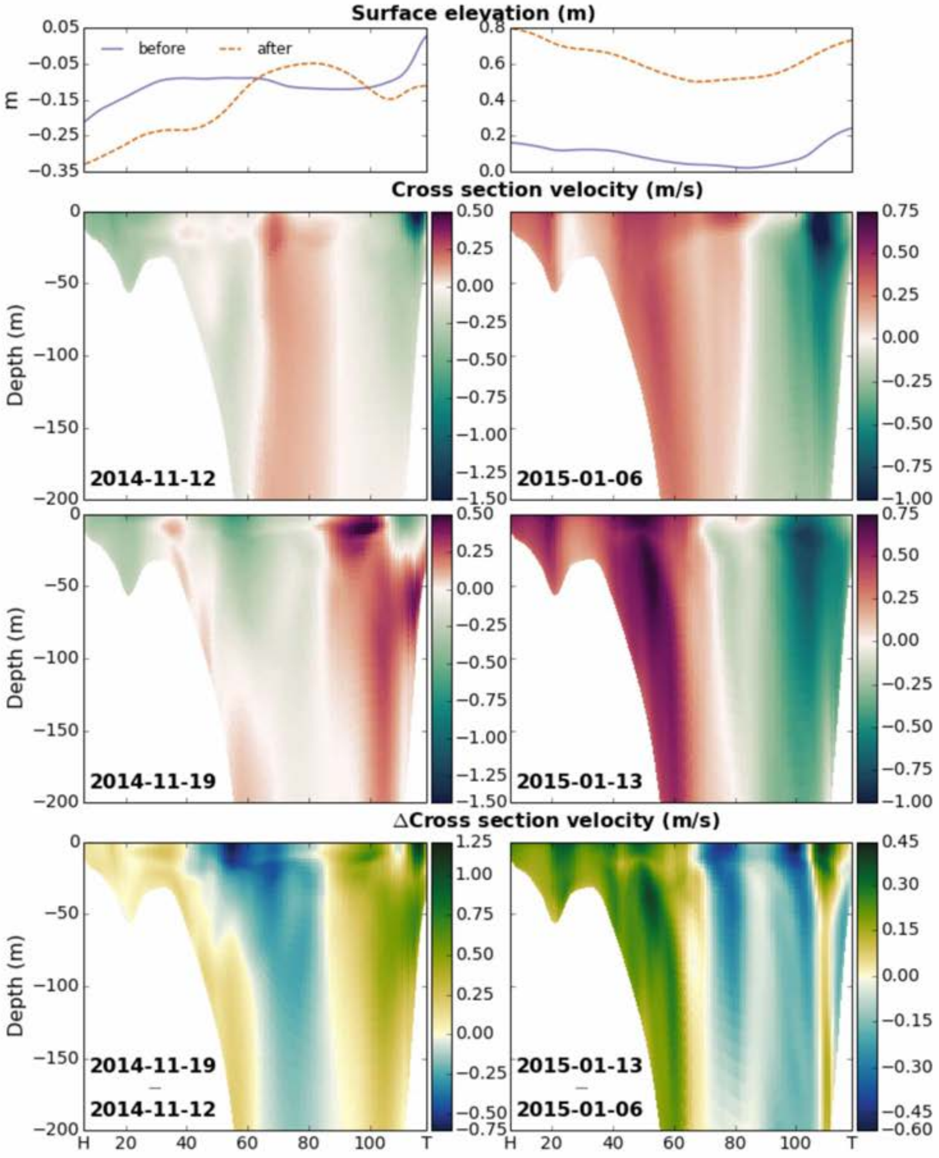

Figure 11. Velocities across the Torungen-Hirtshals section for the case of the NCC minimum (left hand-side) and maximum (right hand-side). The top panels show the surface elevation one week prior (solid) and at the time of the minimum/maximum (dashed). The bottom panels show the differences in velocity that develop in the week leading up to the NCC minimum/maximum.

References

Albretsen, J., J. Aure, R. Saetre, and D. S. Danielssen, 2012: Climatic variability in the Skagerrak and coastal waters of Norway. *ICES J. Mar. Sci.*, **69 (5)**, 758–763, doi:10.1093/icesjms/fsr187.

Aure, J., L. Asplin, R. Sætre, and R. Saetre, 2007: *The Norwegian Coastal Current—Oceanography and Climate*. Tapir Academic Press Trondheim.

Berntsen, J., and E. Svendsen, 1999: Using the SKAGEX dataset for evaluation of ocean model skills. *J. Mar. Syst.*, **18**, 313–331, doi:10.1016/S0924-7963(97)00111-5.

Broquet, G., C. A. Edwards, A. M. Moore, B. S. Powell, M. Veneziani, and J. D. Doyle, 2009: Application of 4d-Variational data assimilation to the California Current System. *Dynam. Atmos. Oceans*, **48 (1-3)**, 69–92, doi:10.1016/j.dynatmoce.2009.03.001.

Broström, G., A. Carrasco, L. R. Hole, S. Dick, F. Janssen, J. Mattsson, and S. Berger, 2011: Usefulness of high resolution coastal models for operational oil spill forecast: the "Full City" accident. *Ocean Sci.*, **7 (6)**, 805–820, doi:10.5194/os-7-805-2011.

Craig, P. D., and M. L. Banner, 1994: Modeling wave-enhanced turbulence in the ocean surface layer. *J. Phys. Oceanogr.*, **24 (12)**, 2546–2559, doi:10.1175/1520-0485(1994)024⟨2546:MWETIT⟩2.0.CO;2.

Danielssen, D. S., L. Edler, S. Fonselius, L. Hernroth, M. Ostrowski, E. Svendsen, and L. Talpsepp, 1997: Oceanographic variability in the Skagerrak and northern Kattegat, May-June, 1990. *ICES J. Mar. Sci.*, **54 (5)**, 753–773, doi:10.1006/jmsc.1996.0210.

Danielssen, D. S., E. Svendsen, and M. Ostrowski, 1996: Long-term hydrographic variation in the Skagerrak based on the section Torungen–Hirtshals. *ICES J Mar Sci*, **53 (6)**, 917–925, doi:10.1006/jmsc.1996.0113.

Dooley, H. D., 1974: Hypotheses concerning the circulation of the northern North Sea. *ICES J. Mar. Sci.*, **36 (1)**, 54–61, doi:10.1093/icesjms/36.1.54.

Eastwood, S., 2011: Atlantic high latitude l3 sea surface temperature product user manual.

Egbert, G. D., and S. Y. Erofeeva, 2002: Efficient inverse modeling of barotropic ocean tides. *J. Atmos. Oceanic Tech.*, **19 (2)**, 183–204, doi:10.1175/1520-0426(2002)019⟨0183:EIMOBO⟩2.0.CO;2.

Fairall, C. W., E. F. Bradley, J. E. Hare, A. A. Grachev, and J. B. Edson, 2003: Bulk parameterization of air-sea fluxes: Updates and verification for the COARE algorithm. *J. Climate*, **16 (4)**, 571–591, doi:10.1175/1520-0442(2003)016⟨0571:BPOASF⟩2.0.CO;2.

Golbeck, I., and Coauthors, 2015: Uncertainty estimation for operational ocean forecast products——a multi-model ensemble for the North Sea and the Baltic Sea. *Ocean Dyn.*, **65 (12)**, 1603–1631, doi:10.1007/s10236-015-0897-8.

Good, S. A., M. J. Martin, and N. A. Rayner, 2013: EN4: Quality controlled ocean temperature and salinity profiles and monthly objective analyses with uncertainty estimates. *J. Geophys. Res. C: Oceans*, **118 (12)**, 6704–6716, doi:10.1002/2013JC009067.

Gratton, S., and J. Tshimanga, 2009: An observation-space formulation of variational assimilation using a restricted preconditioned conjugate gradient algorithm. *Q. J. Roy. Meteorol. Soc.*, **135 (643)**, 1573–1585, doi:10.1002/qj.477.

Gustafsson, B., 1997: Interaction between Baltic Sea and North Sea. *Dtsch. Hydrogr. Z.*, **49 (2-3)**, 165–183, doi:10.1007/BF02764031.

Gustafsson, B., 1999: High frequency variability of the surface layers in the Skagerrak during SKAGEX. *Cont. Shelf Res.*, **19 (8)**, 1021–1047, doi:10.1016/S0278-4343(99)00008-4.

Gustafsson, B., and A. Stigebrandt, 1996: Dynamics of the freshwater-influenced surface layers in the Skagerrak. *J. Sea Res.*, **35**, 39–53, doi:10.1016/S1385-1101(96)90733-9.

Haller, M., F. Janssen, J. Siddorn, W. Petersen, and S. Dick, 2015: Evaluation of numerical models by FerryBox and fixed platform in situ data in the southern North Sea. *Ocean Sci.*, **11 (6)**, 879–896, doi:10.5194/os-11-879-2015.

Hansen, M., K. Kloster, K.-F. Dagestad, S. Sandven, and J. Johannessen, 2010: Retrieval of Sea Ice Drift from SAR Doppler Shift. *Proceedings of ESA Living Planet Symposium*, ESA, Bergen, Norway.

Jakobsen, F., 1997: Hydrographic investigation of the Northern Kattegat front. *Cont. Shelf Res.*, **17 (5)**, 533–554, doi:10.1016/S0278-4343(96)00044-1.

Marchesiello, P., J. C. McWilliams, and A. Shchepetkin, 2001: Open boundary conditions for long-term integration of regional oceanic models. *Ocean model.*, **3 (1)**, 1–20, doi:10.1016/S1463-5003(00)00013-5.

McClimans, T., J. Pietrzak, V. Huess, N. Kliem, J. Nilsen, and B. Johannessen, 2000: Laboratory and numerical simulation of the Skagerrak circulation. *Cont. Shelf Res.*, **20**, 941–974, doi:10.1016/S0278-4343(00)00007-8.

Moore, A. M., H. G. Arango, G. Broquet, B. S. Powell, A. T. Weaver, and J. Zavala-Garay, 2011a: The Regional Ocean Modeling System (ROMS) 4-dimensional variational data assimilation systems. *Progr. Oceanogr.*, **91 (1)**, 34–49, doi:10.1016/j.pocean.2011.05.004.

Moore, A. M., and Coauthors, 2011b: The Regional Ocean Modeling System (ROMS) 4-dimensional variational data assimilation systems. *Progr. Oceanogr.*, **91 (1)**, 74–94, doi:10.1016/j.pocean.2011.05.005.

Moore, A. M., and Coauthors, 2011c: The Regional Ocean Modeling System (ROMS) 4-dimensional variational data assimilation systems. *Progr. Oceanogr.*, **91 (1)**, 50–73, doi:10.1016/j.pocean.2011.05.003.

Neveu, E., A. M. Moore, C. A. Edwards, J. Fiechter, P. Drake, W. J. Crawford, M. G. Jacox, and E. Nuss, 2016: An historical analysis of the California Current circulation using ROMS 4d-Var: System configuration and diagnostics. *Ocean Model.*, **99**, 133–151, doi:10.1016/j.ocemod.2015.11.012.

Nielsen, M. H., 2005: The baroclinic surface currents in the Kattegat. *J. Mar. Syst.*, **55 (3-4)**, 97–121, doi:10.1016/j.jmarsys.2004.08.004.

Pingree, R. D., P. M. Holligan, G. T. Mardell, and R. P. Harris, 1982: Vertical distribution of plankton in the skagerrak in relation to doming of the seasonal thermocline. *Continental Shelf Research*, **1 (2)**, 209–219, doi:10.1016/0278-4343(82)90005-X.

Rodhe, J., 1996: On the dynamics of the large-scale circulation of the skagerrak. *J. Sea Res.*, **35 (1)**, 9–21, doi:10.1016/S1385-1101(96)90731-5.

Røed, L. P., and J. Albretsen, 2007: The impact of freshwater discharges on the ocean circulation in the Skagerrak/northern North Sea area Part I: model validation. *Ocean Dyn.*, **57 (4-5)**, 269–285, doi:10.1007/s10236-007-0122-5.

Röhrs, J., A. K. Sperrevik, K. H. Christensen, G. Broström, and Ø. Breivik, 2015: Comparison of HF radar measurements with Eulerian and Lagrangian surface currents. *Ocean Dyn.*, **65 (5)**, 679–690, doi:10.1007/s10236-015-0828-8.

Shchepetkin, A. F., and J. C. McWilliams, 2005: The regional oceanic modeling system (ROMS): a split-explicit, free-surface, topography-following-coordinate oceanic model. *Ocean Model.*, **9 (4)**, 347–404, doi:10.1016/j.ocemod.2004.08.002.

Shchepetkin, A. F., and J. C. McWilliams, 2009: Computational Kernel Algorithms for Fine-Scale, Multiprocess, Longtime Oceanic Simulations. *Handbook of Numerical Analysis*, Vol. 14, Elsevier, 121–183.

Stigebrandt, A., 1983: A model for the exchange of water and salt between the Baltic and the Skagerrak. *J. Phys. Oceanogr.*, **13**, 411–427, doi:10.1175/1520-0485(1983)013⟨0411:AMFTEO⟩2.0.CO;2.

Stigebrandt, A., 1987: Computations of the flow of dense water into the Baltic Sea from hydrographical measurements in the Arkona Basin. *Tellus A*, **39A (2)**, 170–177, doi:10.1111/j.1600-0870.1987.tb00298.x.

Umlauf, L., H. Burchard, and K. Hutter, 2003: Extending the k-ω turbulence model towards oceanic applications. *Ocean Model.*, **5 (3)**, 195–218, doi:10.1016/S1463-5003(02)00039-2.

Warner, J. C., C. R. Sherwood, H. G. Arango, and R. P. Signell, 2005: Performance of four turbulence closure models implemented using a generic length scale method. *Ocean Model.*, **8 (1-2)**, 81–113, doi:10.1016/j.ocemod.2003.12.003.

Weaver, A., and P. Courtier, 2001: Correlation modelling on the sphere using a generalized diffusion equation. *Q. J. Roy. Meteorol. Soc.*, **127 (575)**, 1815–1846, doi:10.1002/qj.49712757518.